

The utilization of multiples in imaging and characterization is an emerging methodology. Multiples are waves that are reflected or scattered more than once at the subsurface interfaces and eventually recorded at the seismic detectors. Very often, multiples can reach into the earth to illuminate the shadow zones which primaries cannot reach.



This PhD thesis is about designing and analyzing 3D seismic acquisition geometries in particular for the case that multiple reflections are considered as signal rather than noise.

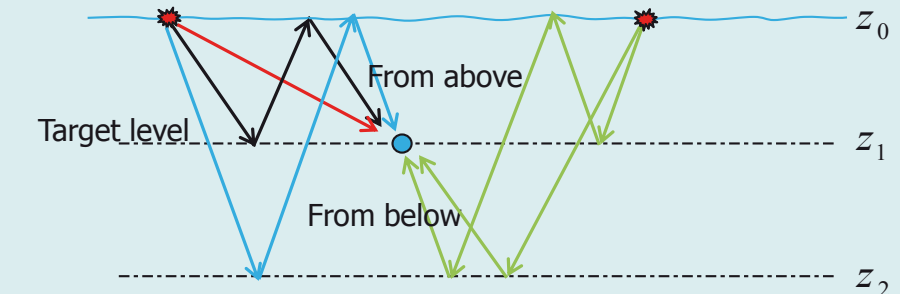
ISBN: 978-94-6203-962-9

3-D SEISMIC ACQUISITION GEOMETRY DESIGN AND ANALYSIS

A. KUMAR

3-D SEISMIC ACQUISITION GEOMETRY DESIGN AND ANALYSIS

INVESTIGATION OF THE REQUIREMENTS TO INCLUDE
ILLUMINATION FROM ALL MULTIPLES



Amarjeet Kumar

3-D seismic acquisition geometry design and analysis

Investigation of the requirements to include
illumination from all multiples

3-D seismic acquisition geometry design and analysis

Investigation of the requirements to include
illumination from all multiples

PROEFSCHRIFT

ter verkrijging van de graad van doctor
aan de Technische Universiteit Delft,
op gezag van de Rector Magnificus prof.ir. K.C.A.M. Luyben,
voorzitter van het College voor Promoties,
in het openbaar te verdedigen op Woensdag 09 December 2015 om 12:30 uur

door Amarjeet KUMAR

Master and Bachelor of Science in Exploration Geophysics,
Indian Institute of Technology Kharagpur, India
geboren te Baidrabad, Bihar.

Dit proefschrift is goedgekeurd door de promotor:
Prof.dr.ir. C.P.A. Wapenaar

Copromotor:
Dr.ir. G. Blacquière

Samenstelling promotiecommissie:

Rector Magnificus,	Technische Universiteit Delft, voorzitter
Prof.dr.ir. C.P.A. Wapenaar,	Technische Universiteit Delft, promotor
Dr.ir. G. Blacquière,	Technische Universiteit Delft, copromotor

Onafhankelijke leden:

Prof.dr.ir. E.C. Slob,	Technische Universiteit Delft
Prof.dr. D.G. Simons,	Technische Universiteit Delft
Prof. K.A. Berteussen,	The Petroleum Institute, Abu Dhabi
Dr. M.W. Pedersen,	Petroleum Geo-Services, Oslo
Dr.ir. A.W.F. Volker,	TNO Delft

The research for this thesis was financially supported partly by Shell/NAM and partly by DELPHI consortium.

ISBN 978-94-6203-962-9

Copyright © 2015 by A. Kumar.

All rights reserved. No part of this publication may be reproduced, stored in a retrieval system or transmitted in any form or by any means, electronic, mechanical, photocopying, recording or otherwise, without the prior written permission of the author.

Printed by: CPI Wöhrmann Print Service, Postbus 92-7200 AB Zutphen
An electronic version of this dissertation is available at
<http://repository.tudelft.nl/>

(Dedicated to my loving parents)

In life if you want to become something, achieve something, win something then always listen to your heart and if your heart doesn't reply to you then close your eyes and take the name of your mom and dad, then see you will achieve everything, everything that is hard will become easy, victory will be yours, just yours.

(Inspired from a Bollywood movie: Kabhi Khushi Kabhi Gham)

Contents

Summary	xi
Samenvatting	xv
1 Introduction	1
1.1 The seismic experiment	1
1.2 Acquisition analysis methods	3
1.2.1 Designing at the surface	3
1.2.2 Designing including the subsurface model	3
1.2.3 Focal beam method	5
1.3 The era of using multiples as signal in imaging	5
1.4 Objective and outline of this thesis	8
1.4.1 Objective	8
1.4.2 Outline	8
2 Theory of model-based acquisition design	11
2.1 Introduction	11
2.2 Operator notation	12
2.3 Representation of seismic data	13
2.4 Grid-point response	17
2.5 Imaging	19
2.6 Focal functions	21
2.6.1 Resolution function	21
2.6.2 AVP function	23
2.7 The ideal focal beams and ideal focal functions	25
2.8 Introduction to the Schoonebeek oil field	27
2.9 Focal beam analysis results and discussion	28
2.9.1 Schoonebeek Geometry and subsurface model	29
2.9.2 Source and detector beam	30
2.9.3 Frequency dependency	31

2.9.4	Focal functions	33
2.9.5	Suggestions for further improvement	35
2.10	Conclusion from this chapter	37
3	Including secondary illumination in seismic acquisition design	39
3.1	Introduction	39
3.2	Double illumination	40
3.3	Including the surface-related multiples in focal beam formulation	42
3.4	Examples	44
3.5	Conclusion from this chapter	50
4	Extending illumination using all multiples: theory	51
4.1	Introduction	51
4.2	Extension of the focal beam method	52
4.2.1	Grid-point response: including multiples	53
4.2.2	Modelling	55
4.2.3	Full wavefield focal beams	60
4.2.4	Illustration of the full wavefield focal beam concept	63
4.3	Full wavefield focusing operator	67
4.4	Conclusion from this chapter	73
5	Extending illumination using all multiples: examples	75
5.1	Introduction	75
5.2	Two-dimensional example	76
5.2.1	Analysis of different geometries	80
5.2.2	Space variance of the beam quality	80
5.3	Three-dimensional examples	83
5.3.1	3-D Model example with a ellipsoidal structure	83
5.3.2	Impact on angle-dependent reflectivity	85
5.3.3	Ziggy model example	87
5.3.4	3-D Model example with a thrust structure	93
5.4	Conclusion from this chapter	99
6	Marine survey design and analysis	103
6.1	Introduction	103
6.2	Theory	105
6.2.1	Focal beams for non-stationary geometries	105
6.2.2	Weighted focal beam concept	106
6.2.3	Extension to multiples	108
6.3	Examples	109
6.3.1	Single source shooting	109

6.3.2	Flip-flop shooting	113
6.4	Application to infill analysis	115
6.5	Discussion	120
6.6	Conclusion from this chapter	121
7	Conclusions and recommendations	123
7.1	Conclusions	123
7.2	Recommendations	126
A	The phase shift operator (W)	127
B	Expression for G in terms of W, R and T	131
C	The Radon transformation	135
	Bibliography	137
	Acknowledgments	147
	Curriculum Vitae	151

Summary

A seismic survey should be designed such that imaging of the acquired data leads to a sufficiently accurate subsurface image. For that purpose, methods for acquisition geometry analysis and design are available. These methods are used to judge whether an acquisition geometry is suited for the specified objectives. Conventional 2D and 3D acquisition geometry analysis methods are largely based on common-midpoint processing that assumes a horizontally layered earth model. Consequently, the influence of the inhomogeneity of the subsurface on the data quality and image quality is not taken into account. However, in practice it has been shown that the data and image quality can suffer significantly from complex geology. Therefore, the inhomogeneity of the subsurface must be taken into account in the acquisition analysis methods. This can be done by the use of a macro model of the subsurface.

Additionally, recent developments in seismic imaging and reservoir characterization use the multiple-reflections in the data to extend the illumination in areas that cannot be reached by the primary-reflections. The use of multiples yields a better vertical resolution as well as to suppress migration artefacts caused by crosstalk of multiple-reflections. The seismic value chain suggests that the new developments in seismic imaging and reservoir characterization should lead to new opportunities in the seismic acquisition. Therefore, the goal of this research is the development of a method that meets all the above mentioned requirements.

The method presented in this thesis is based on the previously developed *focal beam analysis* concept. This concept emphasizes the separate analysis of the source geometry and the detector geometry, leading to two outputs: the focal source beam and the focal detector beam. This gives the opportunity to separately judge and adjust the configuration of the sources and the configuration of the detectors. These beams are inspected in the space-frequency domain and in the Radon-frequency domain. In the spatial do-

main, it is visible whether the wavefield has properly been focused into a point. In the Radon domain, it is visible how the angle-dependent amplitudes are affected by the acquisition geometry and overburden structures. This approach provides thorough understanding of the cause of image deficiencies. The source and detector beams can be multiplied to compute a migrated image. The multiplication can be carried out in two domains to assess the different quality parameters of a seismic image:

- Multiplication of the source and detector beam in the space-frequency domain yields the resolution function, which represents the image of a unit point diffractor.
- Multiplication in the Radon-frequency domain yields the AVP-function, which is the angle-dependent image of one reflection point on an angle-independent reflector.

However, so far this method assumed primary reflections only as signal, leaving out multiple reflections as noise. In this thesis, I discussed that multiples can be considered as signal in the seismic imaging if they are handled correctly. Therefore, I extended this focal beam method to the multiples as well.

In the extended focal beam method, the full wavefield propagation between a subsurface point and the acquisition surface is simulated using a recursive full wavefield modeling engine. It uses a macro velocity model for the wavefield extrapolation from one depth level to another depth level and a reflectivity model to include all the reflection and transmission properties related to the same depth level. Subsequently, the data are focused to the target point using the source and the detector geometry. This full wavefield data is a complex wavefield which includes the effects of all multiples (i.e., propagation as well as reflection and transmission effects). Therefore, the focusing is achieved by a minimization scheme. I have demonstrated with the help of some examples, that the gap in the Radon transformed focal source beam due to sparse sampling issues can be filled with the use of all multiples. It means more angle-dependent information can be obtained.

Imaging of subsalt sediments is challenging in practice, because of the high velocity contrasts and irregular shapes. My analysis shows that in such situation, image quality varies strongly with the position of the target point with respect to salt. In that case, even if one has a perfect source distribution, primary illumination may be limited due to geology. The image quality cannot be improved any further by adjusting the acquisition geometry in this

case. I show that utilizing all multiples may be the part of the solution. The illumination from below is important in such cases. The method presented in this thesis offers opportunities for the investigation of the added value of the surface-related and the internal multiples. To summarize, this new method meets all the following criteria:

- Dealing with the complexity of the subsurface model.
- Considering all the multiple reflections as useful information.
- Illumination from below in the complex sub-salt scenarios.
- Development of geophysical-based infill specifications to assess the impact of coverage holes on data quality.

Amarjeet Kumar

Samenvatting

Een seismische survey dient zo ontworpen te worden dat het verwerken van de verkregen data leidt tot een accuraat beeld van de ondergrond. Om die reden zijn er methodes beschikbaar voor het analyseren en ontwerpen van de seismische acquisitiegeometrie. Deze methodes worden toegepast om te bepalen of een acquisitiegeometrie geschikt is voor de gestelde doelen. De conventionele analyse van 2D en 3D acquisitiegeometrieën is voornamelijk gebaseerd op 'common-midpoint' dataverwerking. Hierbij wordt echter de invloed van de heterogeniteit van de ondergrond op de data en vervolgens de beeldkwaliteit niet in beschouwing genomen. Dit terwijl in de praktijk is aangetoond dat zowel de data als de beeldkwaliteit sterk afhangen van de complexiteit van de geologie. Daarom is het belangrijk dat de heterogeniteit van de ondergrond in rekening wordt gebracht in acquisitieanalysemethodes. Dit kan gerealiseerd worden door een macro-model van de ondergrond te gebruiken.

Recente ontwikkelingen in de seismische beeldvorming en reservoirkarakterisering maken gebruik van meervoudige reflecties in de data om de belichting te verbeteren van zones die niet worden bereikt door primaire reflecties. Het gebruik van meervoudige reflecties resulteert in een verbeterde verticale resolutie en onderdrukt ook migratieartefacten die het gevolg zijn van meerdere reflecties die samenvallen. De seismische waardeketen suggereert dat nieuwe ontwikkelingen in seismische beeldvorming en reservoir karakterisering op hun beurt zullen leiden tot nieuwe ontwikkelingen in de seismische acquisitie. Het doel van dit onderzoek is daarom om een methode te ontwikkelen die aan alle bovengenoemde eisen voldoet.

De methode beschreven in dit proefschrift is gebaseerd op het eerder ontwikkelde concept van 'focal beam' analyse. Dit concept benadrukt de afzonderlijke analyse van de brongeometrie en van de detectorgeometrie. Dit leidt tot twee outputs: de 'focal beam' van de bron en de 'focal beam' van de de-

tector. Dit maakt het mogelijk om de configuratie van de bronnen en de configuratie van de ontvangers afzonderlijk van elkaar te beoordelen en zondig aan te passen. De beams kunnen worden beschouwd in het patiële-frequentiedomein en in het Radon-frequentiedomein. In het patiële domein is te zien of het golfveld correct is gefocusseerd. In het Radon domein is te zien hoe de hoekafhankelijke amplitudes benvloed worden door de acquisitiegeometrie en de structuur van de bovenste lagen. Deze benadering vraagt een grondig begrip van de onderliggende oorzaak van de afwijkingen in het seismische beeld. De 'beams' van de bron en de detector kunnen met elkaar worden vermenigvuldigd om zo een gemigreerde afbeelding te verkrijgen. De vermenigvuldiging kan in twee domeinen worden uitgevoerd om de verschillende kwaliteitsparameters van een seismisch beeld te beoordelen:

- Vermenigvuldiging van de 'beam' van de bron en de detector in het spatiële-frequentie domein resulteert in de resolutiefunctie, die het beeld van een enkele punt diffractor weergeeft.
- Vermenigvuldiging in het Radon-frequentie domein resulteert in de AVP-functie, welke het hoekafhankelijke beeld van een reflectiepunt op een hoekonafhankelijke reflector weergeeft.

Deze methode heeft tot nu toe alleen primaire reflecties beschouwd als signaal, waarbij de meervoudige reflecties verwijderd werden als ruis. In dit proefschrift classificeer ik meervoudige reflecties echter als signaal voor de seismische beeldvorming, onder de voorwaarde dat deze correct worden verwerkt. Ik heb daarom de 'focal beam' methode uitgebreid naar meervoudige reflecties.

In de uitgebreide 'focal beam' methode wordt de propagatie van het volledige golfveld tussen een ondergronds punt en het acquisitieoppervlak gesimuleerd met een iteratief modelleringsprogramma. Dit programma maakt gebruik van een macro-snelheidemodel, en extrapoleert het golfveld van het ene diepteniveau naar het andere. Het maakt ook gebruik van een reflectiecoëfficientmodel, dat de reflectie- en transmissiecoëfficiënten op elk corresponderend diepteniveau berekent. Het gemodelleerde resultaat is een complex golfveld, inclusief de effecten van meervoudige reflecties (dat wil zeggen propagatie, reflectie en transmissieeffecten). In de volgende stap wordt de gemodelleerde data gefocusseerd op het beeldpunt met behulp van de bron- en detectorgeometrie. Het focussen van de data wordt uitgevoerd middels een minimalisatieprocedure. Aan de hand van enkele voorbeelden toon ik aan dat het hiaat in de Radon-getransformeerde 'focal beam' van de bron, veroorzaakt door onvolledige bemonstering, opgevuld kan worden door de meervoudige reflecties

in beschouwing te nemen. Hierdoor komt meer informatie over de hoekaf-hankelijke reflectie beschikbaar.

In de praktijk vormt de beeldvorming van sedimenten onder zoutstructuren een uitdaging vanwege de grote contrasten in snelheid en de onregelmatige vorm van deze structuren. Uit mijn analyse blijkt dat in een dergelijke situatie de beeldkwaliteit sterk varieert met de positie van het beeldpunt ten opzichte van de zoutstructuur. In dit geval is de primaire belichting van het beeldpunt vaak beperkt, zelfs als een perfecte distributie van bronnen is toegepast. De beeldkwaliteit kan dan niet verder worden verbeterd door de acquisitiegeometrie aan te passen. Ik laat zien dat het gebruik van alle meervoudige reflecties een deel van de oplossing kan bieden. De belichting van onderaf is van belang in dergelijke gevallen. De methode die ik in dit proefschrift beschrijf maakt het mogelijk de toegevoegde waarde te onderzoeken van de oppervlaktegerelateerde en de interne, meervoudige reflecties. Samengevat deze nieuwe methode voldoet aan de volgende criteria:

- De complexiteit van de ondergrond moet meegenomen worden.
- Alle meervoudige reflecties moeten als nuttige informatie beschouwd worden.
- Belichting van onderaf in het complexe sub-zout scenario moet mogelijk worden.
- Ontwikkeling van geofysisch gegrondde interpolatiespecificaties om de invloed van gaten in de bedekking op de datakwaliteit te beoordelen.

Amarjeet Kumar

Chapter 1

Introduction

1.1 The seismic experiment

An image of the Earth's subsurface can be acquired by carrying out a seismic survey. In seismic exploration elastic and/or acoustic waves are generated by a source at the surface. For acquisition on land the usual source is dynamite or a seismic vibrator. For a marine survey airguns are most commonly used. The waves are sent into the subsurface, and subsequently the energy is recorded that arrives back at the surface. Here, it is detected with a number of detectors which are either geophones in case of land acquisition or hydrophones in case of marine acquisition. The recorded energy is due to reflection, diffraction and refraction at subsurface boundaries. These boundaries are interfaces between layers of earth that have different elastic properties. In order to get a good quality image this seismic experiment is repeated many times with the shot and the detectors located at different surface positions, such that an inhomogeneity is 'illuminated' and 'detected' from different directions. The result of each seismic experiment is a shot record. It consists of the registration of the reflected wave fields at each detector. The reflected signal is registered as a function of travel time and it contains both propagation (down- and upward) and reflection effects of the subsurface. Such an experiment with one shot-record is illustrated in Figure 1.1.

However, the aim is a structural image of the subsurface from which the propagation effects have been removed. This means that the reflection amplitudes should be presented as a function of lateral position and depth. The method that removes the propagation effects and transforms a time regis-

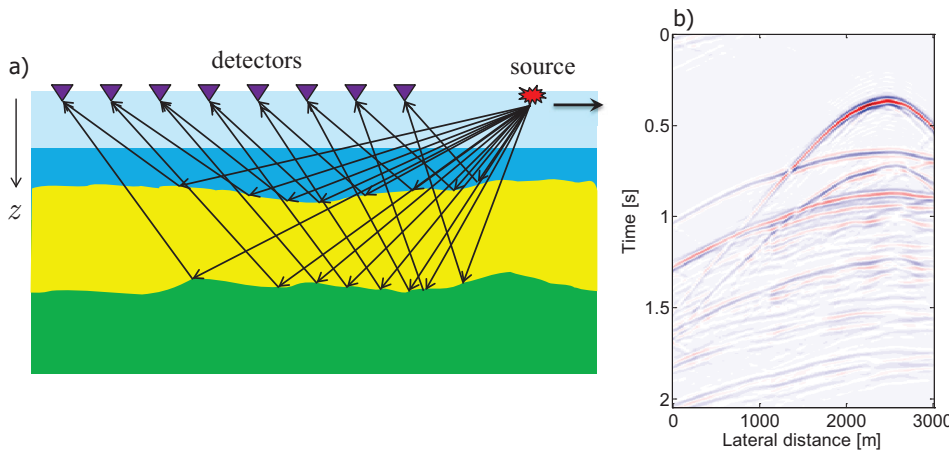


Figure 1.1: a) A seismic experiment. Seismic waves are produced by a source and the reflections are registered by the detectors as a function of time, b) the result of a seismic experiment is a shot record. In a seismic survey many such shot records are acquired.

tration (x,y,t domain) into a depth image (x,y,z domain) is called seismic migration (Sheriff, 2002). The resolution of a migrated result is always limited, due to the finite bandwidth of the registered signals. Therefore the outcome of a migration process is a band-limited estimation of the reflectivity properties of the subsurface.

The design of source and detector positions to acquire the seismic data is the first step of the seismic experiment, the so-called seismic data acquisition. It aims at measuring data of sufficient quality to achieve the upstream objectives, e.g., high resolution images and accurate rock properties estimation at minimum cost. The resolution is governed by temporal and spatial bandwidths of the reflected energy. Besides, the acquired data have to contain low coherent and incoherent noise and preserve the signal fidelity. This thesis focuses on the design and analysis of seismic acquisition geometries in combination with the capability of utilizing multiple scattering in the data.

1.2 Acquisition analysis methods

1.2.1 Designing at the surface

Conventional 2D and 3D survey designs are largely based on common-midpoint processing that assumes a horizontally layered earth model. Therefore, the quality of an acquisition geometries is generally judged by surface attributes such as CMP fold, bin-size, minimum and maximum offset, azimuth range, frequency range, and spatial sampling intervals. There are traditional geometries that can encapsulate these parameters like areal, parallel, orthogonal, zig-zag and others. Cordsen et al. (2000), Galbraith (2004) and Vermeer (2012) describe these geometries and their properties in detail. There are two main aspects to look at while designing a 3D survey. The proposed geometry should handle the signal correctly in terms of resolution and amplitude fidelity. Secondly, the same geometry must somehow attenuate various types of noise which will be present. These two goals (record signal in an optimum way and attenuate noise as much as possible) should be achieved in a design process. Traditionally, the designer estimates the sampling parameters based on a 1D depth model for the target reflectors. However, if the macro subsurface model of the real earth deviates from a 1D model, seismic wavefields will be drastically different and the required layout of sources and detectors may be very different.

1.2.2 Designing including the subsurface model

Over the past few decades, it has become clear that model-based seismic acquisition design is the key to further increase the value of the seismic method for the oil and gas industry. This is particularly true in the case of complex subsurfaces. The subsurface-independent measures are just a first-order approach as the influence of the subsurface is critical in seismic acquisition design. After all, the subsurface determines how the seismic source wavefields travel from the surface to the (potential) reservoir and how the reflected waves travel from the reservoir area back to the detectors at the surface. Therefore, information about the subsurface must be taken into account in any advanced method for seismic acquisition analysis and design. In a completely virgin area, survey design parameters are still dependent on the conventional approach only because of non-availability of the subsurface information. However, in a more mature area, all available subsurface information can be exploited to improve the acquisition design especially for

time-lapse seismic surveys (Walters et al., 2006).

For a complex subsurface structure, the reflection points are no longer situated at the mid-point locations (Campbell et al., 2002). Therefore, the CMP analysis was replaced by the common-reflection-point (CRP) analysis where ray tracing is applied for a given macro-subsurface model. Counting the number of rays (the hit count) in each CRP bin yields attributes of fold, offset, and azimuth that are related to the CRPs at the target rather than to the CMPs at the surface. Examples of this approach can be found in Slawson et al. (1994), Muerdter and Ratcliff (2001) and Chang et al. (2002). This method can easily identify the poor CRP bin coverage and thus helps to improve the current acquisition parameters. However, this analysis counts only the total number of ray reflection points at a specific location, while it neglects the directional information of the raypath at that location. Therefore, relying on this method only, can be misleading.

To overcome this issue, Gibson and Tzimeas (2002) discuss quantitative measures of image resolution for seismic survey design based on Beylkin's approach to spatial image resolution (Beylkin, 1985). They developed a number of attributes such as quantitative image resolution measures of standard deviation, smoothness, wavenumber scatter plots and spatial images. They rightly point out that for good resolution (imaging and inversion) a whole range of raypaths is needed that meet each other at the subsurface point to be imaged. These ray-based methods can provide both the intensity and direction information carried in the wavefield. However, the high frequency asymptotic approximation and the singularity problem of the ray theory may severely limit its accuracy in complex regions (Hoffmann, 2001). Later on, Toxopeus et al. (2003), Laurain et al. (2004) and Xie et al. (2006) used wave-equation-based propagators to compute the range of wavenumbers at the subsurface point.

With the increase of computational power, it has been possible to carry out the full sequence of 3D modelling and migration (Jurick et al., 2003; Regone, 2006). However, fully simulating the seismic experiment and migrating the obtained synthetic seismic data is still a computationally intensive and laborious way to obtain direct measures for image quality at the target. There are methods by which the same information related to a particular target point can be obtained without this sequence of modelling and migration.

1.2.3 Focal beam method

A more efficient way is the so-called focal beam method, which was initially developed by Berkhout et al. (2001) and Volker et al. (2001), and later further expanded by van Veldhuizen et al. (2008) and Wei et al. (2012). It makes use of the so-called common focus point (CFP) technology (Berkhout, 1997a) in which a seismic response can be decomposed into grid-point responses, and the migration result can be simulated for a specific grid-point by double focusing (or bifocal imaging). This method enables accurate analysis for complex subsurfaces. It is a target-oriented method with a direct link to migration and reservoir characterization. As opposed to spatial resolution analysis, based on the theory of Beylkin (1985), which combines detector and source information, focal beams assess the detector and source parts of an acquisition geometry separately. Thus, both target illumination by the source distribution and target sensing by the detector distribution are obtained. Combining this information yields knowledge about the resolution of migrated data and about the accuracy of angle-dependent amplitude information. However, so far this method assumes primary reflections only as signal, leaving out multiple reflections as noise. In the next section, we discuss that multiples can be considered as signal in the seismic imaging if they are handled correctly. Therefore, we extend this focal beam method to the multiples as well in this thesis.

1.3 The era of using multiples as signal in imaging

The utilization of multiples in imaging and characterization is an emerging methodology. Multiples are waves that are reflected or scattered more than once at the subsurface interfaces and eventually end up at the seismic detectors. Multiples usually travel with longer wave paths and may cover larger areas than primaries in the subsurface. Very often, multiples can penetrate into the earth to illuminate the shadow zones which primaries cannot reach. In addition, multiples usually contain smaller reflection angles than primaries and provide the fine structures of the earth. Multiples are particular of interest for imaging poorly illuminated regions in the subsurface, especially below basalt and salt structures (see e.g. Liu et al., 2011). The motivations for using multiply scattered waves are to preserve the true amplitudes, provide extra illumination and improve the resolution of the reservoir images beyond current capability.

To illustrate the advantage of using all multiples, we use a salt model as shown in Figure 1.2a and compute the beam illumination due to a source laterally located at $x = 1200$ m at the surface (also indicated by the red star in Figure 1.2a). Figure 1.2b shows the illuminating energy beam by the primaries-only wavefield. It demonstrates how the structure of the salt body causes variations in the illuminating energy beam and creates shadow zones in the subsurface. Similarly, Figure 1.2c shows the illuminating energy beam due to the full wavefield, i.e., including the surface multiples and the internal multiples. The results clearly illustrate the concept of improved illumination by the generation of virtual sources as downgoing source wavefields, not only at the surface as surface-related multiples but also in the subsurface as internal multiples. The energy in the shadow zones is also filled partly by the multiples.

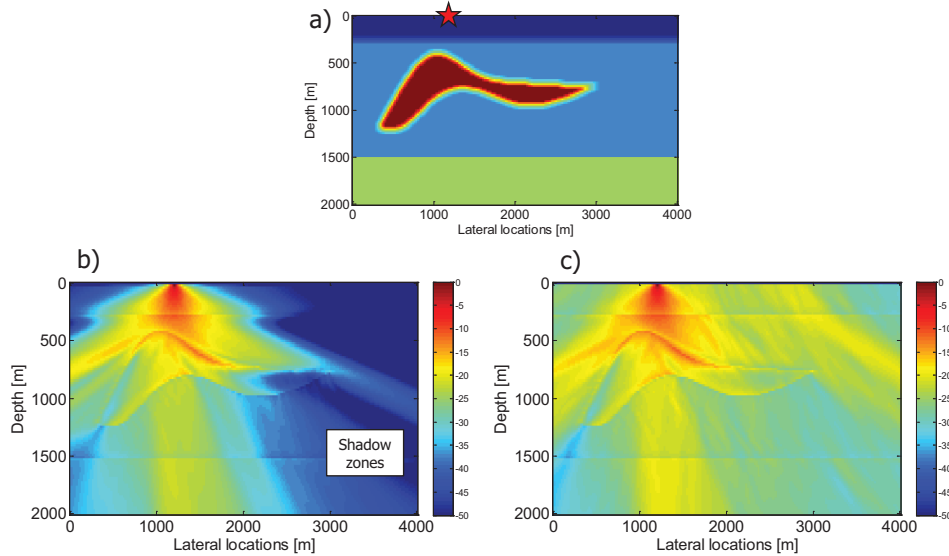


Figure 1.2: a) 2-D salt model example, red star indicates the source location, b) the illuminating energy beam due to the primaries-only wavefield created from one shot, c) same due to the full wavefield created from the same shot. Note the improved illumination utilizing all multiples, that can help to improve the resolution of the images.

Multiple removal or elimination has been an extensive topic of research. Traditionally these waves were suppressed, e.g., with multiple suppression technique (Foster and Mosher, 1992; ten Kroode, 2002), surface-related multiple elimination (Verschuur et al., 1992; Dragoset et al., 2010) and estimation of primaries by sparse inversion (van Groenestijn and Verschuur, 2009; Lopez

and Verschuur, 2013). In recent years, we have seen that the seismic industry is slowly shifting its emphasis from removing the multiples to using the multiples. The problem was that most migration techniques are based on the single-scattering assumption, which establishes a linear relation between the scattering contrasts in the Earth and the seismic data. This linear relation cannot explain multiply scattered events in the data. To utilize the multiply scattered events, we need a non-linear migration technique which can account for the fundamental non-linear relation between the model contrasts and the multiply scattered data. Over the last few years, the use of multiply scattered waves in seismic imaging has been discussed by many authors. The use of surface multiples in surface seismic with some interesting examples can be found in Berkhout and Verschuur (1994); Youn and Zhou (2001); Berkhout and Verschuur (2004); Brown and Guitton (2005); Dash et al. (2009); Lu et al. (2011); Zheng and Schuster (2014).

Similarly, some recent publications deal with using the internal multiples as an extra source of illumination. Malcolm et al. (2008) discussed an inverse scattering approach for imaging with different order of internal multiples independently. Vasconcelos et al. (2008) used interferometric principles for imaging internal multiples in a VSP geometry. Fleury (2013) proposed non-linear reverse time migration to extend the illumination using the internal multiples. More recently, Wapenaar et al. (2014a) and Slob et al. (2014) discussed the concept of Marchenko imaging to use information in internal multiples to improve seismic imaging. Berkhout (2012) introduced the concept of Full Wavefield Migration (FWM) that utilizes primaries and all multiples (both surface and internal multiples) in the observed data to estimate the subsurface reflectivity. Therefore, we consider this is an era of using multiples as a signal in the seismic imaging.

Now it is important to find what it means to the seismic data acquisition, e.g., by taking into account that illuminating wavefields are enhanced by the downward traveling multiple scattering (surface-related and internal), multiples may reach parts of the subsurface where primaries cannot come ('primary shadow zones'). This means the sparse sampling issues in the data acquisition would be compensated by utilizing surface and internal multiples. Therefore, an expensive data acquisition design with the 'symmetric sampling' concept (Vermeer, 2012) can be replaced by the concept of 'asymmetric sampling'.

1.4 Objective and outline of this thesis

1.4.1 Objective

The objective of this research is to implement the integrated approach to acquisition geometry analysis using the focal beam concept, including the information from all multiples. Therefore, we propose an image based acquisition analysis method to incorporate illumination by all multiples. It means when evaluating the performance of an acquisition geometry, we include the following items:

- dealing with a 3-D inhomogeneous complex subsurface;
- dealing with the direct wavefield, surface-related multiples and internal multiples;
- illumination from above as well as illumination from below;
- development of geophysical-based infill specifications to assess the impact of coverage holes on data quality.

Including all the above points may have an important effect on acquisition design, i.e., the acquisition effort may become less demanding. Bear in mind that acquisition geometry design aims at both the optimization of signal and the optimization of noise suppression. The analysis method presented in this thesis deals with the signal quality (e.g., primaries and all multiples). Noise suppression characteristics of the acquisition geometry - for example the requirements related to the attenuation of surface waves and linear noise are not considered. This could be the next step, by having the insight obtained from this research.

1.4.2 Outline

Chapter 2 is an introduction to seismic acquisition analysis for the Schoonebeek oil field in The Netherlands. The field was abandoned in 1996 because oil production was no longer economical at that time. However, with the increased oil price and the use of modern technology like horizontal drilling, high capacity pumping units and steam injection, NAM (Nederlandse Aardolie Maatschappij, a Shell/Exxon Mobil joint venture) reopened the Schoonebeek field in 2011 and expected to produce approximately 100 - 120 million barrels of oil over the next 25 years. The field is continuously

monitored with seismic equipment with the aim to follow the steam injection process. In this chapter, the focal beam acquisition analysis method is reviewed thoroughly and applied to the Schoonebeek geometry.

In **Chapter 3**¹ the focal beam method is extended to take into account the illumination properties of surface-related multiples as well. Often, the multiples illuminate the subsurface from other angles than the primaries and as such have the potential to improve the image quality. The practical use of the multiples as secondary sources in imaging means that we must know them, i.e., they must have been recorded. Consequently, the secondary sources can only be used where detectors are present. Hence, the detector locations are not only important for sensing, but also for illumination.

Chapter 4 presents a method by which not only the surface-related multiples but also the internal multiples can be included in the focal beam analysis. It discusses the illumination properties of primaries, surface-related multiples and internal multiples. A distinction is made between illumination from above and illumination from below: both directions of illumination contain information about the local reflectivity. It is interesting to notice that the use of the three types of waves (direct, surface-related multiples and internal multiples) together may illuminate the subsurface much better than the use of primaries only. Much better here means: some parts of the subsurface are only illuminated by surface-related and/or internal multiples, e.g., in subsalt regions. Other parts are illuminated from many more angles. The illumination study is related to the acquisition effort that is required to obtain the final seismic exploration goals.

In **Chapter 5** the extended focal beam method is illustrated further, by several examples featuring different subsurface situations and different types of acquisition geometries. The influence of an irregularly shaped salt structure on illumination strength due to the primaries-only and the full wavefield is studied. Furthermore, a 2-D example of full wavefield migration (FWM) is provided to show that multiples not only extend the illumination angles but also provide additional imaging subsurface points.

In **Chapter 6** we use the focal beam concept to assess the illumination capabilities of a marine acquisition geometry in the depth domain. In addition to calculating the resolution function, we introduce the concept of weighted

¹**Chapter 3** is part of an extended abstract presented at the 83rd Annual International Meeting, SEG (Kumar and Blacquière, 2013). **Chapters 4** and **5** are the part of journal paper Kumar et al. (2014b) accepted by *Geophysical Prospecting*. **Chapter 6** is part of journal paper submitted to *Geophysics* (Kumar et al., 2015).

focal source and detector beams that allows to conveniently assess the angular aperture available for a specific acquisition configuration at the considered depth point. We also apply the method to the problem of coverage deficiencies that can occur when the survey geometry deviates from the ideal, for example due to feathering.

Chapter 7 contains the conclusions of this research, and recommendations for future developments.

Chapter 2

Theory of model-based acquisition design: The Schoonebeek field example

2.1 Introduction

The previous chapter presented general rules to define an initial acquisition geometry, the first phase of the design process. In the next phase the subsurface model needs to be incorporated. The main objective of this design phase is to evaluate the interaction between the acquisition geometry and the subsurface model as an optimization process. This evaluation is quantified by the quality of the imaging results. It is important to know the limitations of the processing tools in order not to interpret processing deficiencies as being caused by the acquisition geometry. For instance, if the used imaging algorithm has dip limitation, then the final image will not contain information pertaining to high angles even if they are contained in the acquired data. Hence, the interaction between the acquisition geometry and the processing algorithm should be included in this optimization process. Therefore, it is important to establish an assessment methodology that can separate acquisition geometry effects on imaging results from other effects. The so-called **WRW** model (Berkhout, 1982) is well suited for this task because the acquisition geometry is explicitly included in the forward model of the seismic experiment. The imaging technique (migration method) has to be fixed while evaluating different geometries. Similarly, we can evaluate different imaging techniques while keeping the acquisition geometry fixed. Furthermore, we

can evaluate a preferred combination of acquisition geometry and imaging technique as well.

The concept of focal beams allows assessing the effects of an acquisition geometry on the image quality for a given subsurface macro-model, without going into explicit modelling of seismic data. This is achieved through the utilization of focal beams and the focal functions. A large part of the theory of focal beam analysis has been developed and described by Berkhou et al. (2001); Volker et al. (2001); Volker (2002) and van Veldhuizen et al. (2008). In this chapter the concept of focal beams will be explained, preceded by an explanation of the operator notation (van Veldhuizen et al., 2008). The results of the focal beam analysis are illustrated in detail with the help of the Schoonebeek oil-field example.

2.2 Operator notation

Throughout this thesis, an operator notation is used to express all the mathematical derivations. The operators are represented by matrices and vectors. In the continuous situation, the operators represent integrals. In practice however, the data of a seismic survey is always characterized by a discrete spatial sampling of the wavefield. In addition, the computer works with discrete data. Therefore, this notation is very suitable. Also it hides trivial mathematical details from the reader. The notation convention will be as follows:

- Matrices are indicated with capital bold symbols, for example \mathbf{P} .
- Vectors are indicated by capital italic symbols having a vector sign on top of that symbol and a subscript. The subscript indicates which row or column is taken. The distinction between a row vector and a column vector is made by using a dagger superscript ' \dagger ' when the vector is a row vector:
 - \vec{P}_j is the j^{th} column of matrix \mathbf{P} .
 - \vec{P}_j^\dagger is the j^{th} row of matrix \mathbf{P} .
- An element of a matrix is indicated by two subscripts, one that indicates the row and one that indicates the column: P_{ij} is the element on the i^{th} row and j^{th} column of matrix \mathbf{P} .

- Matrices, vectors and elements are formulated per temporal radial frequency component ω , but this symbol is omitted for convenience.
- The reference depth levels of a matrix or a vector are indicated between the parentheses that accompany the matrix. For instance, $\mathbf{W}^-(z_0, z_m)$ describes the upward wave propagation from depth level z_m to the surface z_0 .
- The superscripts '+' and '-' represent the downward and upward direction, respectively.
- The small delta symbol with a subscript (' δ_k ') in-front of any bold symbols refers to data related to one point scatterer.
- The capital delta sign (Δ) in-front of any bold symbols (e.g., $\Delta\mathbf{P}$) refers to data for a unit reflector.

2.3 Representation of seismic data

The data of a seismic survey (2D or 3D) can be conveniently arranged with the aid of the so-called data matrix $\mathbf{P}(z_d; z_s)$ in the temporal frequency domain (Berkhout, 1982). Each element of this matrix represents one frequency component of the signal recorded by a detector (array) at depth level z_d generated by a source (array) at depth level z_s . Note that this matrix can describe both 2-D and 3-D situations (Kinneging et al., 1989). If we take $z_d = z_s = z_0$, where z_0 denotes the surface level, then using the operator notation, the monochromatic expression for primary reflections related to depth level z_m can be written as:

$$\vec{P}_j(z_0; z_0) = \mathbf{D}^{[j]}(z_0) \mathbf{W}^-(z_0, z_m) \mathbf{R}^{\cup}(z_m, z_m) \mathbf{W}^+(z_m, z_0) \vec{S}_j(z_0). \quad (2.1)$$

Figure 2.1 schematically demonstrated the forward model. The symbols in equation (2.1) are described as follows:

- $\vec{S}_j(z_0)$: represents the source wavefield at the j^{th} shot location. It is the j^{th} column vector of source matrix $\mathbf{S}(z_0)$. Each column of this matrix corresponds to the downgoing source wavefield at z_0 due to one source (array) and each row corresponds to a certain lateral position along the acquisition surface.
- $\mathbf{W}^+(z_m, z_0)$: forward wavefield propagation matrix. Each column contains discrete version of the derivative of Green's function describing

wave propagation from one lateral location at the surface z_0 to many lateral locations at depth level z_m .

- $\mathbf{R}^U(z_m, z_m)$: reflectivity matrix, describing the conversion of an incident wavefield into a reflected wavefield. The superscript ' U ' indicates that the reflection turns a downward traveling wavefield into an upward traveling wavefield.
- $\mathbf{W}^-(z_0, z_m)$: forward wavefield propagation matrix. Each column contains discrete version of the derivative of Green's function describing wave propagation from one lateral location at the reflection level z_m to many lateral locations at the surface z_0 . Figure 2.2 shows systematically the representation of forward propagation matrices.
- $\mathbf{D}^{[j]}$: represents the detector matrix. Each row corresponds to one detector (array) and each column corresponds to a detector lateral position. Therefore, each element of the detector matrix shows the detector signature at a particular location. Assuming that detectors are measuring the wavefield exactly as it arrives at the acquisition surface, $\mathbf{D}^{[j]}$ is a unit matrix, i.e., a diagonal matrix with unit elements. Since the detector matrix may vary as function of the source coordinate (x_j, y_j, z_0) , it is denoted as $\mathbf{D}^{[j]}$.

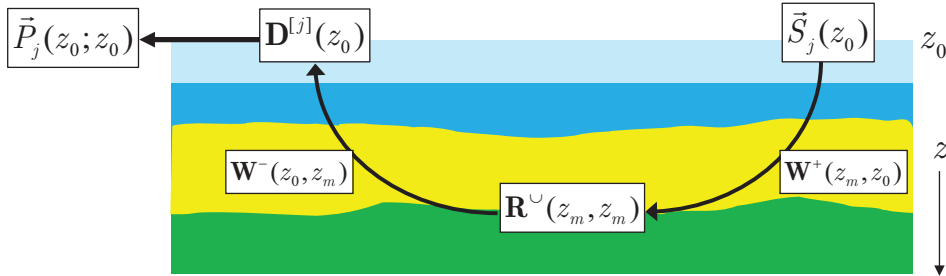


Figure 2.1: System representation of seismic data for primary reflections.

The result of the matrix multiplications in equation (2.1) is a single column vector \vec{P}_j , which represents one shot record. The data matrix for the whole survey is given by:

$$\mathbf{P}(z_0; z_0) = [\vec{P}_1, \vec{P}_2, \dots, \vec{P}_j, \dots, \vec{P}_J]. \quad (2.2)$$

The source location varies along the row direction and the detector location varies along the column direction. Note that, for simplicity, the reflections

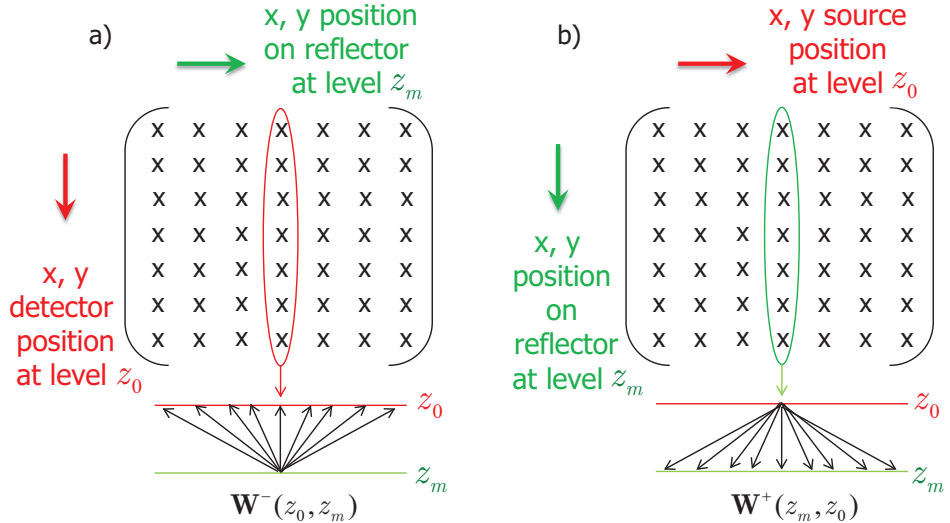


Figure 2.2: The schematic representation of forward propagation matrices. a) $\mathbf{W}^-(z_0, z_m)$ is a forward propagation matrix, which propagates from reflector level z_m to the detector level z_0 , b) similarly, $\mathbf{W}^+(z_m, z_0)$ is a forward propagation matrix, which propagates from the source level z_0 to the reflector level z_m .

for one depth are considered only. In order to obtain the seismic response of the whole subsurface, a summation over all depth levels has to be carried out and transmission effects should be incorporated in \mathbf{W}^+ and \mathbf{W}^- (Berkhout, 2014b). Forward propagation matrices \mathbf{W}^+ and \mathbf{W}^- are given by the recursive expressions:

$$\mathbf{W}^+(z_m, z_0) = \prod_{n=m}^1 \mathbf{W}^+(z_n, z_{n-1}) \text{ and} \quad (2.3a)$$

$$\mathbf{W}^-(z_0, z_m) = \prod_{n=1}^m \mathbf{W}^-(z_{n-1}, z_n), \quad (2.3b)$$

with the columns of $\mathbf{W}^+(z_n, z_{n-1})$ and $\mathbf{W}^-(z_{n-1}, z_n)$ being determined by the user-specified local velocity. Note that multiplications (2.3a and 2.3b) involve space-variant spatial convolution along the lateral coordinates. Without lateral velocity changes, convolutions are multiplications in the wavenumber domain, with $\tilde{\mathbf{W}}^+(z_n, z_{n-1})$ and $\tilde{\mathbf{W}}^-(z_{n-1}, z_n)$ being the phase-shift operators (see also Appendix A).

In the case of marine streamer geometries, the location of the detectors is different for each source position. Therefore, equation (2.2) represents the seismic data exactly the way it is acquired for marine streamer geometries. The schematic representation of the data matrix for this case can be seen in Figure 2.3a. Here, each shot has been recorded to its corresponding live detectors and then a 'roll-along' distance is applied. Due to this effect, the data matrix has a typical 'band-type' structure with many zero elements.

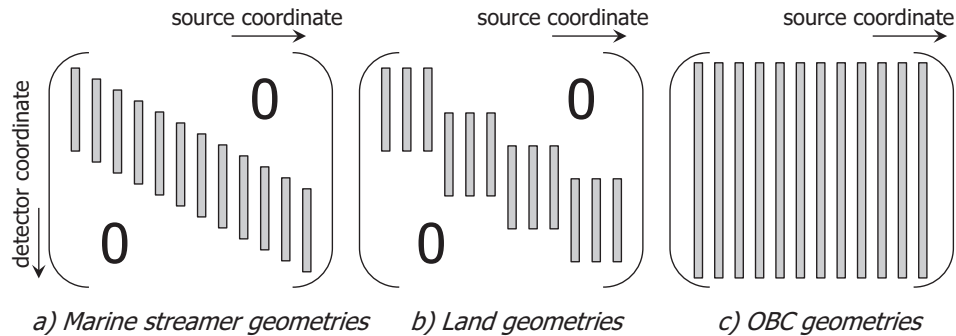


Figure 2.3: Schematic representation of the data matrix for a) marine streamer geometry, b) land geometry and c) OBC geometry.

For land geometries, there are usually several shots fired in the same detector spread, called template. The seismic response from one template can be modeled using the following equation:

$$\mathbf{P}^{[n]}(z_0; z_0) = \mathbf{D}^{[n]}(z_0) \mathbf{W}^-(z_0, z_m) \mathbf{R}^{\cup}(z_m, z_m) \mathbf{W}^+(z_m, z_0) \mathbf{S}^{[n]}(z_0), \quad (2.4)$$

where superscript n represents the n^{th} template. The source matrix \mathbf{S} represents the shot-configuration in a template. The matrix \mathbf{P} is a sub-matrix of the data matrix \mathbf{P} . The data matrix for the total survey is given by:

$$\mathbf{P}(z_0; z_0) = \left[\mathbf{P}^{[1]}, \mathbf{P}^{[2]}, \dots, \mathbf{P}^{[n]}, \dots, \mathbf{P}^{[N]} \right]. \quad (2.5)$$

The schematic representation of the data matrix for land geometries is shown in Figure 2.3b, where three shots have been fired to the same detector spread. The extreme case is the ocean bottom cable (OBC) or ocean bottom node (OBN) geometry, where all shots are fired in the same detector spread. In that case, the data matrix can be written as:

$$\mathbf{P}(z_0; z_0) = \mathbf{D}(z_0) \mathbf{W}^-(z_0, z_m) \mathbf{R}^{\cup}(z_m, z_m) \mathbf{W}^+(z_m, z_0) \mathbf{S}(z_0). \quad (2.6)$$

Note that in this case, the data matrix will contain non-zero elements only as shown in Figure 2.3c. Such geometries are called stationary. This can be considered as a full-fold acquisition geometry from which any geometry can be obtained by applying a mask to the data matrix. In the streamer geometry case, although the streamer is moving, each shot with its corresponding live detectors can be considered to be a stationary part of the survey in a good approximation.

2.4 Grid-point response

The focal beam analysis makes use of the so-called common focus point (CFP) technology (Berkhout, 1997a) in which a seismic response can be composed from grid-point responses, and the migration result can be simulated for a specific grid-point by double focusing. The seismic response $\mathbf{P}(z_0; z_0)$ can be written as superposition of all grid-point responses, as follows:

$$\mathbf{P}(z_0; z_0) = \sum_k \delta_k \mathbf{P}(z_0; z_0), \quad (2.7)$$

where $\delta_k \mathbf{P}(z_0; z_0)$ represents the k^{th} grid-point response. As discussed, the reflectivity matrix $\mathbf{R}^U(z_m, z_m)$ describes the angle-dependent reflection at depth level z_m . Each column or row of this matrix contains the angle-dependent reflection operator of one grid-point at the reflecting surface z_m . A linear Radon transform of such an operator shows the individual reflection coefficient for each angle of incidence. If the reflectivity is angle-independent, \mathbf{R}^U is a diagonal matrix. In any case, the reflectivity matrix \mathbf{R}^U can be written as a sum of grid-point reflectivity matrices as follows:

$$\mathbf{R}^U(z_m, z_m) = \sum_k \delta_k \mathbf{R}^U(z_m, z_m), \quad (2.8)$$

where $\delta_k \mathbf{R}^U(z_m, z_m)$ represents the angle-independent grid-point reflectivity matrix for the lateral location $(x, y)_k$ at depth level z_m . It has only one nonzero element, located on its diagonal. Figure 2.4 explains how the elements of the reflectivity matrix are filled in the cases of angle-dependent, angle-independent and angle-independent grid-point reflectivity, respectively. An extensive discussion on the reflectivity matrix can be found in De Bruin et al. (1990).

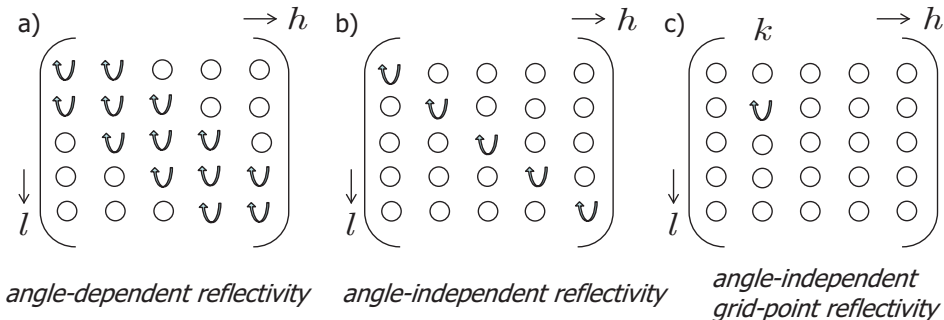


Figure 2.4: a) Angle-dependent reflectivity matrix (some off-diagonals elements are also filled), b) angle-independent reflectivity matrix (only diagonal elements are filled) and c) angle-independent grid-point reflectivity (only the k^{th} diagonal element of the matrix is filled). The letters h and l indicate the lateral locations varying at the target depth level z_m .

Subsequently, the monochromatic response for an angle-independent grid-point response can be written as :

$$\delta_k \vec{P}_j(z_0; z_0) = \mathbf{D}^{[j]}(z_0) \mathbf{W}^-(z_0, z_m) \delta_k \mathbf{R}^{\cup}(z_m, z_m) \mathbf{W}^+(z_m, z_0) \vec{S}_j(z_0). \quad (2.9)$$

In the case of a stationary detector geometry, the grid-point response for all J sources at the surface can be expressed as:

$$\delta_k \mathbf{P}(z_0; z_0) = \mathbf{D}(z_0) \mathbf{W}^-(z_0, z_m) \delta_k \mathbf{R}^{\cup}(z_m, z_m) \mathbf{W}^+(z_m, z_0) \mathbf{S}(z_0). \quad (2.10)$$

The discussion about non-stationary geometries is provided in chapter 6. The matrix $\delta_k \mathbf{P}(z_0; z_0)$ contains the multirecord response of the point diffractor as well as the properties of the acquisition geometry (**D** and **S**). In the focal beam method, one of the aims is to find the angle-dependent effects introduced by the acquisition geometry (**D** and **S**), irrespective of any angle-dependent reflection properties at the target level (van Veldhuizen et al., 2008; Kumar et al., 2014a). Therefore, the grid-point responses $\delta_k \mathbf{P}(z_0; z_0)$ in the modeling are chosen to be angle-independent, i.e., they are responses due to unit point diffractors. This means the element of the grid-point reflectivity matrix ($\delta_k \mathbf{R}^{\cup}$) is chosen to have unit value when used in our focal beam analysis method.

2.5 Imaging

The next step in calculating the focal beams is to perform bifocal imaging of a grid-point response. In this approach, migration is described in terms of double focusing (Berkhout, 1997a,b), i.e, focusing in detection and focusing in emission, followed by the imaging principle (or selecting $t = 0$ s). The double focusing result for the primaries-only grid-point response (see equation 2.10) can be written as:

$$\delta_k \mathbf{P}(z_m; z_m) = \mathbf{F}(z_m, z_0) \delta_k \mathbf{P}(z_0; z_0) \mathbf{F}(z_0, z_m), \quad (2.11)$$

$$\delta_k \mathbf{P}(z_m; z_m) = \mathbf{F}(z_m, z_0) \mathbf{D}(z_0) \mathbf{W}^-(z_0, z_m) \delta_k \mathbf{R}^\cup(z_m, z_m) \times \\ \mathbf{W}^+(z_m, z_0) \mathbf{S}(z_0) \mathbf{F}(z_0, z_m). \quad (2.12)$$

In the above expression, matrix \mathbf{F} represents the focusing operator which aims to remove $\mathbf{W}^+(z_m, z_0) \mathbf{S}(z_0)$ and $\mathbf{D}(z_0) \mathbf{W}^-(z_0, z_m)$ from the data such that the undisturbed reflection properties (position and reflectivity) are obtained. The equation (2.12) is the double focusing result as shown in Figure 2.5 for one reflecting depth level z_m .

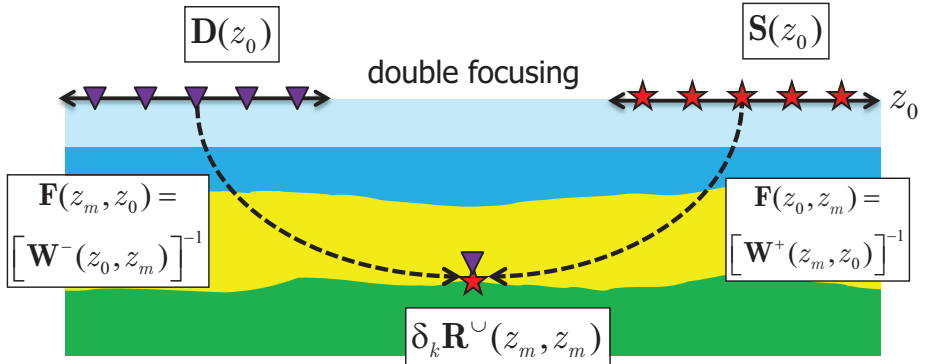


Figure 2.5: Focusing in detection and focusing in emission to a depth level z_m positions a virtual detector and a virtual source on a reflecting boundary.

The perfect migration would require focusing operators \mathbf{F} such that:

$$\begin{aligned} \mathbf{F}(z_m, z_0) \mathbf{D}(z_0) \mathbf{W}^-(z_0, z_m) &= \mathbf{I}, \\ \mathbf{F}(z_m, z_0) &= [\mathbf{W}^-(z_0, z_m)]^{-1} [\mathbf{D}(z_0)]^{-1}. \end{aligned} \quad (2.13)$$

and

$$\begin{aligned}\mathbf{W}^+(z_m, z_0)\mathbf{S}(z_0)\mathbf{F}(z_0, z_m) &= \mathbf{I}, \\ \mathbf{F}(z_0, z_m) &= [\mathbf{S}(z_0)]^{-1}[\mathbf{W}^+(z_m, z_0)]^{-1}.\end{aligned}\quad (2.14)$$

The above equations suggest that the computation of the focusing operators would require an exact inverse of one-way forward propagator matrix \mathbf{W} . However, ignoring the evanescent waves and transmission effects, focusing operator \mathbf{F} can be well approximated as the complex conjugate of forward extrapolation matrix \mathbf{W} as $\mathbf{F} = \mathbf{W}^{-1} \approx \mathbf{W}^H$. This property makes it possible to carry out bifocal imaging in a direct way. The superscript ' H ' in \mathbf{W}^H represents the Hermitian of a matrix. It is to be noted that although \mathbf{F} can be well approximated by \mathbf{W}^H , the influence of \mathbf{D} and \mathbf{S} is still present. However, this is exactly what we want to assess: the effects of the acquisition geometry. Applying the imaging principle to the result of equation (2.12) results in the migration response of the k^{th} grid-point, i.e., it results in an estimate of the angle-dependent reflection properties of the grid-point. Knowing that this response is angle independent, all angle dependency found must have been introduced by the acquisition geometry.

Basically, by double focusing, the data matrix $\delta_k \mathbf{P}(z_0; z_0)$ is downward extrapolated to the depth level of the involved grid-point, resulting in the so-called grid-point matrix $\delta_k \mathbf{P}(z_m; z_m)$. As mentioned before, $\delta_k \mathbf{R}^U(z_m, z_m)$ is to be an unit angle-independent point diffractor when used in focal beam analysis. Therefore, it can be expressed as a matrix multiplication of two unit vectors as follows:

$$\delta_k \mathbf{R}^U(z_m, z_m) = \vec{I}_k(z_m, z_m) \vec{I}_k^\dagger(z_m, z_m), \quad (2.15)$$

therefore, the double focusing result (equation 2.12) can be expressed as follows:

$$\begin{aligned}\delta_k \mathbf{P}(z_m; z_m) &= \left[\mathbf{F}(z_m, z_0) \mathbf{D}(z_0) \vec{W}_k(z_0, z_m) \right] \left[\vec{W}_k^\dagger(z_m, z_0) \mathbf{S}(z_0) \mathbf{F}(z_0, z_m) \right], \\ &= \vec{D}_k(z_m, z_m) \vec{S}_k^\dagger(z_m, z_m).\end{aligned}\quad (2.16)$$

where $\vec{D}_k(z_m, z_m)$ and $\vec{S}_k^\dagger(z_m, z_m)$ represent the focal detector beam (a column vector) and the focal source beam (a row vector) for the k^{th} grid-point, respectively. The superscripts '+' and '-' from the wave propagation term \mathbf{W} have been removed now for simplicity. The expression for the focal detector beam and the focal source beam at depth level z_m can be expressed as follows:

$$\vec{D}_k(z_m, z_m) = \mathbf{F}(z_m, z_0) \mathbf{D}(z_0) \vec{W}_k(z_0, z_m), \quad (2.17)$$

$$\vec{S}_k^\dagger(z_m, z_m) = \vec{W}_k^\dagger(z_m, z_0) \mathbf{S}(z_0) \mathbf{F}(z_0, z_m). \quad (2.18)$$

The focal detector beam shows how the detector geometry affects focusing, and the focal source beam shows how the source geometry affects focusing. This offers an opportunity to judge and adjust the configuration of sources and detectors separately. In an ideal situation, when all influence of acquisition geometry and propagation is perfectly removed by focusing, the focal source beam at depth level z_m is a row vector where the k^{th} element is the only one non-zero element, i.e., $\vec{S}_k^\dagger(z_m) = \vec{I}_k^\dagger(z_m)$, and the focal detector beam at depth level z_m is a column vector where the k^{th} element is the only one non-zero element, i.e., $\vec{D}_k(z_m) = \vec{I}_k(z_m)$. However, this is not the case in practice because of constraints of the acquisition geometry given by a coarse spatial sampling, limited apertures, imperfect migration operators and because of limitations imposed by the evanescent field. These limitations allow us to analyze the acquisition geometry imprint via focal beams.

Similar to retrieving angle-dependent information from the reflectivity matrix \mathbf{R}^\cup in the Radon domain (De Bruin et al., 1990), a plane-wave decomposition of the focal beams by means of a linear Radon transform reveals the angles by which the target point is illuminated (source beam) or sensed (detector beam). For the mathematical formulation of the focal beams in the Radon domain, readers are referred to van Veldhuizen (2006).

2.6 Focal functions

Angle-averaged (structural) imaging and angle-dependent imaging encapsulate the primary purpose of seismic imaging. For structural imaging, the resolution is important while for angle-dependent imaging the range of reflection angles is important. Based on these two requirements, Berkhouwt et al. (2001) identified two focal functions: the resolution function and the amplitude-versus-ray parameter (AVP) function.

2.6.1 Resolution function

The response of an angle-independent reflector can be considered as a response of a distribution of point diffractors. For a given acquisition geometry, the seismic response of a point diffractor can be modeled and imaged to evaluate the resolution. However, it will be shown here that the focal beams can be used to perform this task without going into explicit modeling of the data.

The resolution can be evaluated by double focusing of a grid-point response (equation 2.10) where both detectors and sources are focused at the same subsurface point as follows:

$$\delta_k P_{ii}(z_m; z_m) = \vec{F}_i^\dagger(z_m, z_0) \mathbf{D}(z_0) \mathbf{W}^-(z_0, z_m) \delta_k \mathbf{R}^\cup(z_m, z_m) \times \mathbf{W}^+(z_m, z_0) \mathbf{S}(z_0) \vec{F}_i(z_0, z_m). \quad (2.19)$$

Again since $\delta_k \mathbf{R}^\cup(z_m, z_m)$ has only one non-zero element at the k^{th} lateral position, the above equation can be rewritten as:

$$\begin{aligned} \delta_k P_{ii}(z_m, z_m) &= [\vec{F}_i^\dagger(z_m, z_0) \mathbf{D}(z_0) \vec{W}_k(z_0, z_m)] [\vec{W}_k^\dagger(z_m, z_0) \mathbf{S}(z_0) \vec{F}_i(z_0, z_m)] \\ &= D_{ik}(z_m, z_m) S_{ki}(z_m, z_m). \end{aligned} \quad (2.20)$$

where i varies around the position of the point diffractor k . Equation (2.20) represents the resolution function and it shows that it can be obtained by space-frequency element-by-element multiplication of the focal detector and the focal source beam defined in equations (2.18) and (2.17).

From the multiplication rule of the source and the detector beam it can be concluded that the source and detector geometry can be designed in such a way that they complement each other. Side lobes due to the source geometry can be suppressed by the detector geometry and vice-versa. Note that the resolution function is formulated here for a single frequency component. If a seismic frequency band is considered, the resolution function is obtained by applying an imaging condition, i.e., by summing all monochromatic resolution functions.

The resolution function shows how well a point diffractor at the subsurface gridpoint under consideration can be resolved laterally. Several authors wrote about resolution estimation for acquisition geometries while considering homogeneous subsurface velocity models. See for example von Seggern (1994), and Vermeer (1999). All authors considered the main lobe of the resolution while not paying attention to the importance of side lobes (Volker, 2002). Most of the differences in resolving power of acquisition geometries are contained in the side lobes. In general, if aliasing criteria are taken into consideration, the main lobe of the focal resolution function can be reduced by increasing the aperture. The side lobes can be reduced by reducing the sampling intervals. However, the last two points are valid only in the absence of major shadow zones where there are no illumination problems. The influence on the vertical image resolution, and the artifacts occurring at different depth levels, can be assessed by computing the resolution functions for a range of depth levels.

2.6.2 AVP function

Apart from the resolution, it is also possible to investigate the influence of a given acquisition geometry on the AVP-information in the data. The main objective of the AVP function is to evaluate the effects of the acquisition geometry on the angle-dependent reflectivity contained in the acquired seismic data. Therefore, we will take an angle-independent reflector with zero dip - i.e., $\mathbf{R}(z_m, z_m) = \mathbf{I}$ with ones on the main diagonal and zeros elsewhere in order to separate the acquisition geometry effects from angle dependency variations. Therefore, the AVP-function represents the imprint of the acquisition geometry on the unit sampling comb of the reflectivity function. According to this assumption, the forward model of an angle-independent unit reflector can be written as:

$$\begin{aligned}\Delta \mathbf{P}(z_0, z_0) &= [\mathbf{D}(z_0) \mathbf{W}^-(z_0, z_m)] \mathbf{R}^\cup(z_m, z_m) [\mathbf{W}^+(z_m, z_0) \mathbf{S}(z_0)] \\ &= [\mathbf{D}(z_0) [\mathbf{W}^-(z_0, z_m)] \mathbf{I}(z_m, z_m) [\mathbf{W}^+(z_m, z_0)]] \mathbf{S}(z_0) \\ &= [\mathbf{D}(z_0) [\mathbf{W}^-(z_0, z_m)]] [\mathbf{W}^+(z_m, z_0)] \mathbf{S}(z_0).\end{aligned}\quad (2.21)$$

The capital delta sign (Δ) added to the symbol \mathbf{P} indicates that it is for a unit reflector. The AVP matrix can be obtained by focusing from both side as:

$$\begin{aligned}\Delta \mathbf{P}(z_m; z_m) &= [\mathbf{F}(z_m, z_0) \mathbf{D}(z_0) \mathbf{W}^-(z_0, z_m)] [\mathbf{W}^+(z_m, z_0) \mathbf{S}(z_0) \mathbf{F}(z_0, z_m)] \\ &= \mathbf{D}(z_m, z_m) \mathbf{S}(z_m, z_m),\end{aligned}\quad (2.22)$$

where $\mathbf{D}(z_m, z_m)$ represents the focal detector beam matrix and $\mathbf{S}(z_m, z_m)$ represents the focal source beam matrix, respectively. The AVP matrix is a matrix filled with non-zero elements as shown in Figure 2.6. The AVP function for the k^{th} subsurface gridpoint can be obtained by the k^{th} row or column of the AVP matrix as follows:

$$\vec{\Delta}P_k^\dagger(z_m; z_m) = \vec{D}_k^\dagger(z_m, z_m) \mathbf{S}(z_m, z_m), \quad (2.23a)$$

$$\vec{\Delta}P_k(z_m; z_m) = \mathbf{D}(z_m, z_m) \vec{S}_k(z_m, z_m). \quad (2.23b)$$

Equations (2.23a and 2.23b) show that the AVP function is obtained by using one focal source beam for grid point k and many focal detector beams for all grid points. It is a matrix-vector multiplication or space-variant convolution operation. In practice the computation of the AVP function is simplified by assuming that the focal detector beam does not vary as a function of location l around the target point k . In that case it becomes a space-invariant convolution operation and this convolution of the focal detector and source

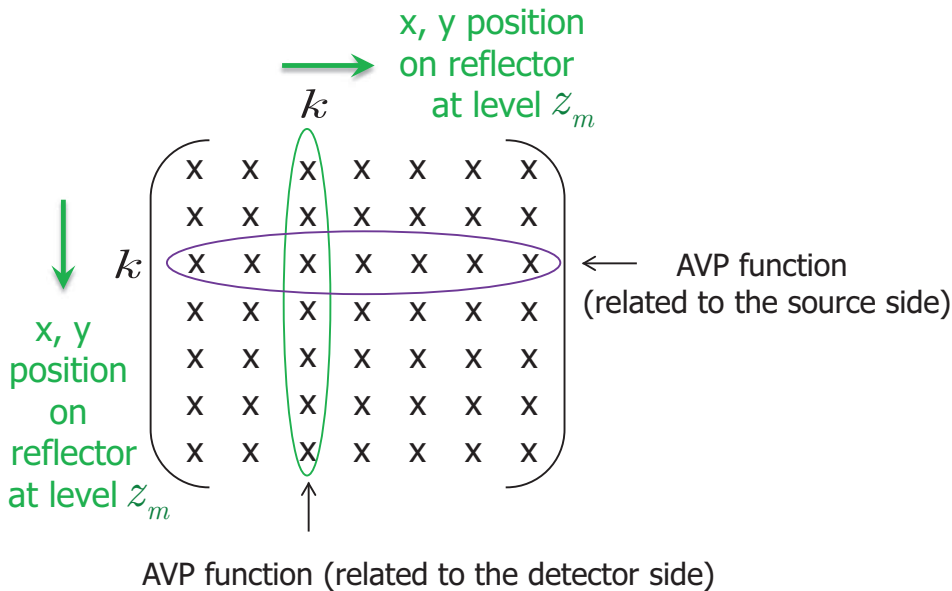


Figure 2.6: Schematic representation of the AVP matrix, where k^{th} column or row is AVP function.

beams can be written as a multiplication of two focal beams in the Radon domain.

The AVP function shows the range of dip angles, their strengths and their azimuths for one target point that will be present in the data i.e., the angles that have been illuminated and detected. Remember that the AVP function reveals how the reflectivity at the target is sampled. Therefore, the designer should know the range of angles that need to be adequately sampled at the target interfaces. This is a function of the elastic properties at these interfaces. The required angles should be at least those that would allow proper inversion for the elastic properties. This information should be provided by the reservoir characterization. Having determined the range of angles that have to be present in the pre-stack data, the designer should seek a uniform unit amplitude AVP function over such range.

The computation of focal beams and focal functions assumed that the target reflector has a zero dip, i.e, a horizontal reflector. However, the local reflector dip can easily be included in the computation. When the target reflector has

dip, the angles of illumination and the angles of detection change according to this dip. To take this into account, a ray parameter shift can be applied to the focal detector beam and the focal source beam in the Radon domain prior to multiplication. For more detail about the focal beams for dipping reflectors, the reader is referred to van Veldhuizen (2006). The main results from this section are summarized in the Figure 2.7.

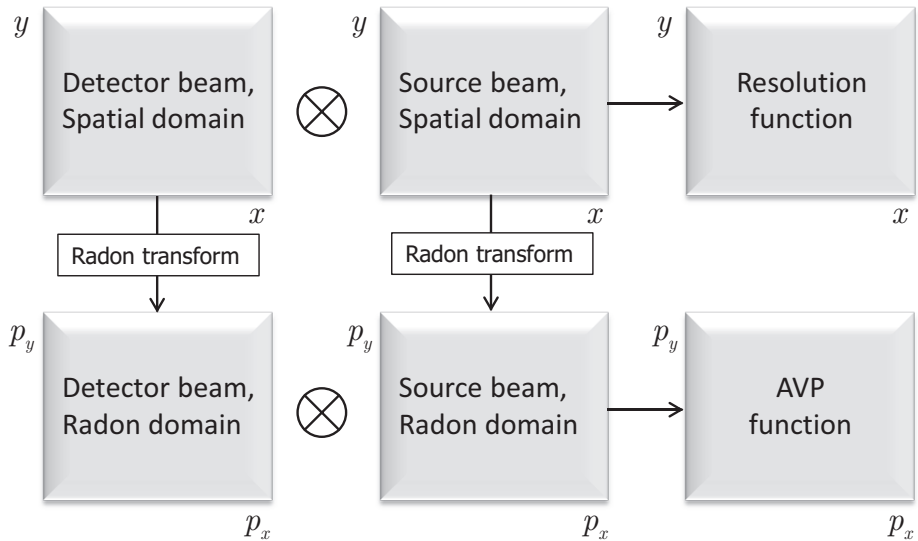


Figure 2.7: The relation between the focal detector beam, the focal source beam and the focal functions. p_x and p_y are the horizontal ray parameter components. The \otimes are element-by-element multiplications. Note that the AVP function is not the Radon transformation of the resolution function.

2.7 The ideal focal beams and ideal focal functions

The theory of focal beam analysis has been explained in the previous sections. The next step is to interpret the observed effects in the focal beams and the focal functions. In the ideal case, a focal beam that is computed at target depth will show one narrow peak at the location of the target point. It shows the forward and reverse wavefield extrapolation of a point diffractor response. When the extrapolation operators have a flat amplitude spectrum, the theoretically best attainable result is a spatially band-limited delta pulse.

In practice, this would be a sinc function in the two dimensional case and Bessel function scaled with the inverse distance from the target point location in the three dimensional case, respectively (Berkhout, 1984).

The ideal focal beam in the spatial domain as well as in the Radon domain is illustrated in Figure 2.8. The target point is located at $(x,y) = (0,0)$. It shows a band limited delta function at the target point in the spatial domain. The Radon-transformed focal beam shows a constant amplitude of all azimuths and angles, up to a maximum angle of 90° . In the Radon domain the focal beam is displayed as function of the horizontal ray parameter components p_x and p_y at zero intercept time. This means it is indirectly displayed as a function of azimuth and angle. The center of Figure 2.8b corresponds to normal incidence, from the center outward the angle increases. The different directions that can be chosen when moving from the center outward represent the different azimuths. A larger bandwidth in the Radon domain, meaning larger angles, will enable a better velocity estimation. Uniformity of the amplitude will avoid biasing of the angle-dependent reflection information in the data.

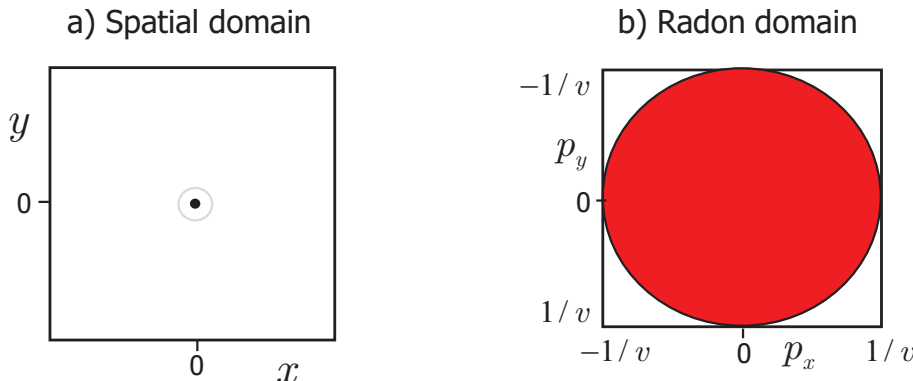


Figure 2.8: Ideal focal beams at target level. Figure a) shows the focal beam in the spatial domain, where the target point is at $(x,y) = (0,0)$. Figure b) shows the focal beam in the Radon domain at zero intercept time. p_x and p_y are lateral ray parameter components. The maximum value of p_x and p_y is the slowness at the target, $1/v$, where v is the wave velocity. This corresponds to an angle of 90° .

The ideal resolution function is the element-by-element product of an ideal focal detector beam and an ideal focal source beam. Therefore in three dimensions, it is the product of two Bessel functions both divided by their

argument. The analytical expression of the resolution functions for ideal acquisition and for cross-spread data is discussed in Wapenaar (1997). Being the product of the Radon transformed focal source beam and focal detector beam, ideally the AVP function shows a constant amplitude for all azimuths and angles upto the maximum angle of 90°. This would require a large acquisition aperture and dense surface sampling for both sources and detectors.

2.8 Introduction to the Schoonebeek oil field

The Schoonebeek oil field is the largest onshore oil field in North-Western Europe. The field was discovered in 1943. The reservoir of Schoonebeek field is mainly Bentheim Sandstone (Lower Cretaceous), clean sand and shore face sandstone of around 20 m thickness. Between 1948-1996, the field produced 250 million barrels of oil. The oil initially in place was one billion barrels. Production was halted in 1996 because it was no longer economical, but with the use of modern technology like horizontal drilling, high capacity pumping units and steam injection, NAM (Nederlandse Aardolie Maatschappij), a Shell/Exxon Mobil joint venture reopened the Schoonebeek field in 2011 and expects to produce approximately 100 - 120 million barrels of oil over the next 25 years.

In December 2010, NAM started time-lapse seismic reservoir monitoring to image the fluid flow using Seismovie, a CGGVeritas' solution to high-resolution onshore reservoir monitoring. In Seismovie, with the use of buried sources and buried detector arrays, data is acquired continuously and autonomously to provide a seamless, high resolution movie of a reservoir.

To know the time-lapse seismic attributes, seismic experiments were done using two detector lines and one source line. With this configuration a field trial was carried out to demonstrate the feasibility to monitor the reservoir changes. In the first quarter of 2012, this newly seismic experiment was proposed with 5 detector lines and 3 source lines (total of 15 bin-lines). In the next section, this newly proposed acquisition geometry is evaluated using focal beam analysis. This newly proposed acquisition geometry is referred as ACQ2.

2.9 Focal beam analysis results and discussion

In this section, focal beams and focal functions for the proposed acquisition geometry of Schoonebeek oil field are computed and discussed. The focal beam computation (see 2.17 and equation 2.18) requires the following steps :

- Define a point diffractor at the target point.
- Compute $\vec{W}_k^\dagger(z_m, z_0)$ and $\vec{W}_k(z_0, z_m)$: Do the forward extrapolation of the wave field generated by a point source from this target point to the acquisition level.
- For the computation of the focal source beam, select the traces that correspond to the location of sources (**S**). For computation of the focal detector beam, select the traces that correspond to the location of detectors (**D**).
- Last step is an inverse extrapolation (**F**) of the selected traces of the wavefield from the acquisition surface to a subsurface area around the target point.

The above process flow for the focal beams computation is also explained in Figure 2.9. These focal beams are analyzed and used as a quality check for the current acquisition geometry. For the computation of the forward and inverse extrapolation operator, a recursive wave field extrapolation in (x, y, ω) domain, with a weighted least squares operator optimization method is used (Thorbecke and Wapenaar, 2003).

All focal beams and focal function are a function of four variables: the x, y, z -coordinates and time. For instance, if we decide to look at the beam at target level only, it is a three dimensional volume x, y - coordinates and time. To visualize this result in two dimensions, a slice from this three dimensional volume can be taken. In this thesis, the focal beams and resolution function will be shown at zero time (meaning the imaging principle has been applied). To evaluate the illumination and reception of the target location as a function of angle, a linear Radon transform of the beam is computed, after which the $\tau = 0$ s component is selected. To avoid a strange wavelet effects in the Radon domain, a Hilbert transformation is needed before $\tau = 0$ s is selected.

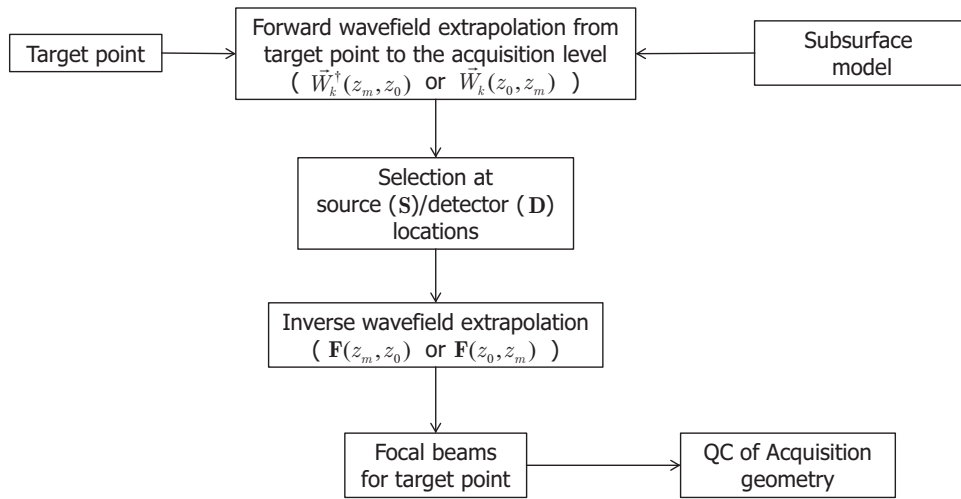


Figure 2.9: The process flow for the focal beams computation.

2.9.1 Schoonebeek Geometry and subsurface model

Figure 2.10 shows the newly proposed acquisition geometry (ACQ2). The acquisition geometry comprises the following features:

- 3 source lines with a spacing of 80 m and length of 576 m, in x -direction
- 5 detector lines parallel to source lines, with a spacing of 16 m and length of 1.1 km
- The source in-line spacing is 48 m and the detector in-line spacing is 16 m.

For the investigation of image quality, the target point is chosen at 530 m depth at a lateral location of $(x,y) = (800,800)$ m. A subsurface model is needed for the focal beam analysis. The Schoonebeek velocity model is a model with several layers that are more or less flat. The model is shown in Figure 2.11. The velocities in the layers vary from 1700 m/s to 3300 m/s. The frequency range for which the analysis is carried out is 2 Hz to 85 Hz. The extrapolation operators, with a length of 29 points, are optimized for a maximum propagation angle of 65°.

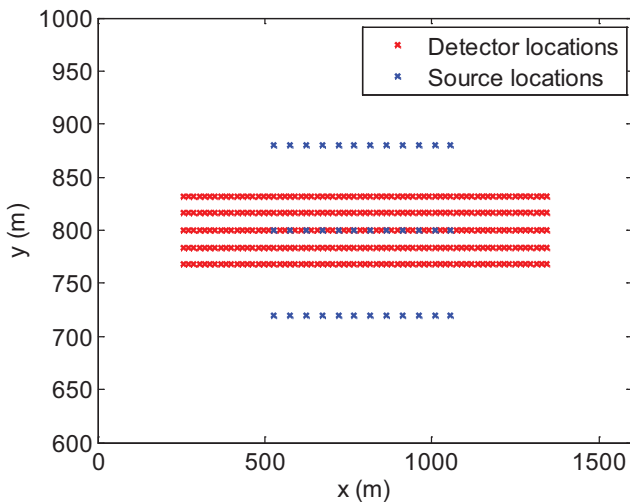


Figure 2.10: A simplified version of the proposed acquisition geometry (ACQ2) of Schoonebeek oilfield.

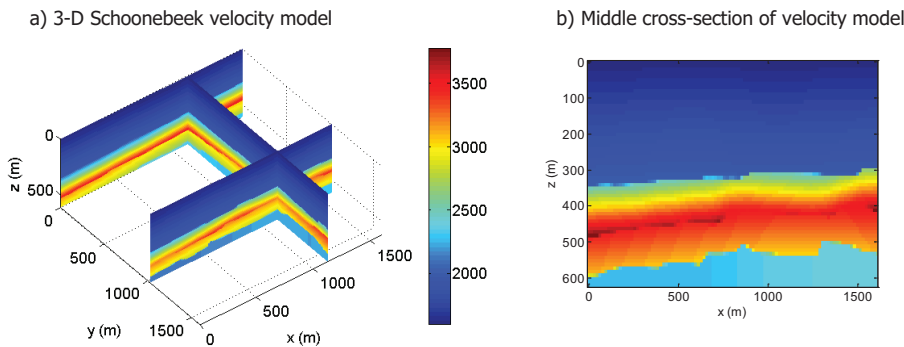


Figure 2.11: The Schoonebeek velocity model. a) shows the model in 3-D slices, b) shows a cross section of the velocity model.

2.9.2 Source and detector beam

The computed focal detector beam and the focal source beam for a single frequency of 40 Hz are shown in Figure 2.12. As mentioned in the theory section, ideally the focal detector beam when examined at the target depth

z_m would be unity at the target location and zero elsewhere, but in practice deviations occur because of the limitations of the acquisition geometry.

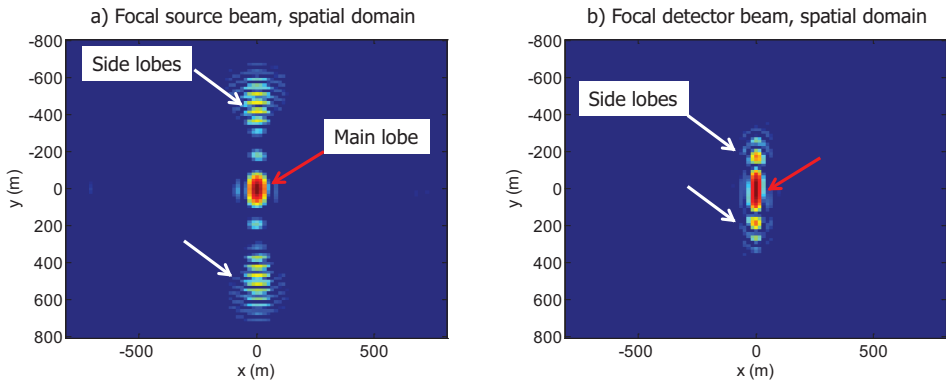


Figure 2.12: a) Focal source beam, b) Focal detector beam, both in the spatial domain for a single frequency of 40 Hz. White arrows indicate the position of side lobes whereas red arrows indicate the position of main lobe.

The large spacing between the lines results in spatial aliasing effects. Spatial aliasing causes the side lobes in the cross-line (y -)direction that are visible in Figure 2.12 (white arrows indicate the aliasing effects and side lobes). The different line spacings between source and detector lines results in different aliasing effects as can be noticed in Figure 2.12a and b. The resolution of the main lobe depends on the acquisition aperture. Larger acquisition apertures provide a better resolution and vice-versa. As we can see from the figures the resolution of the main lobe for both beams is good in the x -direction (red arrows indicate the main lobe). Due to a very limited aperture in the y -direction for both the source and the detector geometry, the resolution of the main lobe is not so good. The focal detector beam has a better resolution than the focal source beam along the x -direction as the aperture of the detector geometry is larger than that of the source geometry along the x -direction.

2.9.3 Frequency dependency

To see the frequency dependency of the focal beams, they are computed for a frequency of 40 and 60 Hz separately. Figure 2.13 shows the source beam for 40 Hz at the left hand side and the source beam for 60 Hz at the right hand side.

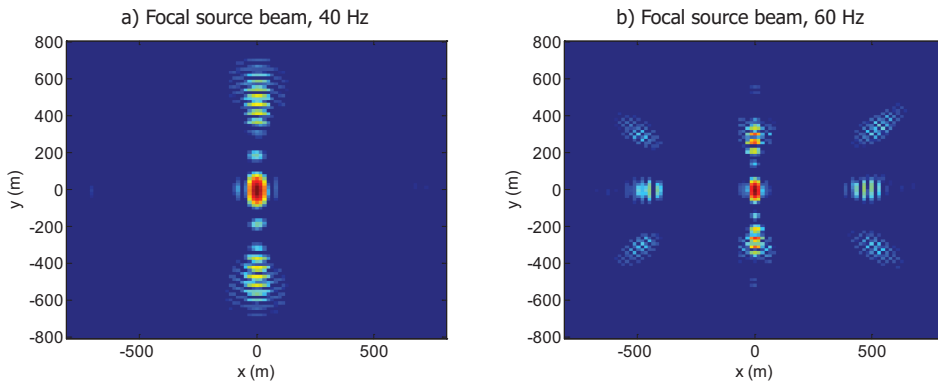


Figure 2.13: Comparison of a) focal source beam in the spatial domain for 40 Hz, b) same for 60 Hz. The side lobes of the 60 Hz beam are closer to the main lobe than those of 40 Hz beam.

Obviously the beam of 60 Hz has a more narrow main lobe than the beam of 40 Hz. The decrease of the width of the main lobe is proportional to the relative frequency increase. This means that if the frequency is increased by a factor of 1.5, the main lobe becomes smaller with that same factor. Also the side lobes are closer to the main lobe by the same stretch factor. In conclusion for a homogenous model it is possible to predict accurately the focal beams for a range of frequencies once it has been computed for only one frequency. However, for the complex model it is possible to interpolate the focal beams for a range of frequencies once they have been computed for a few frequencies. Based on this interesting observation, Wei et al. (2012) proposed a method for the efficient computation of 3-D multifrequency focal beams, in which only a few single-frequency focal beam computations are required, followed by a number of interpolations.

Since the position of side lobes changes as function of frequency, there will not be constructive interference of the side lobes. Hence the side-lobe level will decrease significantly for the wide band resolution function. The focal source beam and the focal detector beam for a wide range of frequencies (2-85 Hz) are shown in Figure 2.14, where we can see, the side-lobe level of the acquisition geometry is significantly reduced (especially in the case of the source beam) due to the destructive interference of side-lobes.

Figure 2.15 shows the focal beams in the Radon domain for the same target point located at $(x,y,z) = (800,800,530)$ m. The focal beams are shown here as a function of the lateral ray parameters p_x and p_y for a single frequency

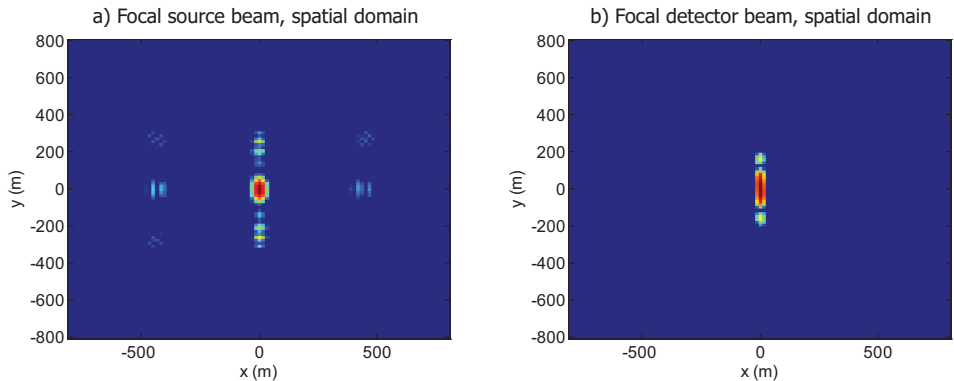


Figure 2.14: a) Focal source beam in the spatial domain for a large bandwidth, and b) focal detector beam in the spatial domain for a large bandwidth (2-85Hz). The side-lobe levels are significantly reduced in the case of a large bandwidth.

as well as for a wide frequency band. The maximum value of p_x and p_y is the P-wave slowness at the target point. This corresponds to a propagation angle of 90° for P-waves. In the Radon domain also, the focal source beam and detector beam show the influence of spatial aliasing in the y-direction as horizontal striping. Again the position of the horizontal striping changes as function of frequency, there will not be constructive interference of this striping. Hence, spatial aliasing effects are not so prominent for a wide frequency band (Figures 2.15b and d). Moreover, the focal beam shows increased amplitudes as a result of the edges of the acquisition geometry. This acquisition edge effect is responsible for the dark red areas in the focal beams.

2.9.4 Focal functions

Multiplication of the source and detector beam in the spatial domain yields the resolution function (see equation 2.20), which is the migration image of a point diffractor. Figure 2.16a shows the resolution function for a target point at 530 m depth for a wide frequency band (2-85 Hz). As can be seen from the figure, the main lobe in the in-line ($x-$) direction is smaller than in the cross-line ($y-$) direction. It means that due to the limited aperture in the y -direction, the geometry is unable to resolve the point diffractor properly. The multiplicative effects of the source and the detector beam also benefits in the reduction of side-lobe level.

The AVP-function is computed by multiplication of the source and detector

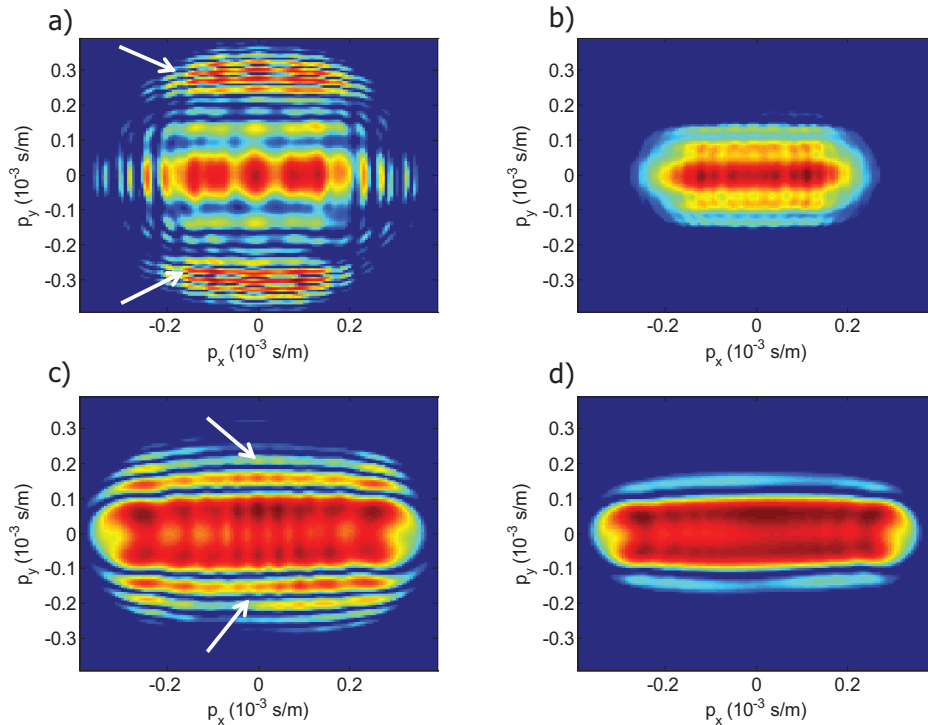


Figure 2.15: a) Focal source beam in the Radon domain for a single frequency of 40 Hz, b) Radon transformed focal source beam for a wide bandwidth (2-85Hz), c) Radon transformed focal detector beam for a single frequency of 40 Hz, and d) same for a wide bandwidth (2-85Hz). The aliasing effects as horizontal striping (shown by white arrows) are reduced significantly in the case of using the full frequency bandwidth.

beam in the Radon domain according to equation (2.23b). As discussed before, the computation of the AVP function, an angle-independent unit reflector is used instead of the target reflectivity. In this way, the influence of the source geometry, detector geometry, propagation and migration are considered separately from the reflectivity of the target. Any deviations from a uniform amplitude distribution implies an imprint on the angle-dependent reflection coefficient of the target reflector.

Due to the multiplication of the source and detector beams, the AVP function is very sensitive to a specific source and detector geometry. In this situation the source and detector geometry do not complement each other. Of all detectors, only few are actually detecting the reflection of the subsurface grid point. The AVP function for the Schoonebeek acquisition geometry is

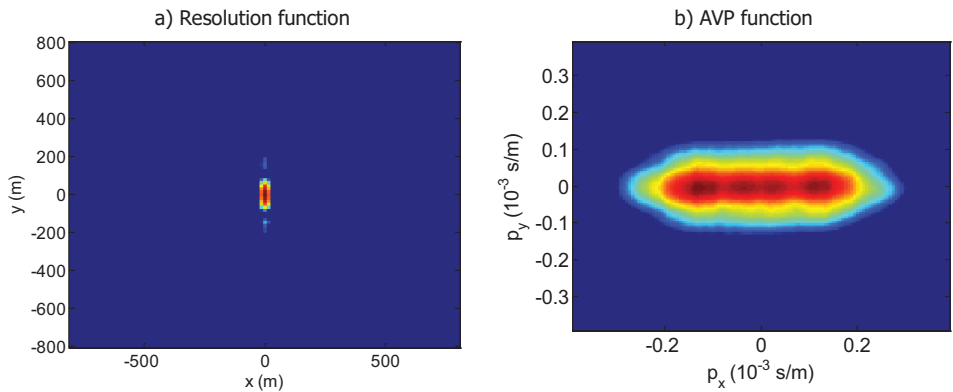


Figure 2.16: a) Resolution function for a target point at 530 m depth (large bandwidth). The in-line resolution is better than the cross-line resolution, and b) AVP function for the same target point (large bandwidth).

shown in Figure 2.16b for the same target point at 530 m depth. As can be seen from the figure more angle information can be obtained in the x -direction but limited angle information can be obtained in the y -direction. It is obvious because we have a limited aperture in the y -direction for both the source and detector geometry.

2.9.5 Suggestions for further improvement

The results from the focal beam analysis clearly show the limitation of the angle aperture in the cross-line (y -)direction for this ACQ2 geometry. Also, due to its limited aperture in the y -direction, this geometry is unable to resolve point diffractors properly. Hence, increase of the aperture in the y -direction for both the source and the detector geometry will improve the result of the focal functions. The larger source-line spacing causes the side lobes in the focal source beam. Therefore, a smaller source-line spacing will reduce the side lobes of the focal source beam and it will improve the amplitude accuracy. Depending upon the design requirements about angle-dependent information at the target, a new acquisition geometry is suggested, referred to ACQ3 (shown in Figure 2.17).

There are more source and detector lines added to improve the angle information along the cross-line direction. Also, the source line interval is reduced from 80 m to 48 m. The ACQ3 geometry is designed such that it improves

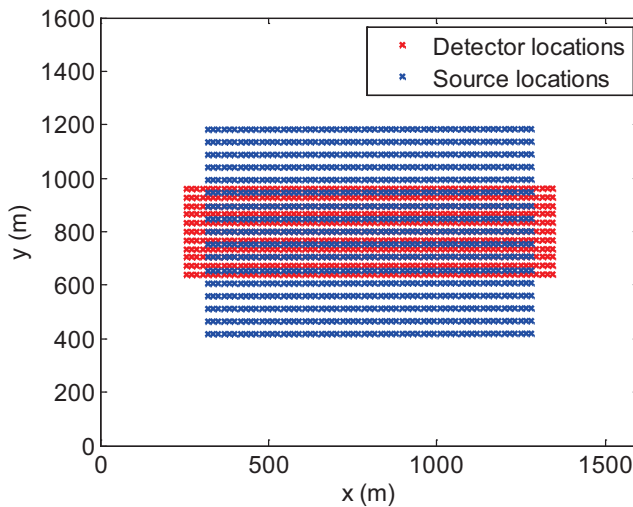


Figure 2.17: A new version of suggested acquisition geometry for the Schoonebeek oilfield to improve the image quality. This acquisition geometry is referred as ACQ3 in this chapter.

the focal beams in the spatial as well as in the Radon domain. The source beam in the spatial as well as in the Radon domain for the original and the new geometry are shown in Figure 2.18. As can be seen from the figure, the side lobes are moved farther away from the main-lobe as well as a much better illumination is achieved for the new geometry. The width of the main lobe also becomes narrower than the ACQ2 geometry because of the increased aperture.

The resolution functions for the ACQ2 and ACQ3 geometry are shown in Figure 2.19. Clearly the side lobes are removed completely, also the main lobe becomes narrower and sharper in the cross-line direction.

The AVP functions for the ACQ2 and the ACQ3 geometry are shown in Figure 2.20. The bandwidth of the AVP-function is increased by the extension of source and detector lines. This is favorable for the estimation of velocities in the cross-line direction.

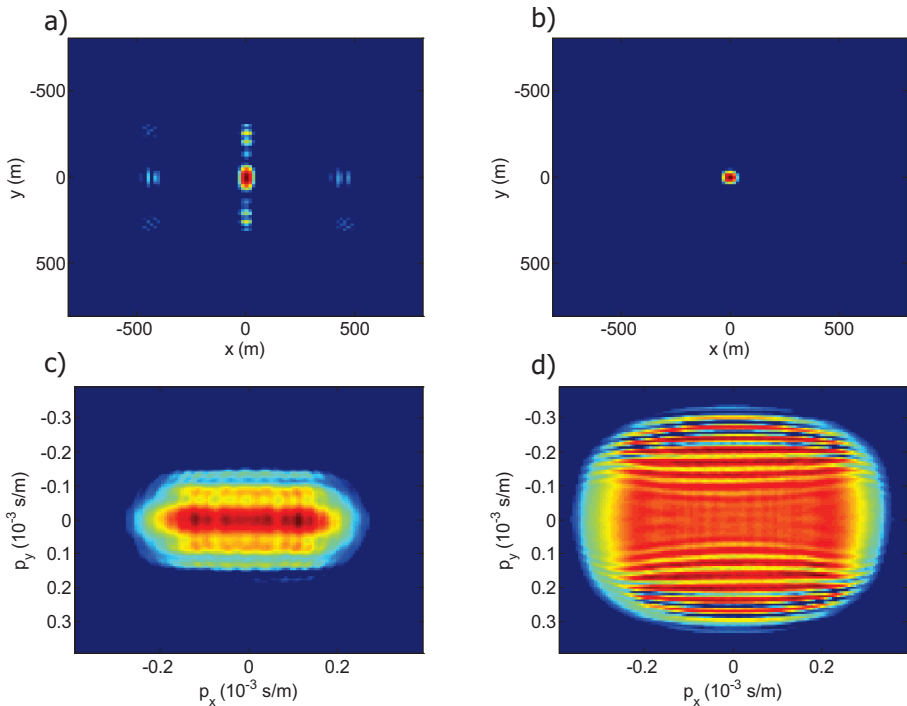


Figure 2.18: a) The focal source beam in the spatial domain for the ACQ2 geometry, b) same for the ACQ3 geometry, c) The focal source beam in the Radon domain for the ACQ2 geometry, and d) same for the ACQ3 geometry.

2.10 Conclusion from this chapter

This chapter establishes a theoretical framework for integrating the acquisition geometry with the subsurface model, being the second phase of the survey design. Focal beam analysis is a method for assessment of subsurface image quality as affected by the seismic acquisition geometry. It has a direct link to pre-stack depth migration. This important feature ensures that the analysis result is directly related to the seismic image quality as it would be obtained by pre-stack depth migration. An acquisition geometry can be assessed using the focal beams and focal functions, where:

- The focal detector and focal source beams are used to separately assess the geometry effects of detectors and sources respectively.
- The focal resolution function is used to measure the spatial resolution at the target and to reveal whether spatial aliasing occurs.

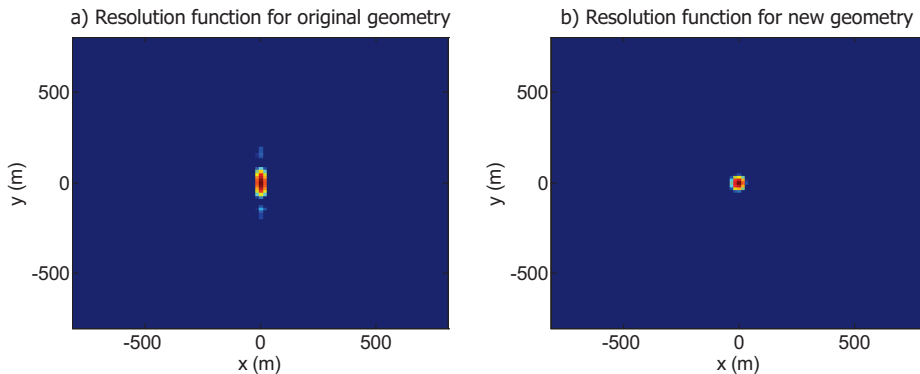


Figure 2.19: a) Resolution function for the ACQ2 geometry, b) same for the ACQ3 geometry. The main-lobe is sharper and narrower for the new design.

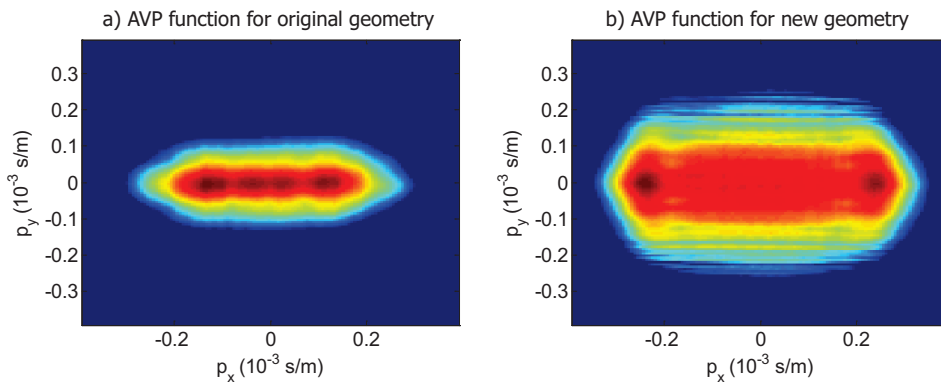


Figure 2.20: a) AVP function for the original geometry, b) same for the new geometry. The new design has much larger bandwidth in the cross-line direction.

- The focal AVP function is used to show how the angle-dependent reflectivity is sampled at the target by a particular acquisition geometry.

The concept of focal beams integrates two different aspects of the seismic discipline, namely acquisition design and imaging. However, the imaging till now is related to the primaries-only case. In the next chapters, we extend this concept to multiples as well, leading to the relation between acquisition design and full-wavefield migration.

Chapter 3

Including secondary illumination in seismic acquisition design ¹

3.1 Introduction

A subsurface image obtained from seismic data is influenced by the acquisition geometry, as it contains an acquisition footprint which can obscure the true reflection response of the subsurface. Hence, the acquisition geometry should be designed in such a way that it allows high-quality images and fulfills the criteria for reservoir characterization. A comprehensive and quantitative assessment of 3-D acquisition geometries, taking into account the effects of the overburden, is provided by the so-called focal beam analysis method, discussed in detail in the previous chapter. Both the resolution and the amplitude accuracy can be estimated.

The separate analysis of the source and receiver geometry in the focal beam method provides the opportunity to obtain angle dependent information for illumination (source side) as well as sensing (detector side). In the case of primary illumination, the illumination part concerns the primary source. However, the subsurface is not only illuminated by primary source wavefields (generating the primaries), but also by secondary source wavefields (generating the surface-related multiples). The fact that secondary source wavefields can be used for imaging has been recognized in global seismology,

¹This chapter is a part of an extended abstract presented at the 83rd Annual International Meeting, SEG (Kumar and Blacquière, 2013) abstract presented at the 83rd Annual International Meeting, SEG (Kumar and Blacquière, 2013). Several changes were introduced to make the text consistent with the other chapters of this thesis.

e.g., Bostock et al. (2001) and Rondenay et al. (2005) discussed the improved resolution of regional scale images of the crust and upper mantle of the Earth by including surface-related multiples from teleseismic earthquakes in their imaging method. The use of multiples for velocity estimation and imaging in exploration seismology has been discussed in the past by Berkhou and Verschuur (1994), and more recently by Schuster (2005), Jiang et al. (2005) and Verschuur and Berkhou (2011).

Using surface multiples in imaging and characterization is an emerging methodology. Therefore, it is important to analyze their significance for acquisition geometry design as well. In this chapter, we propose to include information from surface-related multiples in the focal beam analysis method and formulate a concept of a secondary source beam similar to a primary source beam. This is important because multiples may illuminate the subsurface from more and other angles than primaries, leading to a higher resolution and a better signal to noise ratio (Berkhou et al., 2012a). The secondary source beam will provide us the information of those extra angles from which a subsurface target point will get illuminated. Also, the effect of inclusion of surface-related multiples on the resolution function and AVP function will be studied. This will give us an extra parameter to include at the time of 2-D and 3-D acquisition design. The secondary source beam and its effects are illustrated with the help of 3-D examples.

3.2 Double illumination

In the previous chapter, the representation of the data matrix was discussed in detail. However, that representation contains only primary reflections. Surface related multiples can be included in the model by introducing a feedback loop as is shown in Figure 3.1. Physically this means that apart from the primary source there are secondary sources at the surface which generate an additional downgoing source wavefield. The monochromatic expression of surface seismic data (\mathbf{P}) - including surface-related multiples, is given by the following feedback model (Berkhou, 1982):

$$\begin{aligned}
 \mathbf{P} &= \mathbf{D}\mathbf{P}^-, \\
 &= \mathbf{D}\mathbf{W}^-\mathbf{R}^\cup\mathbf{W}^+(\mathbf{S} + \mathbf{R}^\cap\mathbf{P}^-), \\
 &= \mathbf{D}\mathbf{W}^-\mathbf{R}^\cup\mathbf{W}^+\mathbf{S} + \mathbf{D}\mathbf{W}^-\mathbf{R}^\cup\mathbf{W}^+\mathbf{R}^\cap\mathbf{P}^-, \\
 &= \mathbf{P}_0 + \mathbf{M}_0.
 \end{aligned} \tag{3.1}$$

For simplification, we have dropped the terms related to depth levels between the brackets from all the matrices. Here \mathbf{R}^\cap represents the surface reflectivity and \mathbf{P}^- is the total upward traveling wavefield. The matrices \mathbf{P}_0 and \mathbf{M}_0 are primaries-only reflections and multiples-only reflections data, respectively. The total upward traveling wavefields are measured discretely at the detector locations and indicated as \mathbf{P} . It is important to realize that in a practical implementation, the secondary downgoing wavefield is known only at the position of detector locations ($\mathbf{R}^\cap \mathbf{P}^- \Rightarrow \mathbf{R}^\cap \mathbf{D} \mathbf{P}^- = \mathbf{R}^\cap \mathbf{P}$). This means that the benefits to be obtained from the secondary illumination depend on the detector distribution of the acquisition geometry (Berkhout et al., 2012b).

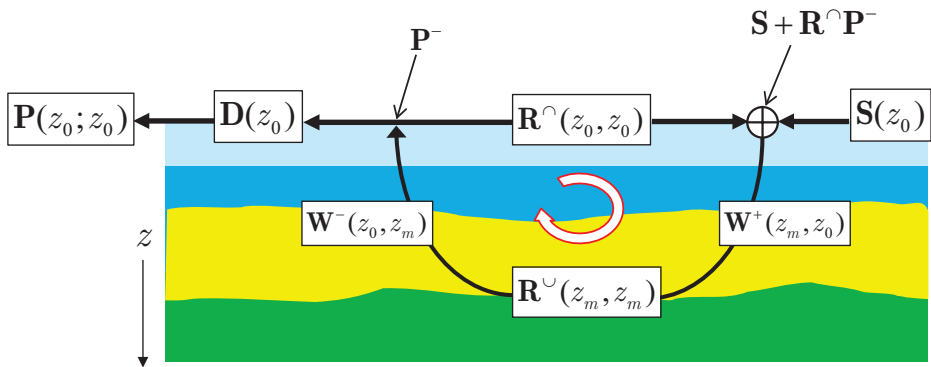


Figure 3.1: Model for seismic data in the case of a reflective surface (feedback model), showing the double illumination property. Note that \mathbf{S} is emitting energy at the source positions (primary illumination) and the energy emitted by the secondary sources, $\mathbf{R}^\cap \mathbf{P}^-$, is known at the detector positions (secondary illumination).

Equation (3.1) shows that the subsurface is illuminated by primary source wavefields (generating the primaries) as well as by secondary source wavefields (generating the surface-related multiples). We call this phenomenon double illumination. We now investigate the illumination of a single subsurface gridpoint. We start with the conventional situation, i.e., without surface scattering. Next, the surface scattering will be included. Without surface multiples, the incident wavefield in the subsurface gridpoint k at $(x, y)_k$, generated by a single traditional source array j , can be represented by the complex-valued scalar quantity:

$$P_{kj}^+(z_m; z_0) = \vec{W}_k^\dagger(z_m, z_0) \vec{S}_j(z_0). \quad (3.2)$$

The row vector \vec{W}_k^\dagger equals the k^{th} row of downward propagation matrix \mathbf{W}^+ .

It describes downward extrapolation from all locations at surface level z_0 to gridpoint k at depth level z_m . In seismic shot record migration, the source-related step aims at transforming $P_{kj}^+ = \vec{W}_k^\dagger \vec{S}_j$ into unity for all gridpoints at all depth levels z_m ($m = 1, 2, \dots$). In other words, this step aims at a deconvolution process that transforms the incident source wavefield at gridpoint k into a band-limited spike. The illumination strength for the involved frequencies must be sufficient to make this step successful. A proper seismic acquisition design should guarantee this requirement.

Now, the conventional illumination of the subsurface will be improved by including the illumination properties of the surface multiples as well (Figure 3.2). We call this double illumination:

$$\begin{aligned} P_{kj}^+(z_m; z_0) &= \vec{W}_k^\dagger(z_m, z_0) \left[\vec{S}_j(z_0) + \mathbf{R}^\cap(z_0, z_0) \vec{P}_j^-(z_m; z_0) \right] \\ &= \vec{W}_k^\dagger(z_m, z_0) \vec{Q}_j(z_0). \end{aligned} \quad (3.3)$$

Equation (3.3) is the connection between a source array (j) at the reflective surface z_0 and the corresponding double illumination at a specific subsurface gridpoint (k) in the subsurface z_m , taking the surface multiples into account.

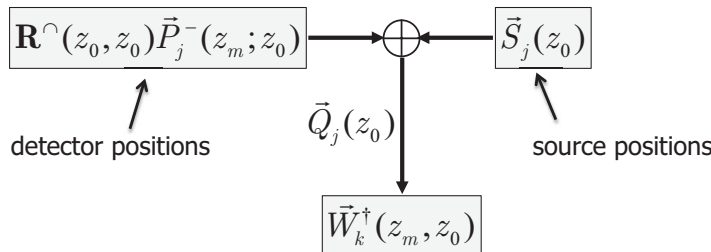


Figure 3.2: The incident wavefield at subsurface gridpoint k due to primary and secondary sources at the surface (double illumination).

3.3 Including the surface-related multiples in focal beam formulation

The complexity by the surface-multiples in the feedback loop is kept at the source side, providing an additional downgoing source wavefield. It means nothing has to be changed in the focal detector beam computation. However, the focal source beam should be computed for primary sources (\mathbf{S}) as well

as secondary sources ($\mathbf{R}^\cap \mathbf{P}^-$), separately. As explained earlier in equation (2.18), the expression of the focal source beam for the primary data (\mathbf{P}_0) contains one forward propagation term (\mathbf{W}) and a focusing term (\mathbf{F}). In terms of the source beam matrix, it can be written as:

$$\mathbf{S}^p = \mathbf{W}^+ \mathbf{S} \mathbf{F}^p. \quad (3.4)$$

Here superscript p represents the source beam for the primaries-only source wavefield (\mathbf{S}). In the ideal case, at target depth a focal beam will show one narrow peak at the lateral location of the target point. This means equation (3.4) is an identity matrix in the ideal case:

$$\begin{aligned} \mathbf{W}^+ \mathbf{S} \mathbf{F}^p &= \mathbf{I}, \\ \mathbf{F}^p &\approx \mathbf{I}(\mathbf{S})^{-1} (\mathbf{W}^+)^{-1} \approx (\mathbf{S})^{-1} (\mathbf{W}^-)^*. \end{aligned} \quad (3.5)$$

The matrix \mathbf{F}^p represents the primary focusing operator, which aims to remove the propagation effects from the primaries-only data. In a similar way, a secondary source beam for the multiples data (\mathbf{M}_0) can be formulated as:

$$\mathbf{S}^m = \mathbf{W}^+ \mathbf{R}^\cap \mathbf{P} \mathbf{F}^m. \quad (3.6)$$

Here superscript m represents the source beam for the secondary source wavefield ($\mathbf{R}^\cap \mathbf{P}$). Similarly \mathbf{F}^m can be written as:

$$\mathbf{F}^m \approx (\mathbf{R}^\cap \mathbf{P})^{-1} (\mathbf{W}^-)^* = \mathbf{P}^{-1} (\mathbf{R}^\cap)^{-1} (\mathbf{W}^-)^*. \quad (3.7)$$

The inversion of a data matrix in a least-squares sense can be expressed as:

$$\mathbf{P}^{-1} \approx \mathbf{P}^H [\mathbf{P} \mathbf{P}^H + \varepsilon^2 \mathbf{I}]^{-1}. \quad (3.8)$$

In equation (3.8) superscript H denotes the Hermitian operator and the extra term ε^2 is a small positive constant that is used for stabilization purposes. Of course, equation 3.8 can be refined further by using a more sophisticated inversion scheme.

Using $\mathbf{R}^\cap = -\mathbf{I}$, the secondary source beam expression can be further simplified to:

$$\mathbf{S}^m \approx \mathbf{W}^+ [\mathbf{P} \mathbf{P}^H [\mathbf{P} \mathbf{P}^H + \varepsilon^2 \mathbf{I}]^{-1}] (\mathbf{W}^-)^*. \quad (3.9)$$

The total focal source beam (primary plus secondary) can be written as:

$$\mathbf{S}^t = \mathbf{S}^p + \mathbf{S}^m. \quad (3.10)$$

where \mathbf{S}^p and \mathbf{S}^m are given by equations (3.4) and (3.6) respectively. Here superscript t represents the source beam for the total incident wavefield $(\mathbf{S}^+ + \mathbf{R}^\top \mathbf{P})$. Note that to compute the secondary focusing operator, an inverse of data matrix (\mathbf{P}) should be taken. Inversion of the full data matrix in practice may produce cross talk noise, especially in the case of a complex model. In order to overcome this issue, we propose to select only strong surface-related multiples (e.g., water bottom multiples) and perform the inversion event by event via the conjugate transpose of data matrix. In this way, the conjugate transpose of a matrix is a good approximation of an inverse of a matrix. In chapter 4, we introduce a method to deal with this situation properly.

According to equation (3.9), for the computation of the secondary source beam, an auto-correlation of data matrix $(\mathbf{P}\mathbf{P}^H)$ is applied to the forward extrapolated wavefield (\mathbf{W}^+) sampled at the detector location. Later, this re-sampled wavefield is inversely extrapolated $(\{\mathbf{W}^-\}^*)$ from the acquisition surface to a subsurface area around the target point.

3.4 Examples

To illustrate the concept of the primary and the secondary source beam, the following 3-D acquisition geometry is considered. It comprises of a densely sampled detector spread with a sampling interval of 50 m in both the x and y -direction and only one source line of 3000 m length with a sampling interval of 100 m along the x -direction located at $y = 3500$ m as shown in Figure 3.3.

Focal beams and focal functions are computed for this acquisition geometry for a target point located at $(x, y, z = 2000, 2000, 1000)$ m. For the computation of the forward and inverse extrapolation operators, a recursive wave field extrapolation in the (x, y, ω) domain with a weighted least-squares operator optimization method is used (Thorbecke et al., 2004). The velocity in the subsurface is assumed constant at 2500 m/s. The frequency range for which the analysis is carried out is 5-30 Hz.

Figure 3.4 shows the results of focal beams and focal functions for the considered 3-D geometry in the case of primary reflections only. Note that the detector beam shows that all angles are sensed and is ideal in the spatial as well as the Radon domain (Figure 3.4a and 3.4d), as expected from the densely sampled detector spread. On the other hand, the source beam suffers from poor illumination and does show only one direction of illumination

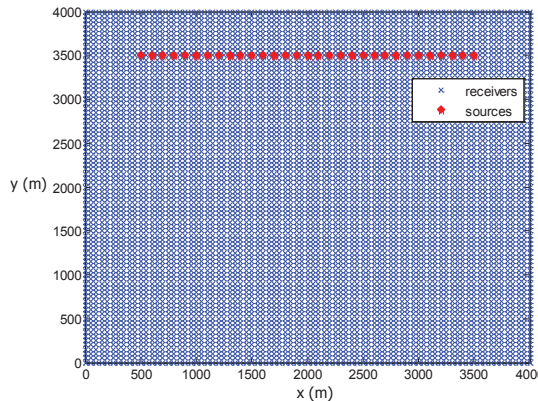


Figure 3.3: The 3-D acquisition geometry template for the focal beam analysis.

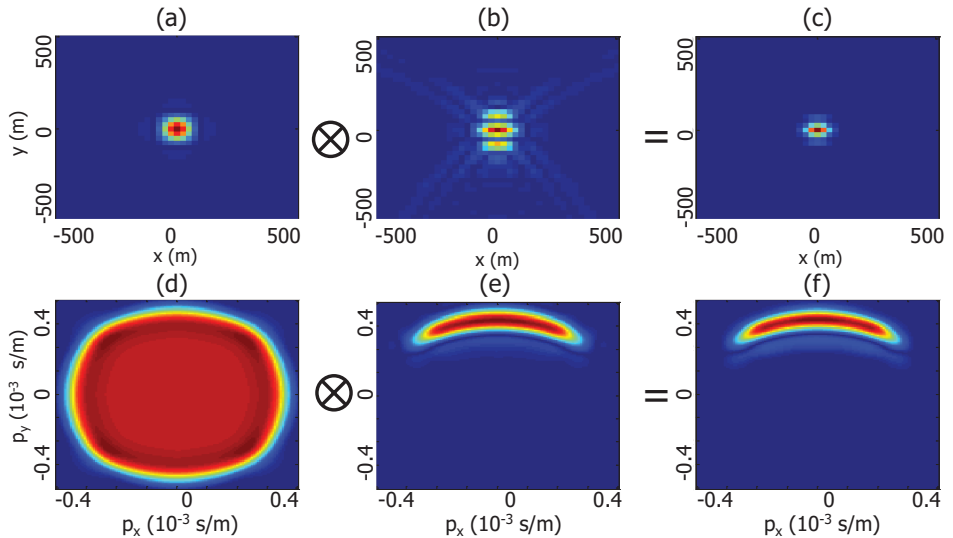


Figure 3.4: a) Focal detector beam in the spatial domain, b) focal source beam in the spatial domain, c) the resolution function for a given target point, d) focal detector beam in the Radon domain showing sensing angles, e) focal source beam in the Radon domain showing illumination angles, and f) the AVP function showing illumination-and-sensing angles for the primaries-only wavefield.

in the Radon domain (Figure 3.4e). The focal functions are obtained by multiplication of the focal beams in the spatial and the Radon domain respectively. Because of multiplicative effects, this acquisition geometry is able

to resolve the point diffractor properly but the AVP function shows a very limited range of angles in the ray-parameter domain (Figure 3.4c and 3.4f). It means that angle-dependent reflection information in the y -direction can not be retrieved properly from this acquisition geometry.

So far, we have seen the results of the focal beams and focal functions due to the primaries-only wavefield. Next, the computations are carried out for surface related multiples as a secondary source wavefield. The secondary source beam is computed for the same target point using modelled surface multiples. In case of a homogeneous medium the target point is illuminated by an additional angle for every additional order of surface multiple. The new angles of illumination are complementary to the angles of illumination due to the primaries-only wavefield.

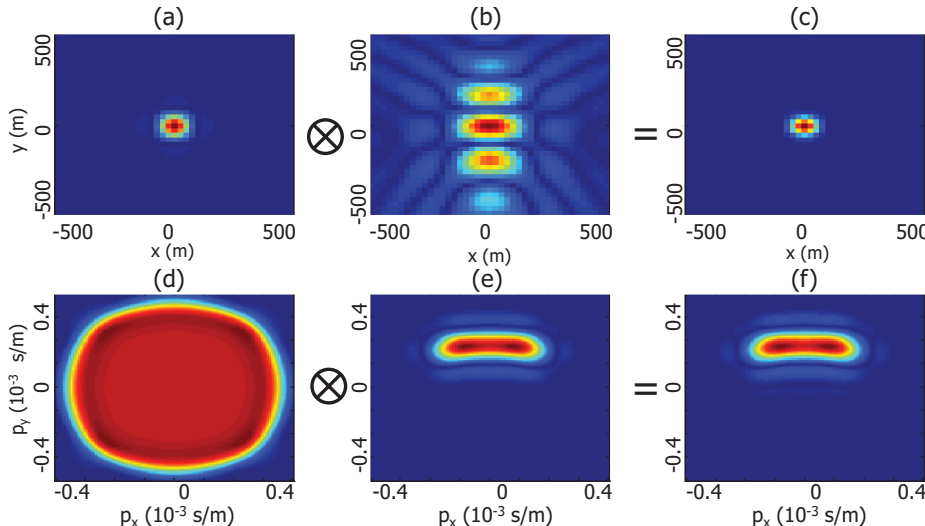


Figure 3.5: Same as Figure 3.4 but for the 1st order multiple.

Figures 3.5, 3.6 and 3.7 show the results of the focal beams and functions for each order of multiples separately. Note that the detector beam is unchanged as it should be, and the secondary source beam in the Radon domain provides different illumination angles than the primary source beam. For this simple, homogeneous subsurface, as we increase the order of multiples, the apertures of the secondary sources get reduced which affects the focusing of secondary source beams in the spatial domain as can be seen in Figure 3.5b, 3.6b and 3.7b. But, at the end, we add all these secondary beams together with the

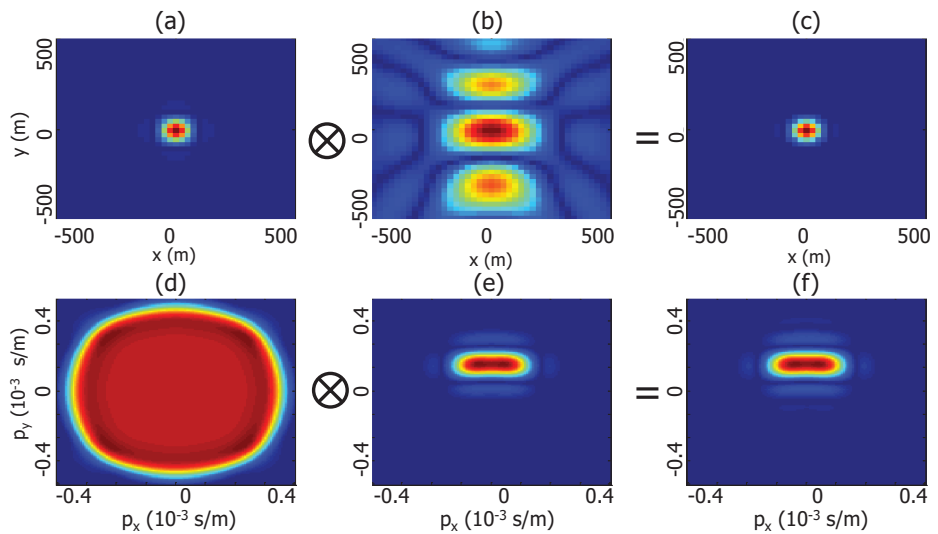


Figure 3.6: Same as Figure 3.4 but for the 2nd order multiple.

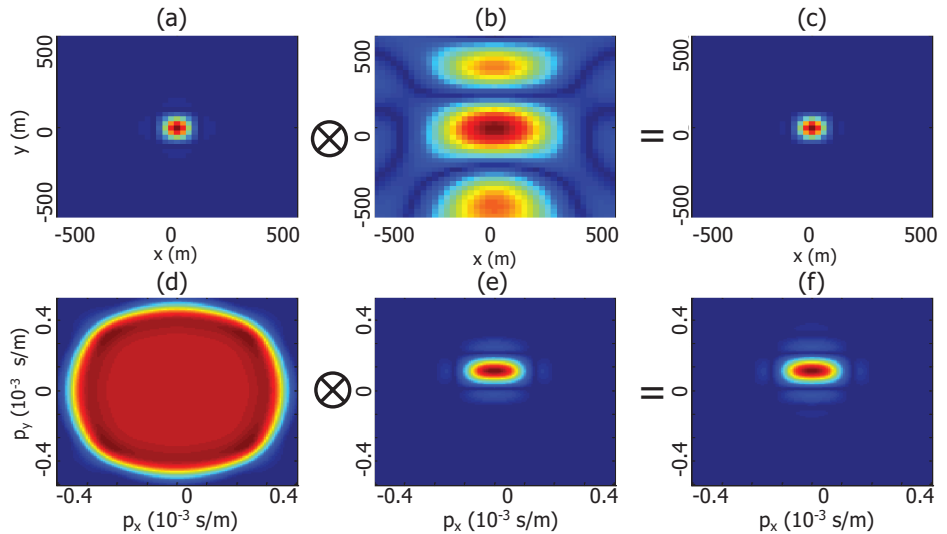


Figure 3.7: Same as Figure 3.4 but for the 3rd order multiple.

primary beam. As a consequence, the resolution gets improved because of the extra angle information as shown in Figure 3.8. As a final remark, we conclude that the primary and secondary source beam together will lead to a better focal source beam and AVP function.

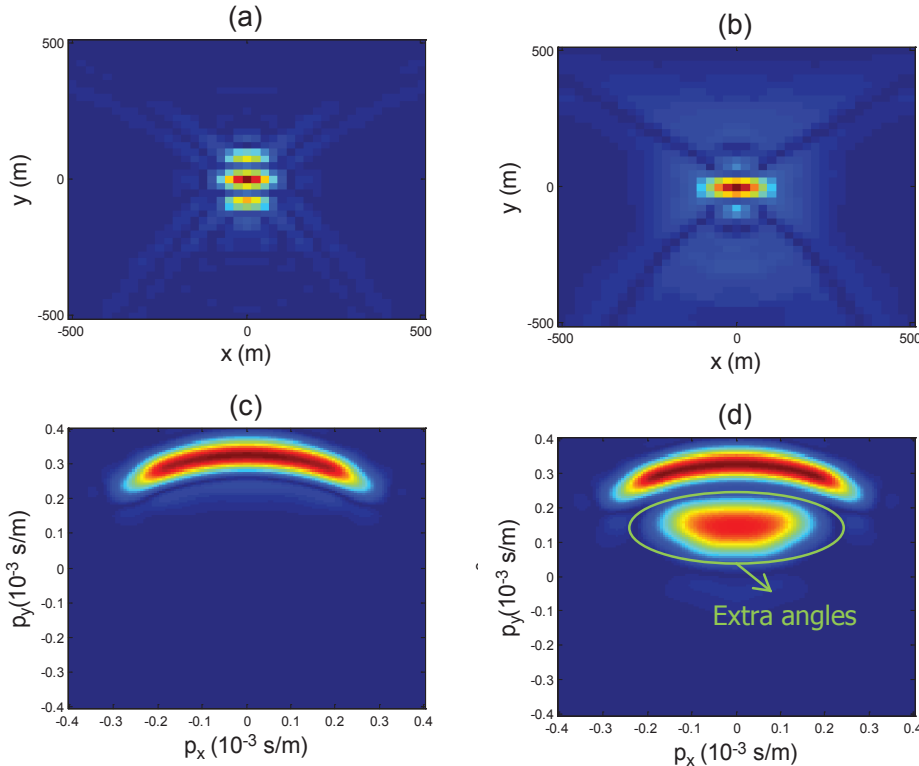


Figure 3.8: a) Focal source beam (spatial domain) for the primaries-only wavefield, b) focal source beam (spatial domain) for the primaries-plus-multiples wavefield, c) focal source beam (Radon domain) for the primaries-only wavefield, and d) focal source beam (Radon domain) for the primaries-plus-multiples wavefield.

In the previous example, the detector spread was densely sampled within the aperture range. As we mentioned, the benefits to be obtained from the secondary illumination depend on the detector distribution of the acquisition geometry. Next, we show the results of secondary illumination for the case that some of the detector lines are removed from the above acquisition geometry. In this example, detectors are now sampled sparsely along the x -direction with the sampling interval of 400 m (shown in Figure 3.9).

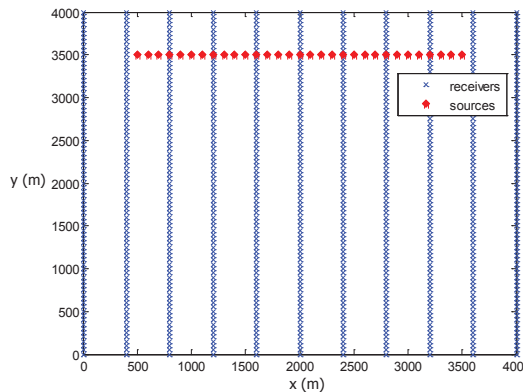


Figure 3.9: A second example of a 3-D acquisition geometry.

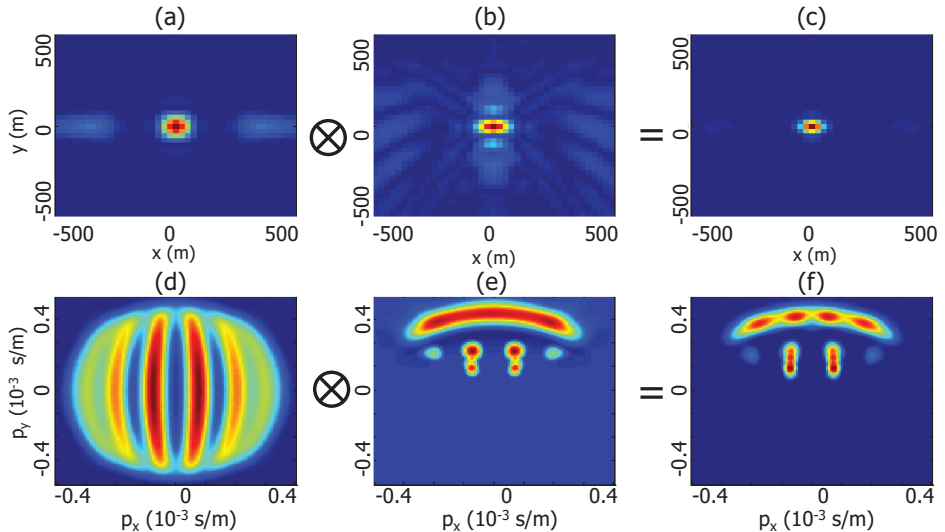


Figure 3.10: Same as Figure 3.7 but the effect of removing some of the detector lines on the focal beams and focal functions for the for the primaries as well as including three order multiples wavefield.

Focal beams and functions are computed for the same target point as in the previous example for the primaries as well as including three orders of multiples. The results are shown in Figure 3.10. Here as expected, the detector beam in the spatial domain shows some side lobes along the x -direction due to the sparse sampling. The larger line spacing along the x -

direction is directly apparent in the Radon domain. The individual detector lines can be easily identified.

As the detector geometry is not perfect, its effects are clearly visible on the secondary source beam both in the spatial and in the Radon domain (Figures 3.10b and 3.10e). The poor focusing in the spatial domain and less extra angle information in the Radon domain compared to Figure 3.8d can be seen clearly. This explains the importance of a proper detector sampling for the use of secondary illumination.

3.5 Conclusion from this chapter

The focal beam analysis method can be extended to surface-related multiples, leading to the concept of a secondary source beam. Surface-related multiples provide an additional downgoing source wavefield that illuminates the target point at other angles than primaries. Therefore, more angle-dependent information can be retrieved with the help of these secondary sources. It should be noted that the secondary source wavefield ($\mathbf{R} \cap \mathbf{P}$) is measured at the detector locations. Therefore, the benefits to be obtained from the secondary illumination depend on the detector distribution of the acquisition geometry. So the concept of secondary illumination favors an improved detector sampling, rather than the conventional rule of symmetric sampling.

The downside of this method to compute secondary source beams is that it is computationally expensive and time consuming because all the shot-records (\mathbf{P}) have to be known in advance for the auto-correlation step ($\mathbf{P}\mathbf{P}^H$). However, in the next chapter, we solve this issue. There, we present an efficient method in which there is no need to compute complete data sets. Only multiples corresponding to a particular target point are modelled using a full-wavefield modeling scheme. In this way, we include the illumination by internal multiples as well, leading to the concept of triple-illumination. This provides another 'free-of-charge' enhancement of the incident wavefield.

Chapter 4

Extending illumination using all multiples: *theory*¹

4.1 Introduction

Recent advances in survey design have led to conventional common-midpoint-based analysis being replaced by subsurface-based seismic acquisition analysis, with the emphasis on advanced techniques of illumination analysis. Amongst them is the so-called focal beam method, a wave-equation-based seismic illumination analysis method. The objective of the focal beam method is to provide a quantitative insight into the combined influence of acquisition geometry, overburden structure, and migration operators on the resolution and angle dependent reflectivity of the image. The method distinguishes between the illumination and sensing capability of a particular acquisition geometry by computing the focal source beam and the focal detector beam, respectively. Sensing is related to the detection properties of a detector configuration, while illumination is related to the emission properties of a source configuration. The focal source beam analyses the incident wavefield at a specific subsurface grid-point related to the available sources, while the focal detector beam analyses the sensing wavefield at the same subsurface grid-point, related to the available detectors.

So far, only the primary reflection signals (primaries) were addressed in any previous seismic acquisition analysis method leaving aside the multiply-

¹This chapter is accepted to *Geophysical Prospecting* (Kumar et al., 2014b). Several changes were introduced to make the text consistent with the other chapters of this thesis.

reflected signals (multiples). Therefore, the migration result simulated for a specific grid point was similar to Kirchhoff migration. However, the subsurface is not only illuminated by the primary source wavefields (generating the primaries), but also by the secondary source wavefields at the surface (generating the surface-related multiples) and in the subsurface (generating the internal multiples). These waves may illuminate structures that can not be easily illuminated by primaries, in which case they allow us to image portions of the subsurface not illuminated by singly-scattered waves. Therefore, multiples should not be treated as noise anymore. However, to make use of multiples in imaging, a better and more robust migration algorithm is needed. Over the last few years, the use of multiple reflections in seismic imaging has been discussed by many authors (Jiang et al., 2005; Whitmore et al., 2010; Berkhout and Verschuur, 2011; Verschuur and Berkhout, 2011; Lu et al., 2011; Soni et al., 2012; Davydenko and Verschuur, 2013; Fleury, 2013; Slob et al., 2014).

In the previous chapter, we discussed the inclusion of surface-related multiples in the focal beam method. Also, the case of illumination by surface-related multiples for blended source arrays has been discussed by Berkhout et al. (2012b). In this chapter, we include illumination by internal multiples in our analysis, leading to the triple illumination (direct, surface-related multiples and internal multiples). We reformulate the grid-point response by incorporating all the source-side multiples, which differs from the approach of chapter 3. Therefore, the incident wavefield at a specific grid-point becomes more complex. Furthermore, we discuss the extended focal beam theory where we propose a least-squares minimization process to compute the focal source beam using all the multiples. We distinguish between illumination from above and illumination from below and their impact on the estimation of angle-dependent reflectivity. We will illustrate our theory with both 2-D and 3-D numerical examples.

4.2 Extension of the focal beam method

The theoretical foundation of the so-called focal beam theory has been discussed extensively in chapter 2. In this section, we will extend this concept to include all multiples. We first explain the theoretical expression of the grid-point response for including multiples. Then the focal source beam for multiples will be formulated.

4.2.1 Grid-point response: including multiples

Let us recall the expression of the grid-point response for the primary reflections from chapter 2, given by equation (2.9):

$$\delta_k \vec{P}_j(z_0; z_0) = \mathbf{D}^{[j]}(z_0) \mathbf{W}^-(z_0, z_m) \delta_k \mathbf{R}^{\cup}(z_m, z_m) \mathbf{W}^+(z_m, z_0) \vec{S}_j(z_0). \quad (4.1)$$

In this expression, the propagation matrices \mathbf{W}^+ and \mathbf{W}^- are one-way scattering free propagators. There are no transmission effects included in these propagators. The term $\mathbf{W}^+(z_m, z_0) \vec{S}_j(z_0)$ on the right hand side of the grid-point reflectivity matrix $\delta_k \mathbf{R}^{\cup}(z_m, z_m)$ of equation (4.1) represents the source side of the experiments. It represents the wavefield due to source j incident at depth level z_m from above, and is, therefore, referred to as the illuminating wavefield from above: $\vec{P}_j^+(z_m; z_0) = \mathbf{W}^+(z_m, z_0) \vec{S}_j(z_0)$. If we include all multiples in the model, then the monochromatic grid-point response for the full wavefield becomes the following equation:

$$\delta_k \vec{P}_j(z_0; z_0) = \mathbf{D}^{[j]}(z_0) \mathbf{W}^-(z_0, z_m) \delta_k \mathbf{R}^{\cup}(z_m, z_m) \mathbf{G}^+(z_m, z_0) \vec{S}_j(z_0). \quad (4.2)$$

The only change here with respect to equation (2.9) is that one-way propagator $\mathbf{W}^+(z_m, z_0)$ is replaced by the full-wavefield propagator $\mathbf{G}^+(z_m, z_0)$, which includes the effects of all multiples. It means that all the complex wave propagation paths by the multiples are kept on the source side, leading to a complex full illuminating wavefield from above, i.e., $\vec{P}_j^+(z_m; z_0) = \mathbf{G}^+(z_m, z_0) \vec{S}_j(z_0)$. With the full illuminating wavefield here, we mean the combination of the illumination by the direct wavefields, surface-related multiples and internal multiples. Note that, the operator $\mathbf{G}^+(z_m, z_0)$ includes all multiples which incident at the grid-point from above only. Later, we will discuss about multiples which incident at the grid-point from below as well. Figure 4.1 illustrates the primaries-only grid-point response and full wavefield grid-point response respectively.

If we again assume a stationary detector geometry, then, for all J sources at the surface, the full grid-point response matrix can be expressed as:

$$\delta_k \mathbf{P}(z_0; z_0) = \mathbf{D}(z_0) \mathbf{W}^-(z_0, z_m) \delta_k \mathbf{R}^{\cup}(z_m, z_m) \mathbf{G}^+(z_m, z_0) \mathbf{S}(z_0). \quad (4.3)$$

Note that if we include all multiples at the detector side (instead of at the source side), one-way upward propagator $\mathbf{W}^-(z_0, z_m)$ in the above equation is replaced by the full wavefield propagator $\mathbf{G}^-(z_0, z_m)$. In that case, the full grid-point response matrix can be written as:

$$\delta_k \mathbf{P}(z_0; z_0) = \mathbf{D}(z_0) \mathbf{G}^-(z_0, z_m) \delta_k \mathbf{R}^{\cup}(z_m, z_m) \mathbf{W}^+(z_m, z_0) \mathbf{S}(z_0). \quad (4.4)$$

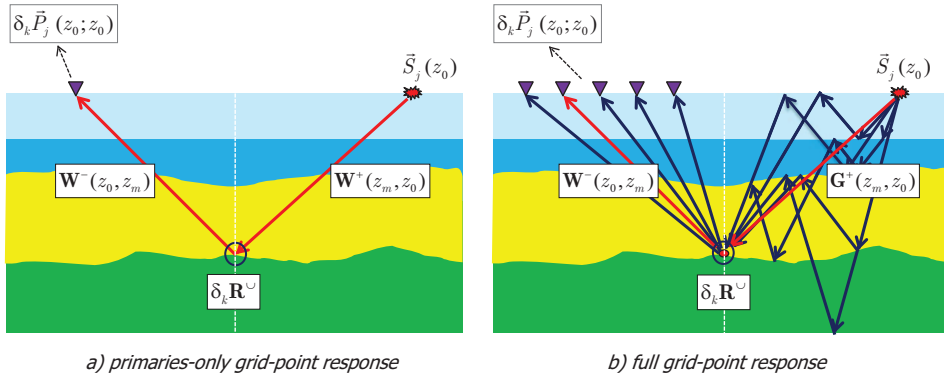


Figure 4.1: a) Grid-point response for primary reflections only, and b) same for primary as well as multiple reflections.

In the above formulations we kept all the multiples either at the source side or at the detector side. However, it is possible to split the multiples and divide them between the source side and the detector side. Wapenaar (1996) discussed the generalized primary representations, where internal multiples are equally shared between both sides. A further discussion on this way of splitting the multiples is beyond the scope of this thesis.

Figure 4.2a explains why the multiples provide additional angles of illumination leading to multi-angle illumination from a single shot record. Note that much more energy (sum of the squared amplitudes) is arriving at the grid-point than in the case of primaries-only illumination (see red arrow and the corresponding wavefield in red in Figure 4.2a). Moreover, this energy is arriving from different angles (referred as the changing angle events in the figure). Interestingly, by including all multiples, the target level will not only be illuminated from above by the incident source wavefield but also from below by the reflected wavefield from the deeper layers, as shown in Figure 4.2b. In this case, we rely completely on multiples. In some scenarios, e.g., in the presence of a complex overburden structure with strong 'shadow' effects, illumination from below may be the major illumination of the grid-point. The illuminating wavefield from below at depth level z_m can be expressed as:

$$\vec{P}_j^-(z_m; z_0) = \mathbf{G}^-(z_m, z_0) \vec{S}_j(z_0). \quad (4.5)$$

where operator $\mathbf{G}^-(z_m, z_0)$ carries all the complex propagation paths from primary source $\vec{S}_j(z_0)$ that, after scattering, reach depth level z_m from below.

In the next section, we discuss the modelling of illuminating wavefields from above as well as from below with the help of a 2-D numerical example.

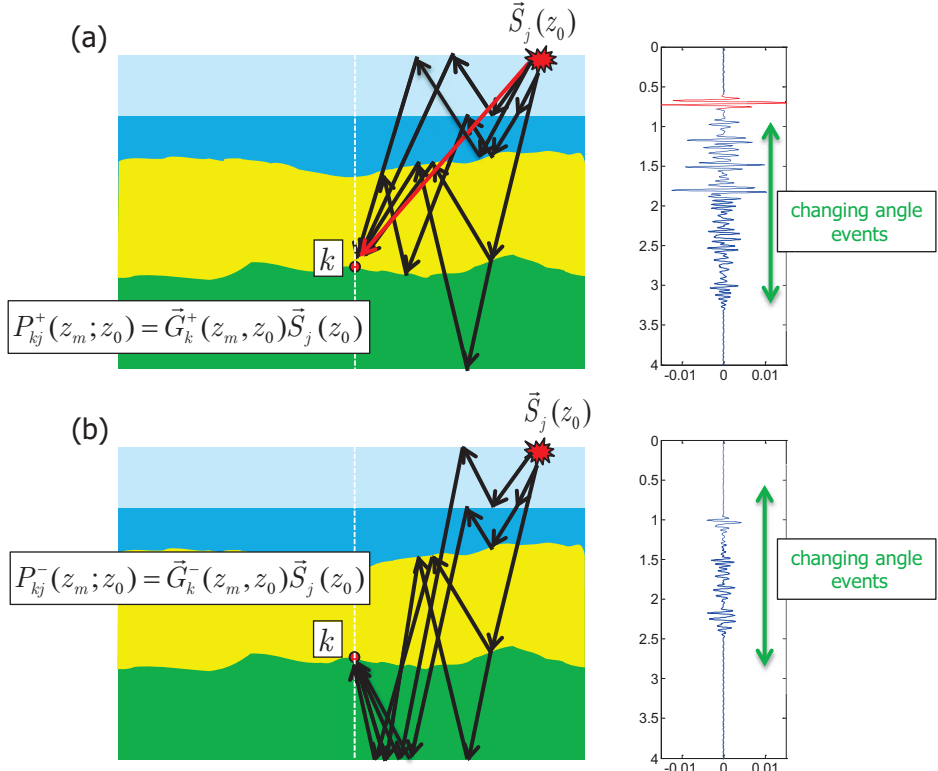


Figure 4.2: a) Illuminating wavefield incident at the grid-point from above. The red line shows illumination by primaries-only. b) Illuminating wavefield incident at the grid-point from below.

4.2.2 Modelling

To simulate full wavefield propagation (operators \mathbf{G}^+ and \mathbf{G}^-), a forward modelling method should be chosen that models the true wave propagation as accurately as possible, yet being computationally affordable. Depending on the efficiency and requirements, the user has the option to choose any available modelling scheme ranging from eikonal solvers (Vidale, 1988) to full 3D elastic finite-difference methods (Virieux, 1986). We have selected the modelling engine which is being used in full-wavefield migration (FWM) known as recursive acoustic full wavefield modelling, referred to as FWMod

(Berkhout and Verschuur, 2011; Davydenko and Verschuur, 2013; Soni and Verschuur, 2014).

This full wavefield modelling process consists of the two main steps: first, recursive one-way extrapolation of the up and downgoing wavefields from one depth level to another depth level; second, including the scattering in both directions at each depth level. Eventually, the iterative application of these steps going from the surface to the deepest level of interest and again back to the surface, results in two-way modelled data. The modelled wavefields are stored at each depth level in order to update scattered wavefields during the iterations. Every iteration is called a round-trip, in which a new order of scattering is included. The accuracy of this modelling method is high in 3-D complex media and can be compared with the accuracy of finite-difference methods. Note that, this forward modelling scheme in its structure is similar with what is referred to as the 'Generalized Bremmer series' (Corones, 1975; Wapenaar, 1996; Gustafsson, 2000).

In Berkhout (2014b), the FWMod engine has been explained extensively. Here, we will repeat the main wavefield relationships that are required for understanding the full-wavefield modelling. Let us define the wavefield convention for the upgoing and downgoing wavefields just above and just below a depth level z_m . The incoming downgoing $\vec{P}^+(z_m; z_{m-1})$ and upgoing $\vec{P}^-(z_m; z_{m+1})$ wavefields approach depth level z_m from above and below, respectively. In the same manner two types of wavefields $\vec{Q}^-(z_m)$ and $\vec{Q}^+(z_m)$, leave depth level z_m to the up and down direction, respectively. The matrices $\mathbf{R}^U(z_m, z_m)$ and $\mathbf{R}^D(z_m, z_m)$ represent reflectivity related to the discontinuities at depth level z_m for the wavefield coming from above and from below the layer, respectively. Similarly, The matrices $\mathbf{T}^+(z_m, z_m)$ and $\mathbf{T}^-(z_m, z_m)$ represent transmission properties related to the discontinuities at depth level z_m for the wavefield coming from above and from below the layer, respectively. We limit our discussions to P-waves only, although the reflection operators describe elastic PP reflectivity. For elastic full wavefield modeling, the readers are referred to Soni (2014).

The outgoing upward wavefield $\vec{Q}^-(z_m)$ at depth level z_m can be represented as a sum of the reflected wavefield at the current depth level and the transmitted upgoing wavefield that arrives at this depth level from below:

$$\vec{Q}^-(z_m) = \mathbf{R}^U(z_m, z_m) \vec{P}^+(z_m; z_{m-1}) + \mathbf{T}^-(z_m, z_m) \vec{P}^-(z_m; z_{m+1}). \quad (4.6)$$

To stress the influence of the effect of a parameter contrast at depth level z_m , the transmission effect is written as $\mathbf{T}^-(z_m, z_m) = \mathbf{I} + \delta \mathbf{T}^-(z_m, z_m)$, meaning

that $\delta\mathbf{T}^-(z_m, z_m) = 0$ if there is no contrast at z_m . Using this formulation, equation 4.6 is written as:

$$\vec{Q}^-(z_m) = \vec{P}^-(z_m; z_{m+1}) + \mathbf{R}^{\cup}(z_m, z_m) \vec{P}^+(z_m; z_{m-1}) \\ + \delta\mathbf{T}^-(z_m, z_m) \vec{P}^-(z_m; z_{m+1}). \quad (4.7)$$

It means the outgoing upward wavefield (\vec{Q}^-) can be expressed as the summation of the incident wavefield (\vec{P}^-) and the scattered wavefields ($\mathbf{R}^{\cup} \vec{P}^+ + \delta\mathbf{T}^- \vec{P}^-$). In a similar way, the outgoing downward wavefield $\vec{Q}^+(z_m)$ can be written as sum of the incident wavefield from above and the scattering terms as:

$$\vec{Q}^+(z_m) = \vec{P}^+(z_m; z_{m-1}) + \mathbf{R}^{\cap}(z_m, z_m) \vec{P}^-(z_m; z_{m+1}) \\ + \delta\mathbf{T}^+(z_m, z_m) \vec{P}^+(z_m; z_{m-1}). \quad (4.8)$$

As a final step in the wavefield relationships, the outgoing wavefields (\vec{Q}^+ and \vec{Q}^-) become the incoming wavefields (\vec{P}^+ and \vec{P}^-) at the neighboring depth levels via wavefield extrapolation:

$$\vec{P}^-(z_{m-1}; z_m) = \mathbf{W}^-(z_{m-1}, z_m) \vec{Q}^-(z_m). \quad (4.9)$$

and,

$$\vec{P}^+(z_{m+1}; z_m) = \mathbf{W}^+(z_{m+1}, z_m) \vec{Q}^+(z_m). \quad (4.10)$$

The propagation from one depth level to another depth level in our examples is carried out in a hybrid manner depending upon the complexity of the velocity model. Let us consider two scenarios: scenario one where the velocity does not vary laterally and scenario two where the velocity varies laterally. In the first scenario, the wavefield extrapolation has been implemented as a multiplication in the wavenumber-frequency domain (Gazdag and Sguazzero, 1984). In the second scenario, the wavefield extrapolation is computed by convolutions in the space-frequency domain (Holberg, 1988; Blacquière et al., 1989). The convolution operators are optimized using a weighted least-squares method (Thorbecke et al., 2004). Figure 4.3 illustrates the wavefield relationships used in FWMod.

Apart from being efficient, the reason for using this particular full wavefield modelling engine is to have full control over the order of multiple scattering modelled. This is a very important advantage for our analysis because it allows the contribution of each order of multiples (surface-related or internal) to be analysed separately. As we can model the incident wavefield at any grid-point from above and from below by this scheme, illumination at these grid-points from above and from below can also be analysed separately.

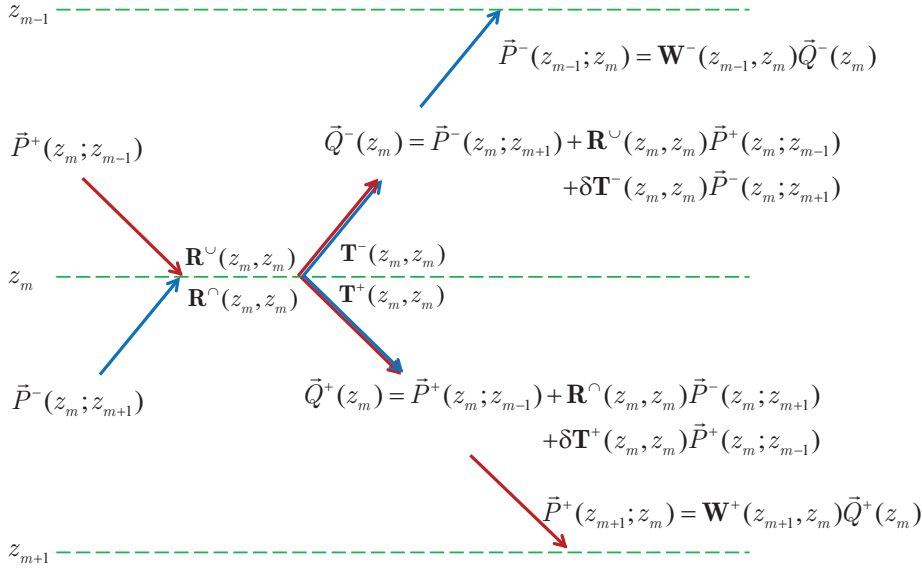


Figure 4.3: Full wavefield relationships of incoming (\vec{P}) and outgoing (\vec{Q}) wavefields. The outgoing wavefields (\vec{Q}^+ and \vec{Q}^-) are obtained by including the reflection and transmission operators (\mathbf{R} and \mathbf{T}) to the incoming wavefields (\vec{P}^+ and \vec{P}^-). These outgoing wavefields are then propagated to the next depth levels using the wavefield extrapolation operators (\mathbf{W}^+ and \mathbf{W}^-) to obtain the incoming wavefields.

Now, to illustrate the recursive full wavefield modelling scheme, we will give an example using the simple 1.5D reflectivity model shown in Figure 4.4a, where the velocity is assumed to be constant at 1500 m/s and the reflectivity is due to a density contrast only. Here, the aim is to compute a full illuminating wavefield from above and from below at a target point located at $(x, z) = (1500, 400)$ m (shown as the red triangle in Figure 4.4a). The arrows in Figure 4.4a indicate some typical examples of raypaths for the direct wavefield, the 1st order and the 2nd order of multiple scattering.

To compute the illuminating wavefield at any target point in the subsurface level z_m due to all sources at surface level z_0 , a source is put at that target point, its full-wavefield propagation is modelled and its response is recorded at the surface by the detectors. According to the reciprocity theorem (see e.g. Wapenaar, 1998), the result is the same as if the sources would be located at the surface and a detector would be located at the target point. The modelled illuminating wavefields from above at the target point are shown in Figures 4.4b, 4.4c and 4.4d, for the first, second and third iteration, re-

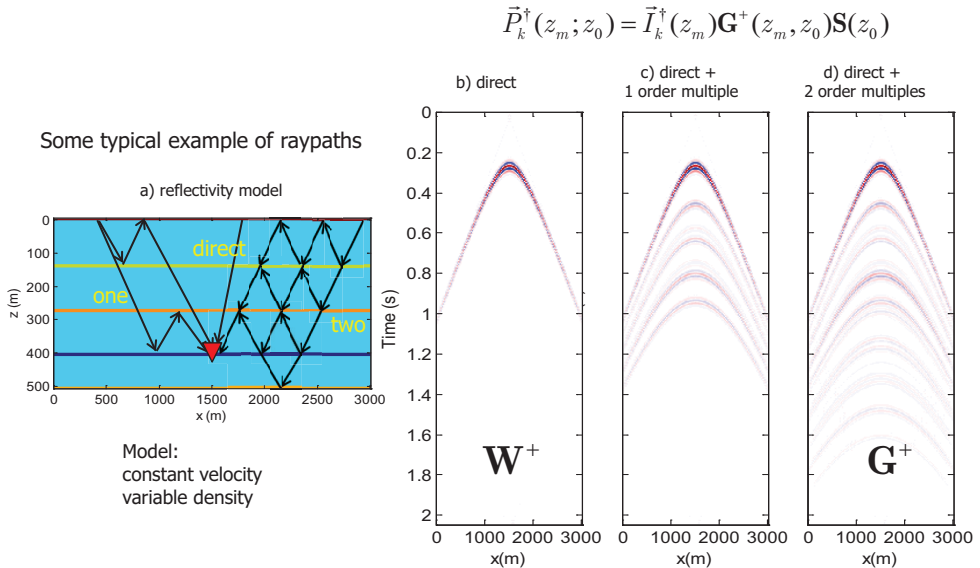


Figure 4.4: a) Reflectivity model, where arrows show the direction of the illuminating wavefield at the target point for different order of multiples, b) illuminating wavefield at the target point from above, direct wavefield, c) illuminating wavefield including one order of multiples and d) illuminating wavefield including two orders of multiples.

spectively. We can see that in the first iteration, the direct wavefield has been modelled only, and in each subsequent iteration, one higher order of multiples is modelled. Similarly, the illuminating wavefields from below has been modelled and shown in Figures 4.5b, 4.5c and 4.5d, for the first, second and third iteration, respectively. The arrows in Figure 4.5a indicate the full propagation paths of the illuminating wavefield from below. As expected in this case, we completely rely on multiples and, therefore, there is no direct wavefield in the first iteration of modelling (Figure 4.5b).

To summarize, the full wavefield modelling engine allows to control the modelling of any order of multiples (surface-related or internal) from above and/or from below, which allows us to fully assess the advantage of using multiples in the seismic acquisition analysis.

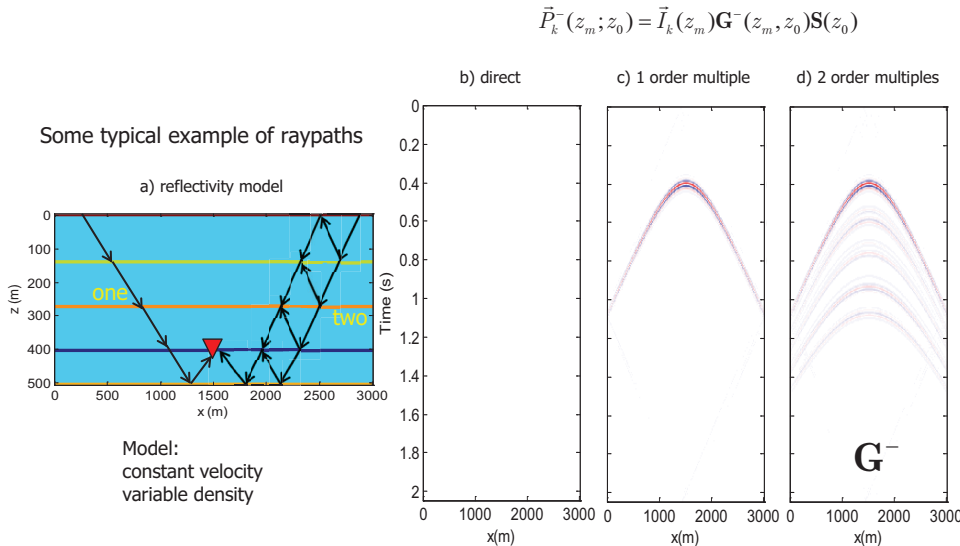


Figure 4.5: a) Reflectivity model, b-d) Illuminating wavefield at the target point from below, direct wavefield (not present) b), including one order of multiples c) and including two orders of multiples d).

4.2.3 Full wavefield focal beams

Starting with the double focusing concept, the double focusing result for the full wavefield grid-point response (equation 4.2) can be written as:

$$\delta_k \mathbf{P}(z_m; z_m) = \mathbf{F}(z_m, z_0) \mathbf{D}(z_0) \mathbf{W}^-(z_0, z_m) \delta_k \mathbf{R}^\cup(z_m, z_m) \times \mathbf{G}^+(z_m, z_0) \mathbf{S}(z_0) \underline{\mathbf{F}}(z_0, z_m). \quad (4.11)$$

The above equation is very similar to equation (2.12). However in this case, the focusing operator $\underline{\mathbf{F}}(z_0, z_m)$ at the source side should be computed such that it removes the effects of full wavefield propagation of $\mathbf{G}^+(z_m, z_0)$. The bar below the full wavefield focusing operator $\underline{\mathbf{F}}(z_0, z_m)$ differentiates it from primary focusing operator $\mathbf{F}(z_0, z_m)$. Again, the perfect migration would require a focusing operator $\underline{\mathbf{F}}$ such that:

$$\begin{aligned} \mathbf{G}^+(z_m, z_0) \mathbf{S}(z_0) \underline{\mathbf{F}}(z_0, z_m) &= \mathbf{I}, \\ \underline{\mathbf{F}}(z_0, z_m) &= [\mathbf{S}(z_0)]^{-1} [\mathbf{G}^+(z_m, z_0)]^{-1}. \end{aligned} \quad (4.12)$$

Operator \mathbf{G}^+ is a non-linear combination of one-way operators \mathbf{W} and reflectivity operators \mathbf{R}^\cup , which makes it a complex wavefield propagator.

Therefore, the inverse of \mathbf{G}^+ can not be expressed as its complex conjugate transpose, i.e., $[\mathbf{G}^+]^{-1} \neq [\mathbf{G}^+]^H$. Hence, we propose to compute the focal source beam at depth level z_m for the full wavefield by some minimization scheme.

Similar to equation (2.18), the full-wavefield focal source beam can be expressed as follows, replacing $\vec{W}_k^\dagger(z_m, z_0)$ by $\vec{G}_k^\dagger(z_m, z_0)$:

$$\vec{S}_k^\dagger(z_m, z_m) = \vec{G}_k^\dagger(z_m, z_0) \mathbf{S}(z_0) \mathbf{F}(z_0, z_m). \quad (4.13)$$

The term $\vec{G}_k^\dagger(z_m, z_0) \mathbf{S}^+(z_0)$ represents the full illuminating wavefield from above at the k^{th} grid-point location from all sources at the surface z_0 and it can be represented as $\vec{P}_k^\dagger(z_m; z_0)$. This wavefield can be modelled efficiently using the full-wavefield modelling scheme in combination with reciprocity and stored. The expression for the focusing operator from equation (4.12) can be substituted in equation (4.13) and then the expression for the full-wavefield focal source beam can be rewritten as:

$$\begin{aligned} \vec{S}_k^\dagger(z_m, z_m) &= \vec{P}_k^\dagger(z_m; z_0) [\mathbf{G}^+(z_m, z_0) \mathbf{S}(z_0)]^{-1}, \text{ or} \\ \vec{S}_k^\dagger(z_m, z_m) \mathbf{G}^+(z_m, z_0) \mathbf{S}(z_0) &= \vec{P}_k^\dagger(z_m; z_0). \end{aligned} \quad (4.14)$$

The above equation states that the full-wavefield beam $\vec{S}_k^\dagger(z_m, z_m)$ should be such that when it is forward propagated from the depth level z_m to the surface level z_0 in a full wavefield sense, then it should match with the full-illuminating wavefield $\vec{P}_k^\dagger(z_m; z_0)$. Based on this, we can formulate the estimation of the full-wavefield source beam as a minimization of the following objective function J in a least-square sense:

$$J = \left\| \vec{P}_k^\dagger(z_m; z_0) - \vec{S}_k^\dagger(z_m, z_m) \mathbf{G}^+(z_m, z_0) \mathbf{S}(z_0) \right\|_2^2. \quad (4.15)$$

The above optimization problem can be solved by an iterative gradient scheme. Here, we have used the conjugate gradient scheme (Hestenes and Stiefel, 1952). The solution in the steepest descent method steps in the negative direction of the gradient, and can be written as:

$$\Delta \vec{S}_k^\dagger(z_m, z_m) = \vec{E}_k^\dagger(z_m; z_0) [\mathbf{S}(z_0)]^H [\mathbf{G}^+(z_m, z_0)]^H. \quad (4.16)$$

where $\vec{E}_k^\dagger(z_m; z_0)$ is the residual wavefield, given by:

$$\vec{E}_k^\dagger(z_m; z_0) = \vec{P}_k^\dagger(z_m; z_0) - \vec{S}_k^\dagger(z_m, z_m) \mathbf{G}^+(z_m, z_0) \mathbf{S}(z_0). \quad (4.17)$$

Equation (4.16) can be interpreted as the reverse full-wavefield modelling of the residual wavefield. The gradient for the objective function (4.15) is computed such that it provides a solution for a beam $\vec{S}_k^\dagger(z_m, z_m)$ of having minimum energy. This prevents the iterative scheme to arrive at the obvious solution that is $\vec{S}_k^\dagger = \vec{I}_k^\dagger$. The full-wavefield focal source beam at depth level z_m is an estimate of full-wavefield focusing in emission at the grid-point under consideration, i.e., $\vec{S}_k^\dagger(z_m, z_m) = \langle \vec{I}_k^\dagger \rangle$. At any iteration i , the update of focal source beam can be computed by finding the appropriate step-length α in the gradient scheme, as:

$$\langle \vec{S}_k^\dagger(z_m) \rangle^i = \langle \vec{S}_k^\dagger(z_m) \rangle^{i-1} + \alpha \Delta \vec{S}_k^\dagger(z_m), \quad (4.18)$$

such that the objective function J is minimized. The initialization of this minimization scheme starts by taking $\langle \vec{S}_k^\dagger \rangle^{(0)} = 0$ and $\vec{E}_k^\dagger(z_m; z_0) = \vec{P}_k^\dagger(z_m; z_0)$. We perform the iterative process until the estimated beam explains the total modelled full illuminating wavefield sufficiently well.

Figure 4.6 shows a generalized block diagram of the inversion scheme for full-wavefield focusing in emission. The final result of this full-wavefield focusing in emission is referred to as the focal source beam at depth level z_m , which shows the focusing capability of a source geometry using all multiples. The beam computation by such a minimization scheme is very similar to the estimation of the reflectivity by the full-wavefield migration (Davydenko et al., 2012). The difference is that we are interested in finding the effects on the image quality of a certain target area caused by the acquisition geometry rather than finding the subsurface properties themselves.

As mentioned already, all the complexity by the multiples is kept at the source side in the modelling of the grid-point response, meaning that detector side focusing can be done by using the same focusing operator as for the primaries-only wavefield (equation 2.13). Therefore, the focal detector beam computation is unchanged.

Everything we discussed so far about illumination from above, we can repeat for illumination from below. To compute the target illumination from below, in equation (4.15), the illuminating wavefield from above $\vec{P}_k^+(z_m; z_0)$ should be replaced by the illuminating wavefield from below $\vec{P}_k^-(z_m; z_0)$ and also the operator $\mathbf{G}^+(z_m, z_0)$ should be replaced by the operator $\mathbf{G}^-(z_m, z_0)$. The objective function for illumination from below can be written as:

$$J = \left\| \vec{P}_k^-(z_m; z_0) - \vec{S}_k^\dagger(z_m, z_m) \mathbf{G}^-(z_m, z_0) \mathbf{S}(z_0) \right\|_2^2. \quad (4.19)$$

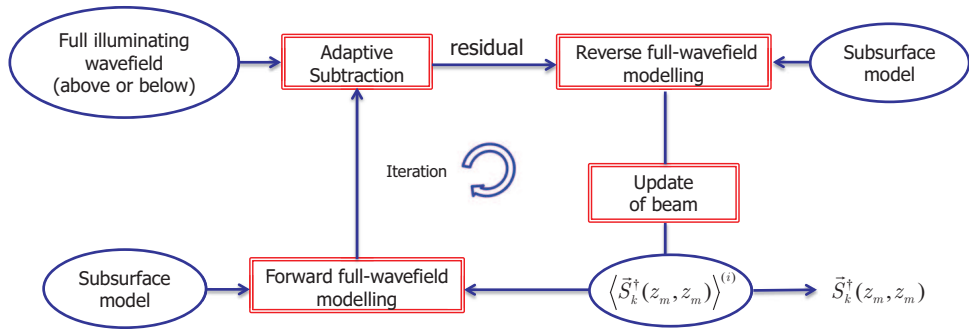


Figure 4.6: Block diagram showing the feedback loop for the computation of the full-wavefield focal beam. The estimated beam at the target level is used to simulate the response using full-wavefield modelling, which is compared with the modelled illuminating wavefield at the target point by the available primary sources at the surface. The residual of these two wavefields is fed back in the loop, using the reverse full-wavefield modelling process, to update the beam iteratively.

The above optimization problem can be solved in a similar way by an iterative gradient scheme and the results obtained by solving this objective function can be referred as a full-wavefield focal source beam for the illuminating wavefield from below. It provides illumination angles incident at the target level from below, after reflecting from deeper layers (Figure 4.5a).

4.2.4 Illustration of the full wavefield focal beam concept

To illustrate the above mentioned least-squares inversion approach for full-wavefield focusing, we use again the synthetic reflectivity model shown in Figure 4.4a and the modelled full illuminating wavefield $\vec{P}_k^\dagger(z_m; z_0)$ shown in Figure 4.4d. In this example, the primary sources are available everywhere from 0 m to 3000 m along the surface with a sampling interval of 10 m. Therefore, we do expect a proper focusing at the target location in the spatial domain.

The result after the first iteration is shown in Figure 4.7a. We do observe a focus at the lateral position of the target point at $t = 0$ s but also a number of events at other times. The events at other times are due to the focusing operator being approximated in this first iteration by \mathbf{G}^H instead of the exact inverse of \mathbf{G} , which results in the cross correlation artefacts.

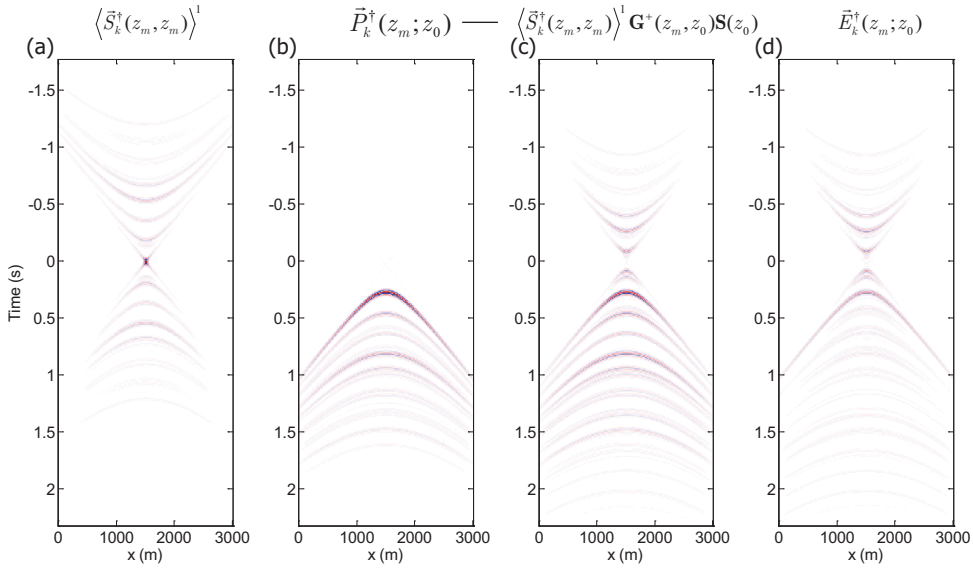


Figure 4.7: First iteration result of full wavefield focal source beam computation: a) estimated beam at the target location, b) the full illuminating wavefield, c) the wavefield modelled using the estimated beam and d) the residual wavefield.

The residual wavefield at the surface, being the difference between the full illuminating wavefield (Figure 4.7b) and the simulated response using full-wavefield modelling with the current estimated beam (Figure 4.7c), is shown in Figure 4.7d. This residual wavefield is fed back into the loop using the reverse full-wavefield modelling to update the beam iteratively (equation 4.18). The result after 10 iterations is shown in Figure 4.8a. Note that there are no undesired events at other times anymore resulting in a perfect focusing at $t = 0$ s and also the residual wavefield (Figure 4.8d) is reduced to almost zero.

The Radon transforms of the estimated beam for the first iteration and the tenth iteration are shown in Figure 4.9. They provide the angle information contained in the beam at $\tau = 0$ s. Again we observe a number of events at other times as well in the first iteration Radon transformed beam (Figure 4.9b), which is suppressed fully in the tenth iteration (Figure 4.9d).

The example discussed so far had an almost perfect source geometry. Therefore, the illumination by the primaries-only wavefield was already good enough for this simple subsurface model and multiples didn't improve the illumination. So far, the primary source geometry was limited and it will now be

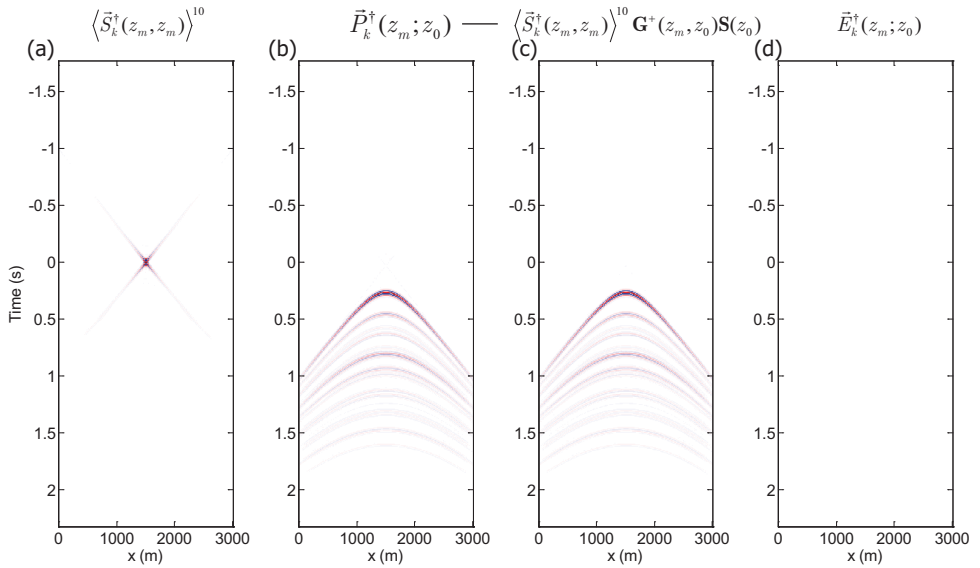


Figure 4.8: Tenth iteration result of full wavefield focal source beam: a) estimated beam at the target location, b) the full illuminating wavefield, c) the wavefield modelled using the estimated beam and d) the residual wavefield.

shown that multiples help to improve the illumination angles especially towards smaller angles.

In the next example, the source geometry comprises two source arrays of 100 sources with sampling interval of 10 m (shown in Figure 4.10a). There is a big gap in the distribution of the sources. Figures 4.10b, c and d show the primaries-only illuminating wavefield from above, the full illuminating wavefield from above (primaries plus two orders of multiples, i.e., three roundtrips) and the full illuminating wavefield from below at the target point by the corresponding sources, respectively. It may be noticed that there are many multiple reflections coming from different reflectors, which will subsequently help to improve the illumination and the focusing.

The focal source beam is computed by the above mentioned minimization method. Figure 4.11 shows the focal source beam for primaries-only illuminating wavefield in the spatial as well as in the Radon domain. As expected, the focusing capability for this source geometry suffers from the large gap between the two source arrays in the spatial domain and it also shows two ranges of angles coming from both sides in the Radon domain. Results for

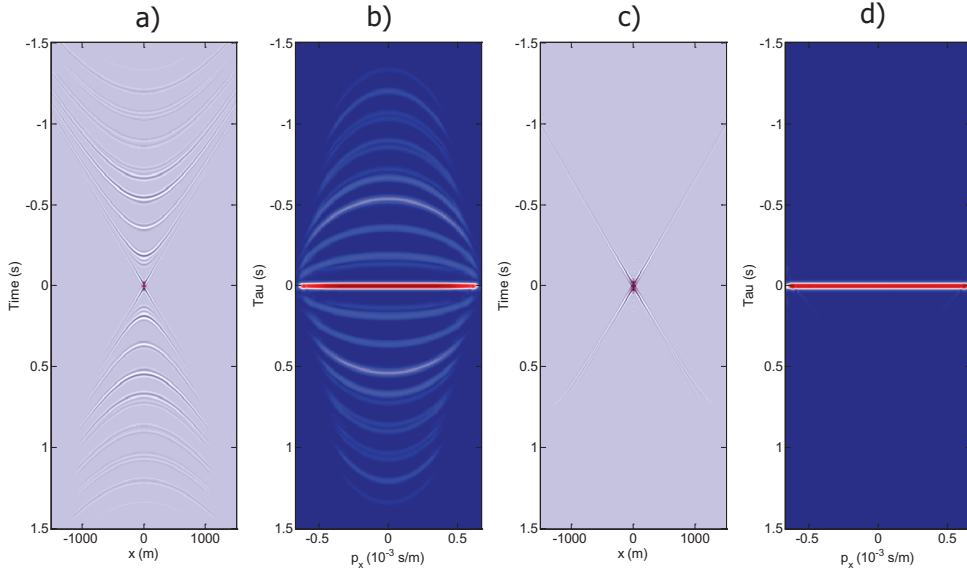


Figure 4.9: First and tenth iteration result of full wavefield focal source beam: a) the estimated beam after the first iteration result in the spatial domain, b) same in the Radon domain, c) the estimated beam after 10th iteration result in spatial domain, and d) same in the Radon domain.

the zero intercept time are shown in Figure 4.12.

Next, we show the results of focal source beam for the full illuminating wavefield from above. They are shown in Figure 4.13. It may be observed that the focusing is sharper in the spatial domain and the illumination is wider in the Radon domain at the $\tau = 0$ s compared to primaries-only results (Figure 4.11). A slice at time $t=0$ s has been plotted in Figure 4.14 for a closer view of the amplitudes. It is noticed that the amplitude of the main lobe in spatial domain is higher than in Figure 4.12a, whereas in the Radon domain, the amplitudes of the extra illumination-angles are weaker than the primaries as the primaries are stronger than the multiples (Figure 4.14b). However, there may be cases where primaries are weaker than multiples. One such case will be discussed in the next chapter.

Further, the illumination from below at the target point has been analyzed and the incident wavefield from below $\vec{P}_k^-(z_m, z_0)$ has been computed using equation (4.5) for the same model (Figures 4.10d). As explained earlier there is no direct illuminating wavefield present from below. Hence, solving objective function (equation 4.19) for this wavefield will provide only the

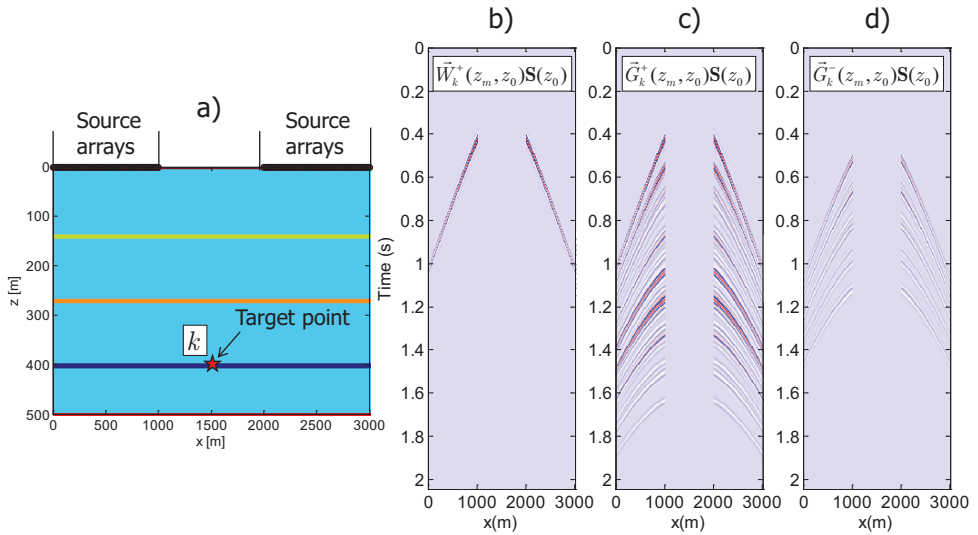


Figure 4.10: a) Reflectivity model with position of two source arrays and the target point, b) primaries-only illuminating wavefield at the target point from all available sources at the surface, c) full illuminating wavefield from above at the target point, and d) full illuminating wavefield from below at the target point from all available sources at the surface.

focusing capabilities of secondary sources created by the available primary sources $\mathbf{S}(z_0)$. The results are shown in Figure 4.15.

A slice at the zero intercept time is plotted in Figure 4.16 and the angles by which the target point is illuminated from below can be seen in this figure. These angles are required for estimating the down-side reflection coefficient at the target point.

4.3 Full wavefield focusing operator

In the previous section, we formulated the computation of the focal source beam at depth level z_m as a minimization problem. In this scheme, we utilized the fact that the full wavefield focusing operator $\mathbf{F}(z_0, z_m)$ should be the exact inverse of the full wavefield propagation operator $\mathbf{G}^+(z_m, z_0)$. However, we did not specifically solve for this focusing operator, rather we solved for the final focusing results. It would be interesting to see the focusing operator itself. In this section, we will formulate the objective function to

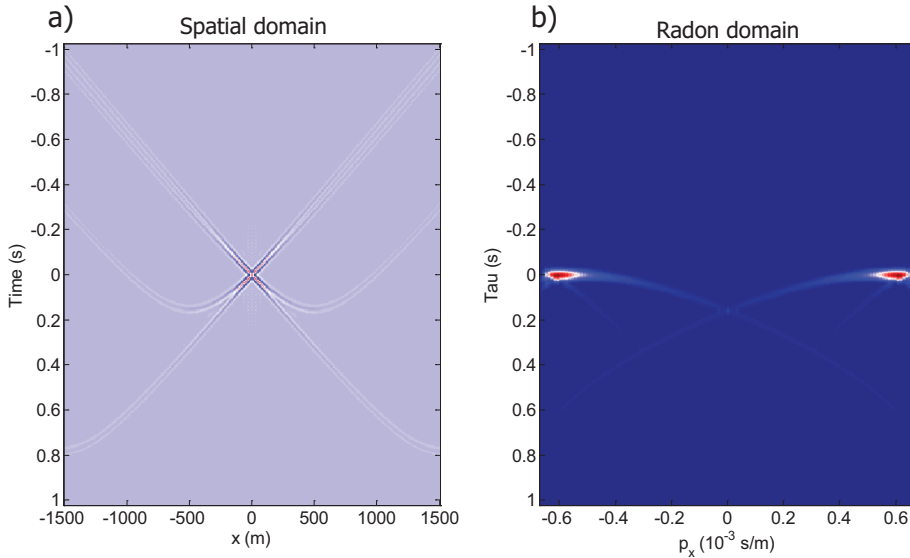


Figure 4.11: a) Focal source beam in the spatial domain for all times, b) same in the Radon domain for the primaries-only wavefield.

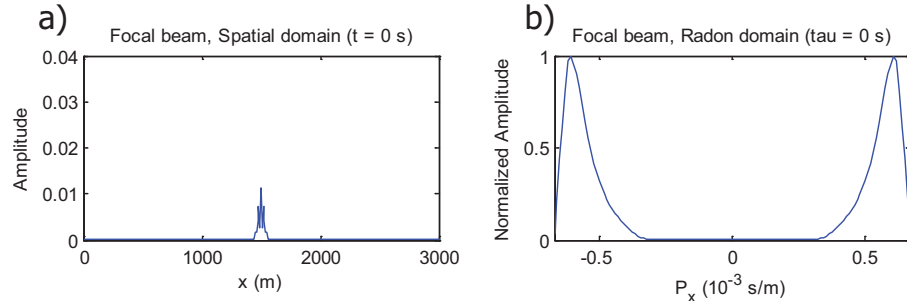


Figure 4.12: a) Focal source beam at time $t = 0 \text{ s}$ in the spatial domain; b) same at $\tau = 0 \text{ s}$ in the Radon domain for the primaries-only wavefield.

solve for the focusing operator. Let us recall the equation (4.12):

$$\mathbf{G}^+(z_m, z_0) \mathbf{S}(z_0) \underline{\mathbf{F}}(z_0, z_m) = \mathbf{I}. \quad (4.20)$$

The above equation can be solved as a minimization problem to find the focusing operator. The following objective function can be formulated as:

$$J = \|\mathbf{G}^+(z_m, z_0) \mathbf{S}(z_0) \underline{\mathbf{F}}(z_0, z_m) - \mathbf{I}\|_2^2. \quad (4.21)$$

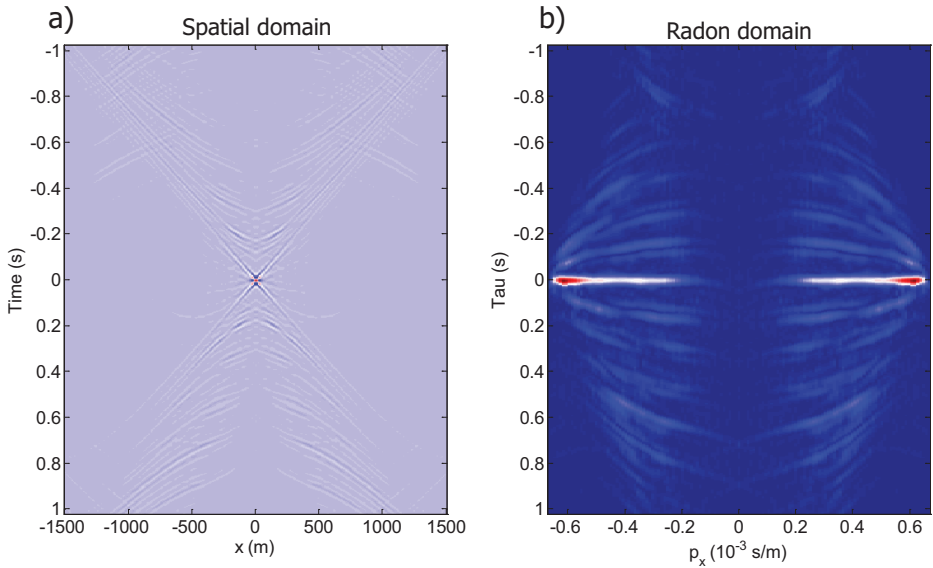


Figure 4.13: a) Focal source beam in the spatial domain for all times, b) same in the Radon domain for the full illuminating wavefield from above.

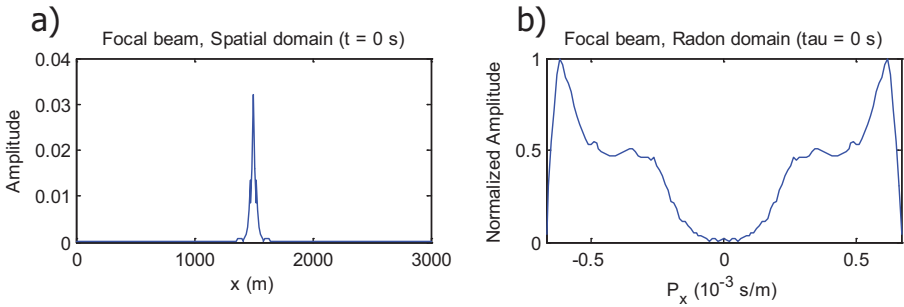


Figure 4.14: a) Focal source beam at time $t = 0$ s in the spatial domain; b) same at $\tau = 0$ s in the Radon domain for the full illuminating wavefield from above.

This minimization problem can be solved by an iterative gradient scheme. The gradient of the objective function is expressed as:

$$\Delta J = [\mathbf{G}^+(z_m, z_0) \mathbf{S}(z_0)]^H \mathbf{E}(z_m). \quad (4.22)$$

where $\mathbf{E}(z_m)$ is the residual at depth level z_m , given by:

$$\mathbf{E}(z_m) = \mathbf{G}^+(z_m, z_0) \mathbf{S}(z_0) \mathbf{F}(z_0, z_m) - \mathbf{I}. \quad (4.23)$$

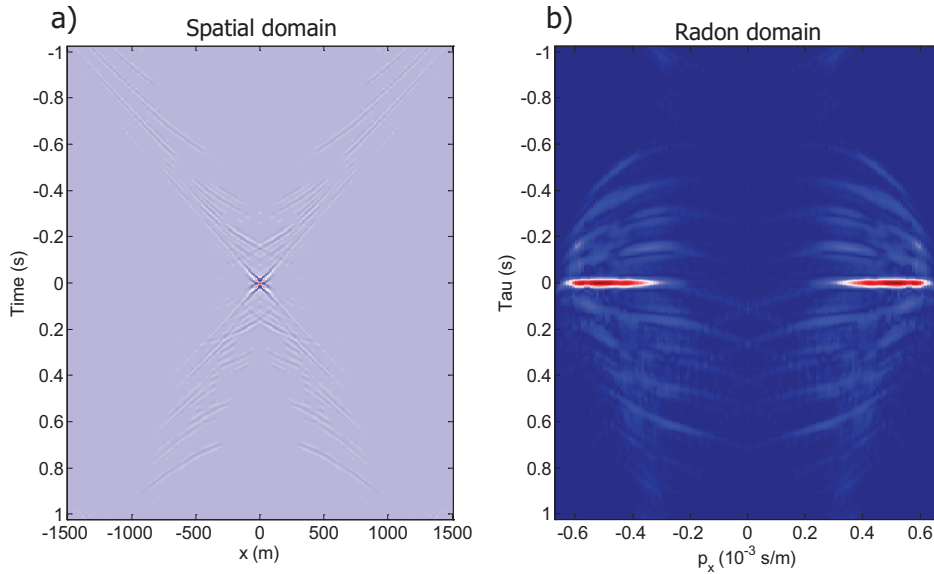


Figure 4.15: a) Focal source beam in the spatial domain, and b) same in the Radon domain for the multiples-only illuminating wavefield at the target point from below.

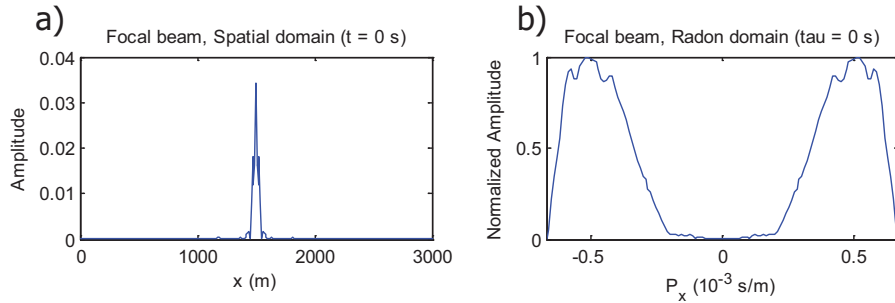


Figure 4.16: a) Focal source beam at time $t = 0$ in the spatial domain, and b) same at $\tau = 0 \text{ s}$ in the Radon domain for the multiples-only illuminating wavefield incidenting at the target point from below.

The update of the focusing operator can be found by finding the appropriate step-length α in the gradient scheme, as:

$$\langle \underline{\mathbf{F}}(z_0, z_m) \rangle^i = \langle \underline{\mathbf{F}}(z_0, z_m) \rangle^{i-1} + \alpha \Delta \underline{\mathbf{F}}(z_0, z_m). \quad (4.24)$$

The iteration process goes on until the residual $\mathbf{E}(z_m)$ (equation 4.23) becomes close to zero. The first iteration result of the the full wavefield focusing

operator is the complex conjugate (time-reversed) of the propagation operator (\mathbf{G}) as \mathbf{G}^H .

To illustrate this method for finding the full wavefield focusing operator, we use the same 1.5 D reflectivity model used earlier and will solve for the focusing operator at a target point located at $(x_k, z) = (1500, 400)$ m (shown as the red triangle in Figure 4.4a). The source geometry will be taken as densely distributed within the available aperture. By emitting the focusing operator into the actual medium in a full wavefield sense, focusing occurs at target depth level and the focus is proportional to a bandlimited version of $\delta(x - x_k)\delta(t)$, where x_k is the lateral location of the target point at depth level z_m .

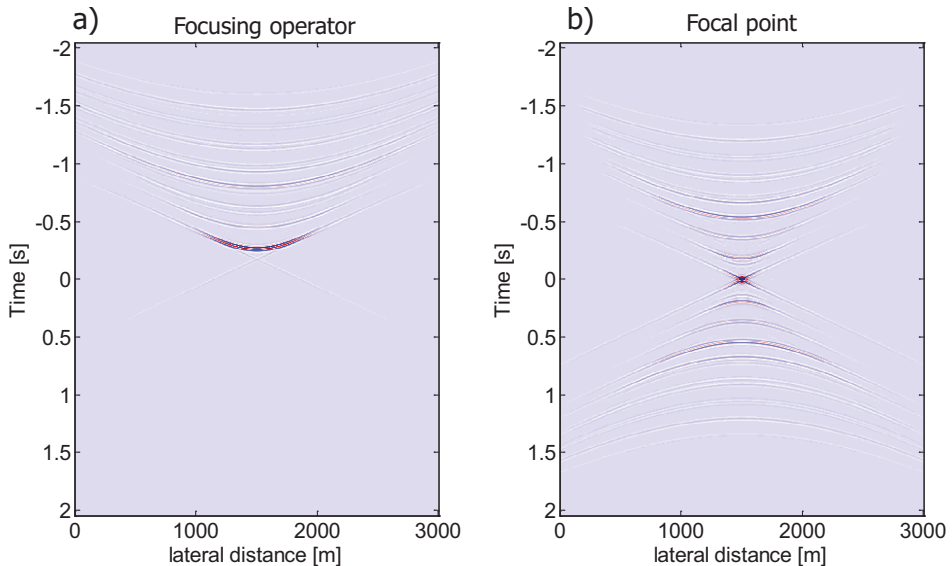


Figure 4.17: a) Focusing operator after first iteration, and b) its corresponding focusing result. The focusing result is not yet perfect.

The result of the focusing operator and the focusing results after the first iteration is shown in Figure 4.17. It is clearly observed that the focusing operator is the complex conjugate transpose of the full propagation operator after the first iteration, hence the focusing is not a bandlimited version of $\delta(x - x_k)\delta(t)$. The result after the 10th iteration is shown in Figure 4.18. By emitting this final focusing operator in to the actual medium, the focusing becomes a bandlimited version of $\delta(x - x_k)\delta(t)$ (Figure 4.18b). Note the dif-

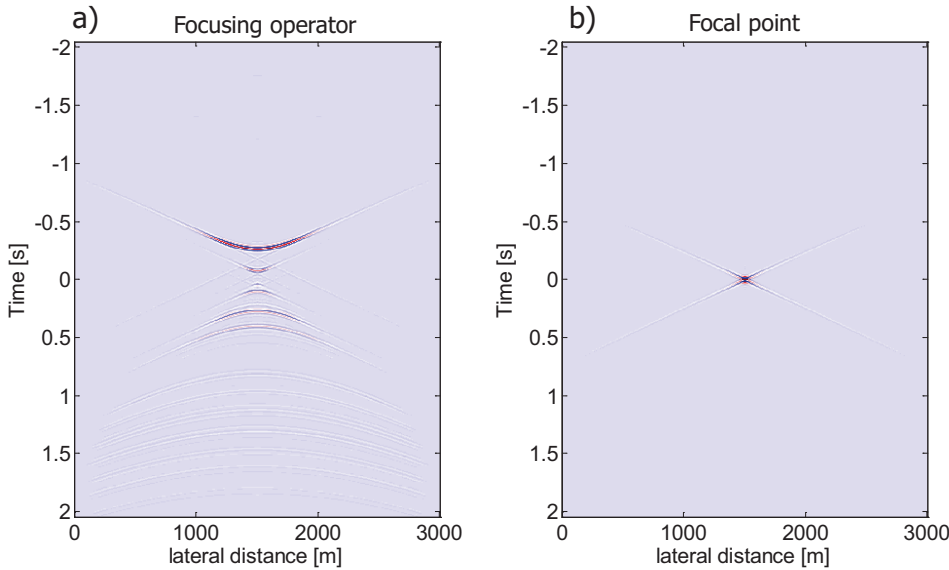


Figure 4.18: a) Focusing operator after 10th iteration, and b) its corresponding focusing result. The focusing result is now perfect.

ference between the iteration one focusing operator and iteration ten focusing operator. In both cases, there is the time-reversed direct arrival. However, in Figure 4.17a the coda is purely acausal (i.e., preceding the time-reversed direct arrival), the coda in Figure 4.18a is purely causal (i.e., it follows the time-reversed direct arrival).

The final focusing operator is referred as type-2 focusing function in the Marchenko imaging papers (see e.g. Wapenaar et al., 2014a; Slob et al., 2014; Wapenaar et al., 2014b). In this methodology, the focusing operator is retrieved directly from the reflection response and an estimate of the direct arrival. In our method, we retrieve the focusing operator by inversion of the modelled response of a source located at the grid-point in the subsurface, measured by the detectors at the surface. A similar method can be applied to data measured in borehole seismic, i.e., seismic interferometry by multi-dimensional deconvolution (MDD) (Wapenaar et al., 2011; van der Neut et al., 2011) also inverts the measured transmission response and applies this inverse to the reflection data measured in the horizontal borehole.

4.4 Conclusion from this chapter

In the last few years, we observe a trend towards using multiples in the imaging process. We therefore proposed to study seismic acquisition geometry analysis via focal beams, and to include in this analysis the illumination by all (primaries and) multiples. The existing so-called focal beam method for primary reflections was expanded to include all multiples as well. In this chapter, the grid-point response is formulated such that all the complex wave propagation paths by the multiples are kept on the source side, leading to a complex full illuminating wavefield. As a result of the complex illuminating wavefields involved, the focal beam needs to be computed by a minimization scheme. These focal beams describe the potential imaging capabilities of the source and detector geometries in terms of resolution and angle-dependent information. This avoids the need to carry out full 3-D survey simulation in order to access its imaging capabilities.

Finally, illumination from below can also be analysed by this method, which shows the potential of a source geometry in imaging from below. Illumination from above as well as from below by multiply reflected wavefields reveals information at angles that may not be present in illumination by primary reflections. This feature can be exploited in the acquisition design. It may either lead to a much improved image of the subsurface for the same acquisition geometry, or to a more cost-effective acquisition geometry for the same image quality. This extended analysis via focal beams can be used for effective survey design, assuming that multiples will be used in imaging and reservoir characterization on a routine basis.

Chapter 5

Extending illumination using all multiples: *examples*

5.1 Introduction

In the previous chapter, the theory of the focal-beam concept was extended to the multiples. The concept was illustrated with simple layer-model examples and it was shown that multiples provide additional illumination angles. In this chapter, the image quality to be obtained from several general and specific acquisition geometries (2-D and 3-D) will be determined by focal beam analysis for primaries as well as multiples. The main illustrations of this chapter include:

- the influence of an irregularly shaped salt structure on illumination strength.
- the primaries-only wavefield illumination versus the full-wavefield illumination for different geometry: less sources, same illumination (economics).
- the illumination from above as well as from below for 3-D geometries and their impact on angle-dependent reflectivity.
- limited illumination due to geology, even in the case of a perfect source distribution: improvement by using multiples.
- the resolution and the AVP functions for shallow and deep targets.

Furthermore, we also provide a 2-D example of full-wavefield migration (FWM) to show that multiples not only extend the illumination angles but also provide additional subsurface image points. In all examples that follow, extended focal beam analysis will always be applied for a single target point (i.e. at one depth level). Note that the point diffractors at the target boundary for which the migrated response is analysed can also cause artifacts at different depth levels. These artifacts are left aside in this chapter.

5.2 Two-dimensional example

The illustrations in this section show the influence of an irregularly shaped salt structure on illumination strength using primaries as well as multiples. The velocity model and the reflectivity model are shown in Figure 5.1.

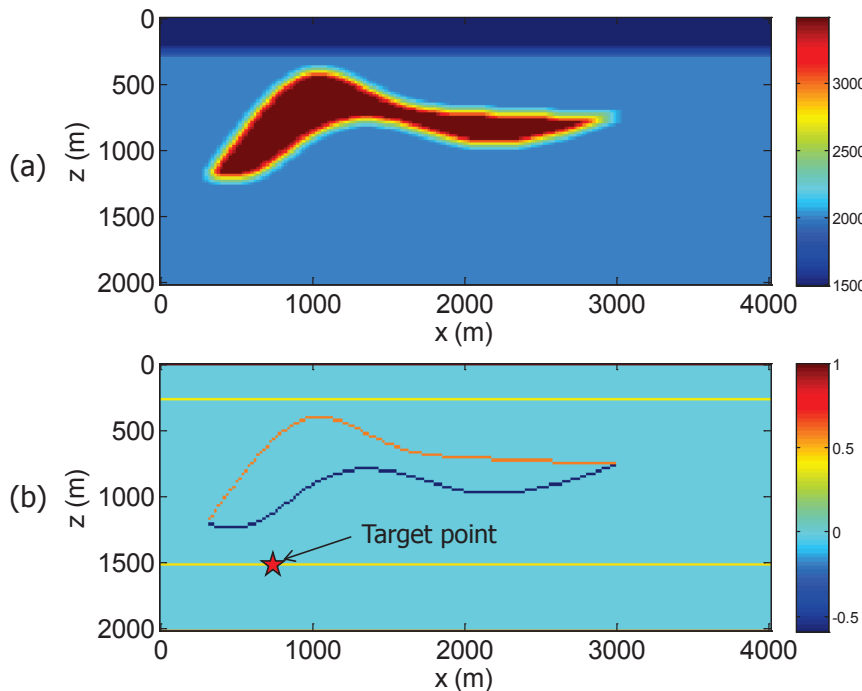


Figure 5.1: a) The 2-D velocity model and b) the 2-D reflectivity model. The target point is indicated by the red star.

Note that the reflectivity at 1500 m depth is due to a density contrast only. A target point located laterally at 900 m and vertically at 1500 m has been

chosen for the analysis (indicated by the red star in Figure 5.1b). The source wavelet has a Gaussian spectrum with a frequency range of 5 Hz to 30 Hz.

To see the effect that the salt body causes on the wavefield, let us look at the wavefield propagating upward from a point diffractor located at the target point. Figure 5.2a shows the energy of upward traveling waves for the primaries-only wavefield and Figure 5.2b shows the same for the full wavefield (primaries as well as all multiples). It may be observed that there is enhancement in energy of upward propagating waves using all multiples. Even at the far offsets, there is a considerable amount of energy arriving at the surface in the case of the full wavefield versus negligible energy in the case of the primaries-only wavefield.

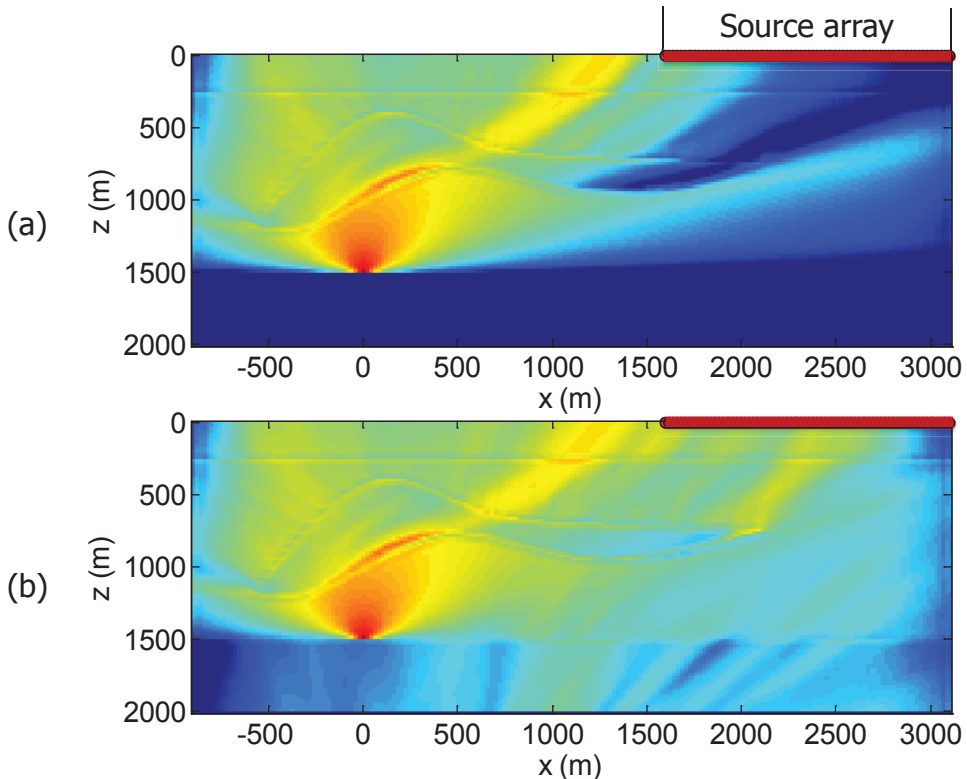


Figure 5.2: a) Forward propagating energy from a point diffractor ("upward radiating buried source") for the primaries-only wavefield and b) same for the full wavefield. The source array is indicated by a red line.

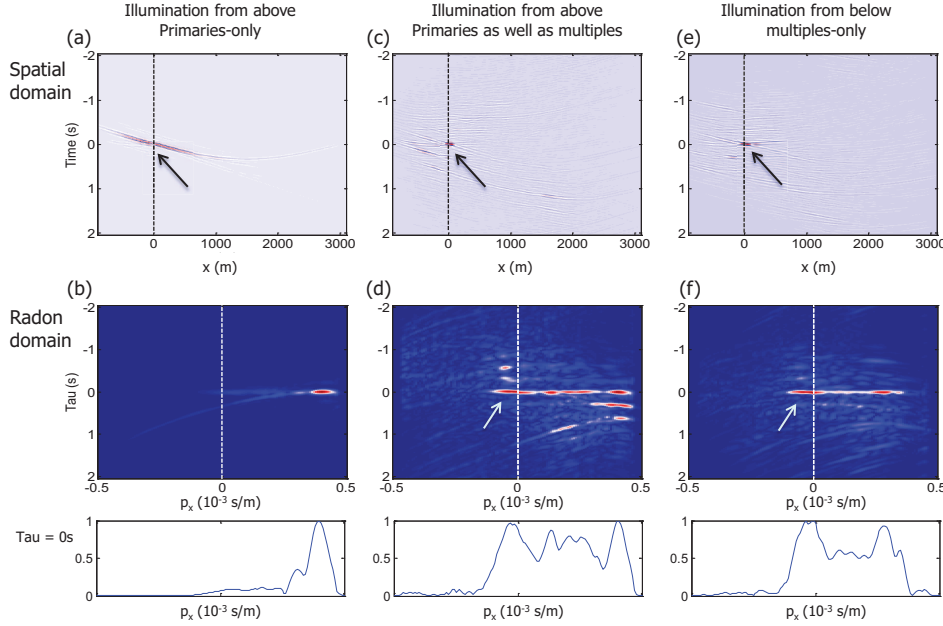


Figure 5.3: The focal source beam in the spatial domain as well as in the Radon domain a) and b) for the primaries-only wavefield, c) and d) for the full wavefield from above, e) and f) for the multiples-only wavefield incidenting from below. The black arrows show the focusing point. The white arrows indicate illumination at the negative p -values. The bottom row shows the slice at $\tau = 0$ s for closer view of amplitudes.

Sources at a sampling interval of 10 m within an aperture of 1500 m have been taken, located at the right side of the target point (shown in Figure 5.2 by a red line), and the focal source beam has been computed to find the focusing capabilities of this source geometry. As sources are present at the right side of the target point only, no proper focusing is expected in the case of the primaries-only wavefield. This can be clearly observed in Figure 5.3a. In the Radon domain, a small range of illumination angles is visible at positive p -values (Figure 5.3b).

Multiples here help in widening the range of angles of illumination and they even illuminate the target point from the opposite direction, i.e., negative p -values are present, see Figure 5.3d. This results in better focusing and, hence, better illumination, see Figure 5.3c. Till now, we discussed the illumination from above. The illumination from below at the target point for this source geometry was also analysed and the results are shown in Figures 5.3e and 5.3f. A slice at $\tau = 0$ s has been plotted at the bottom row in Figure 5.3

for a better view of the amplitudes for each case. As discussed earlier, there is no direct illuminating wavefield in the case of illumination from below and indeed Figure 5.3f shows no illumination angles contained in the direct wavefield (Figure 5.3b). The illumination angles from below are required to estimate the down-side reflection coefficient \mathbf{R}^\cap (as opposed to \mathbf{R}^\cup) at the target point in the imaging from below.

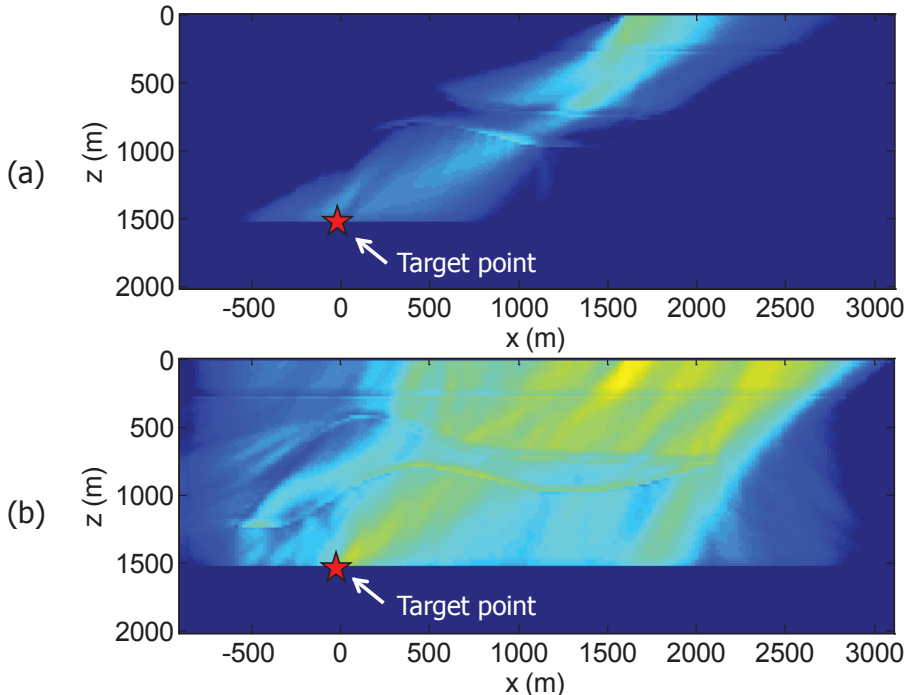


Figure 5.4: a) Back propagated energy from the surface level to the target level for the primaries-only wavefield and b) same for the full wavefield for the case of illumination from above.

The effect that the illumination improves when using multiples can be explained by back propagating the energy as shown in Figure 5.4. This is inversely extrapolated energy from the available sources at the surface to the target level. It shows that more energy is reaching the target level and from more directions in the case of the full wavefield (Figure 5.4b) than in the case of the primaries-only wavefield (Figure 5.4a).

From the preceding example, it seems likely that the more complex the subsurface is, the more extra angles are contained in the secondary source wavefield generated by the multiples.

5.2.1 Analysis of different geometries

The above example contained a comparison of the primaries-only wavefield illumination with the full wavefield illumination for the same source geometry. It has been shown that the illumination improved using multiples. We also performed an analysis of the primaries-only wavefield illumination versus the full wavefield illumination for a different geometry. Figure 5.5a shows the focusing result for the primaries-only case with sources having a 3000 m aperture which is compared with the focusing result for the full-wavefield illumination case with sources having a 1500 m aperture (Figure 5.5b). It can be clearly noticed that the illumination angles at $\tau = 0$ s in both cases are the same, which shows that a source geometry design for primaries and multiples leads to different solutions.

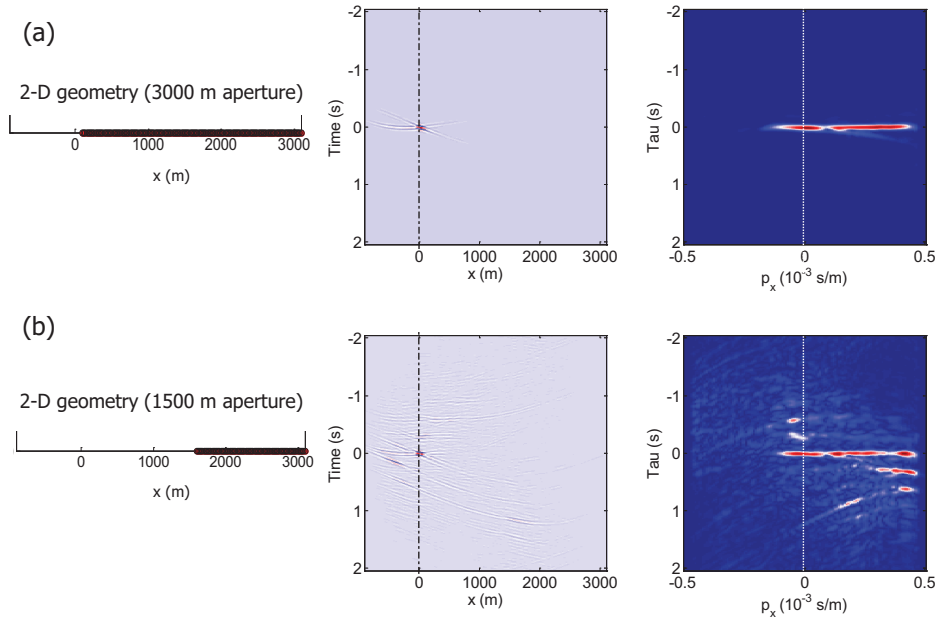


Figure 5.5: Comparison of the focusing results for the primaries-only wavefield using 3000 m aperture a) with the result for the full wavefield using 1500 m aperture b).

5.2.2 Space variance of the beam quality

So far, the full wavefield focal beam analysis was carried out for only one target point in the subsurface and the angle-dependent results were found at

$\tau = 0s$ in the ray-parameter domain. In order to evaluate the spatial variability of the angle dependent information, we need to compute the focal beam results along the horizon. Again, we choose to compute the angle-dependent information along an angle-independent reflector. In this way, the source geometry, detector geometry, propagation and migration are considered separately from the reflectivity of the target reflector. Ideally the results would show a uniform amplitude as a function of ray parameter for all lateral locations along the reflector. Any deviation from this uniform amplitude value implies an acquisition imprint on the angle-dependent reflection coefficient of the target reflector.

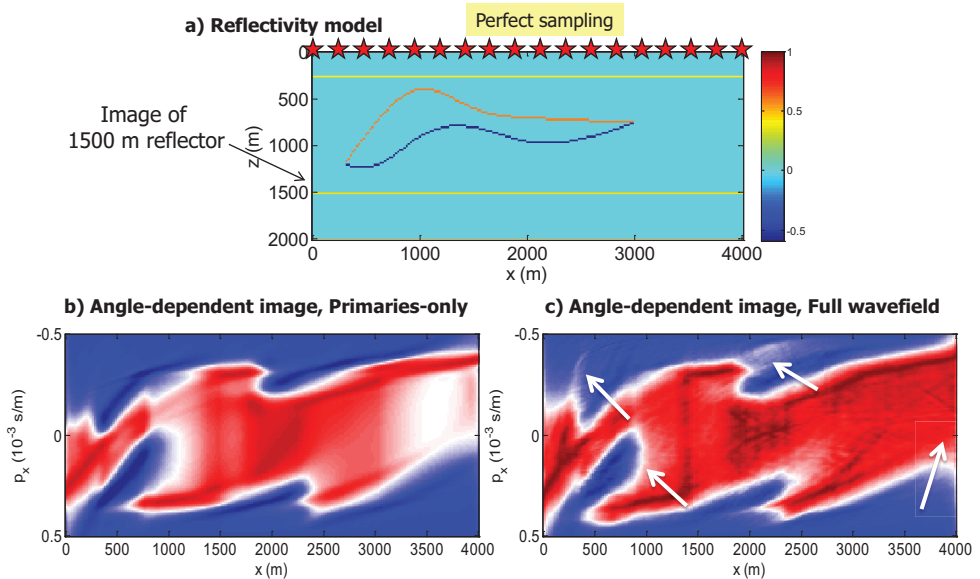


Figure 5.6: a) The salt reflectivity model with the source geometry indicated by the red stars, b) estimated reflectivity as function of ray-parameter for the primaries along the reflector at $z = 1500$ m and c) same for the full wavefield.

In this section, we estimate the reflectivity as a function of ray-parameter along the 1500 m angle-independent reflector for two different geometries. The first geometry has a perfect source sampling (shown in Figure 5.6a by the red stars) whereas the second geometry has an 800 m acquisition gap depicting the inaccessible areas during the real seismic acquisition (shown in Figure 5.7a). It is assumed that detectors are densely sampled for both cases. The analysis was carried out for the primaries-only wavefield as well as for the full wavefield. First let us see the angle dependent image of this reflector

for the perfect sampling case and for the primaries-only (Figure 5.6b). We observe two effects: severe limitation of the angle-dependent information and the non-uniformity of the amplitude within the available ray-parameter spectrum. This is caused mainly due to the limited spatial aperture as well as the strong lateral-variations because of the salt body. Now, let us look at the full wavefield results shown in Figure 5.6c. We now see the amplitudes are more uniformly distributed within the available spectrum as well as some new angles are found which were not there in the primaries-only wavefield case (especially in the areas shown by the white arrows). This suggests that the multiple reflections balance out the spatial amplitude-variations along the horizon and also provide new angles complementary to the primaries-only reflections.

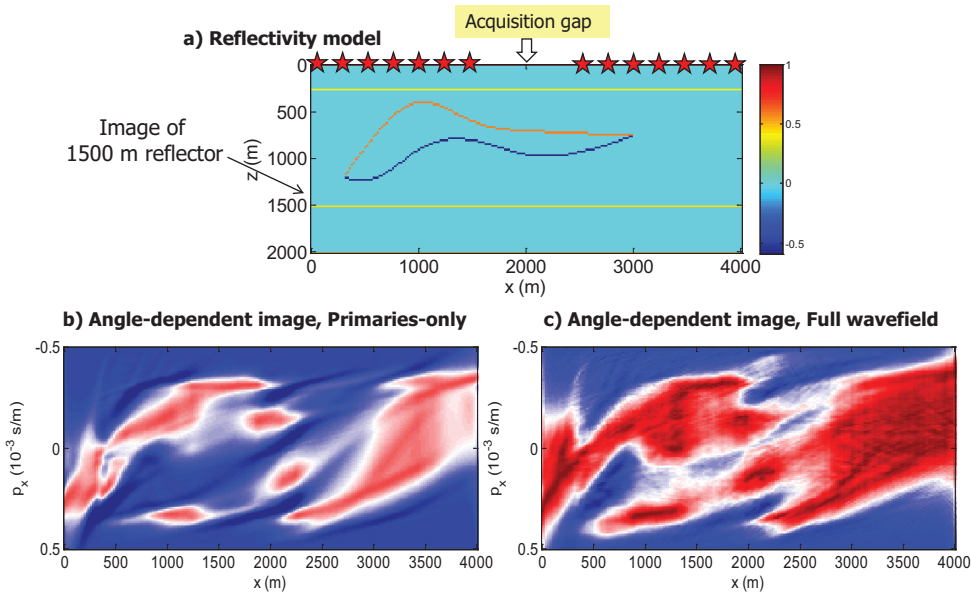


Figure 5.7: same as Figure 5.6, but for the case of a seismic acquisition gap in the source sampling.

Let us now observe the result of the more interesting case where there is an acquisition gap in the source sampling. This experiment is even more impressive for demonstrating the benefits of utilizing multiples. For the primary reflections the result is shown in Figure 5.7b, while the results with all multiples is displayed in Figure 5.7c. The primaries-only result shows a very coarse and limited illumination along the reflector. However, all the multiples that have a bounce at this specific reflector completely infill the angle-space.

Note that this will have major impact for reservoir characterization and velocity analysis, as both process greatly benefit from proper sampling of the illumination angles.

The full wavefield results for this acquisition case resemble the perfect source sampling case closely (Figure 5.6c). Therefore, it is clear that when multiples are used in imaging the traditional belief that sources and detectors should preferably be sampled in a symmetric manner (Vermeer, 2012) becomes outdated.

5.3 Three-dimensional examples

5.3.1 3-D Model example with a ellipsoidal structure

We now provide a 3-D example. The velocity and reflectivity model are shown in Figure 5.8. At about 400 m depth there is an ellipsoidal area with a velocity of 3500 m/s. The 3-D acquisition geometry comprises a densely sampled detector spread and 8 source lines of 2000 m aperture with a sampling interval of 25 m along the x -direction as shown in Figure 5.9. The first four source lines are located from $y = 1000$ m to $y = 1450$ m with a sampling interval of 150 m and the second four source lines are located from $y = 2500$ m to $y = 2950$ m with a sampling interval of 150 m along the y -direction. A target point located at $(x,y,z = 2000,2000,700)$ m in the subsurface has been chosen for the analysis. The source geometry has been designed such that it illuminates the considered target point from large angles in the y -direction when using the primaries-only incident wavefield. We will show that the smaller angles can be obtained by using multiples.

A focal beam analysis for the primaries as well as for the full wavefield was carried out and the results are shown in Figure 5.10. The focal beams at the target level are a function of three variables, i.e., x,y - coordinates and time. Similarly, in the Radon domain, they are function of the p_x,p_y - coordinates and the intercept time. To visualize these results in two dimensions, a slice from such a three dimensional volume is taken. Here, the focal beams and the AVP function will be shown at zero intercept time in a ray-parameter panel (meaning the imaging principle has been applied).

Figures 5.10a, b and c show the detector beam, the source beam and the AVP function for the primaries-only wavefield, respectively. Note that the detector beam shows that all angles are sensed as expected from the densely

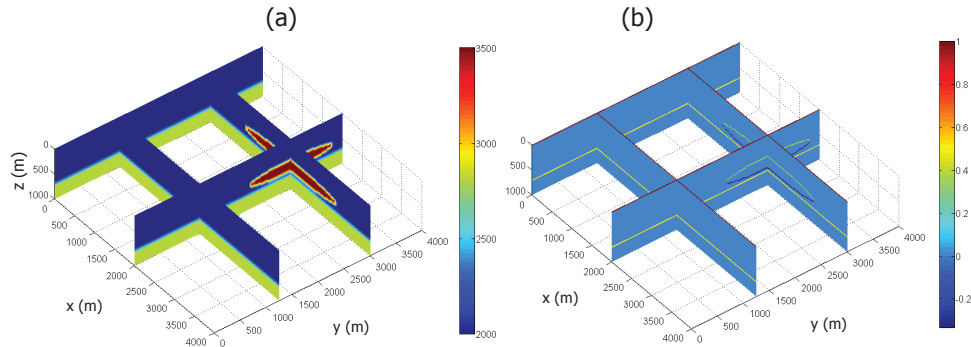


Figure 5.8: a) The 3-D velocity model and b) the 3-D reflectivity model.

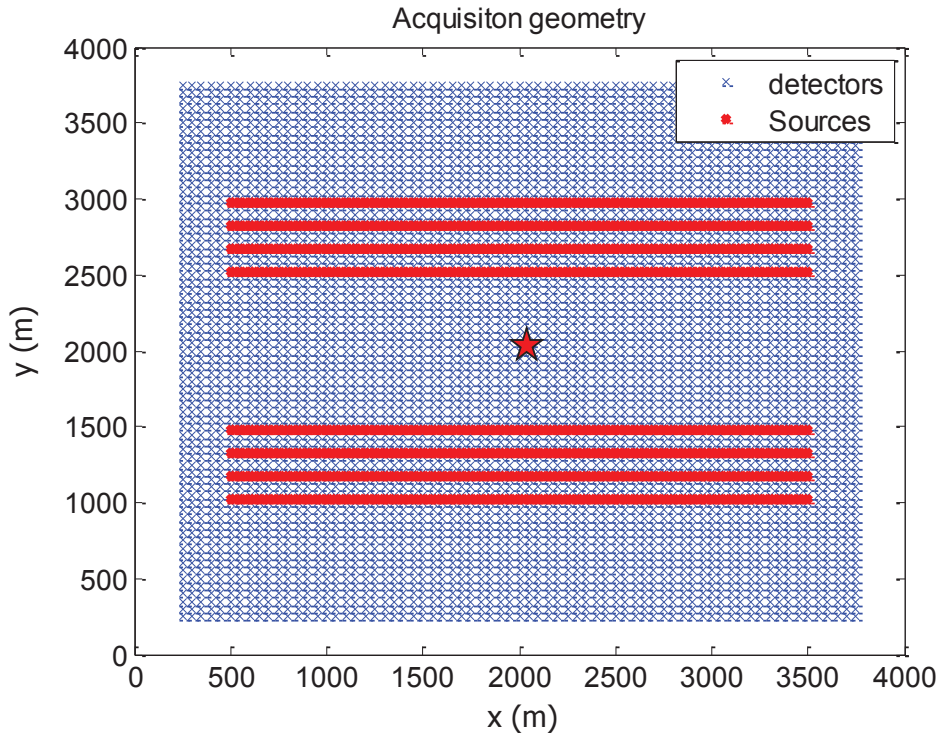


Figure 5.9: 3-D acquisition geometry. The lateral position of the target point at depth 700 m is indicated by the red star.

sampled detector spread. On the other hand, the source beam indeed shows only large illumination angles in p_y . Consequently, the AVP function also

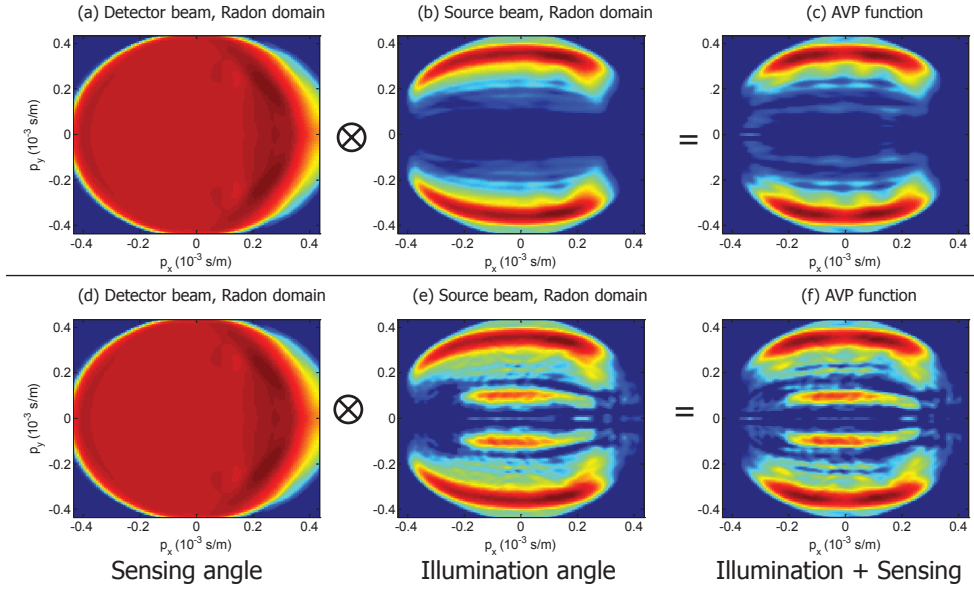


Figure 5.10: The detector beam, the source beam and the AVP function in the Radon domain for the primaries-only wavefield (upper row) and the full wavefield from above (lower row).

shows large reflection angles only. Similarly Figures 5.10d, e and f show the detector beam, the source beam and the AVP function for the full wavefield from above. Note the extension of illumination angles in the source beam and the AVP function towards smaller angles.

We also analysed illumination from below for this example by solving the objective function (4.19). Figures 5.11a, b and c show the result of beams and AVP function for this case. It can be noticed in Figure 5.11b that illumination angles from below are complementary to those from above. The total illumination and reflection angles - from above and from below - are shown in Figures 5.11e and f, respectively.

5.3.2 Impact on angle-dependent reflectivity

The AVP function as presented in the previous section can be used to correct for the angle-dependent amplitude imprint caused by acquisition, overburden and processing. The reflectivity in the ray-parameter domain (\mathbf{R}_k) found in the seismic data is obscured by the acquisition AVP imprint ($\mathbf{\tilde{A}}$),

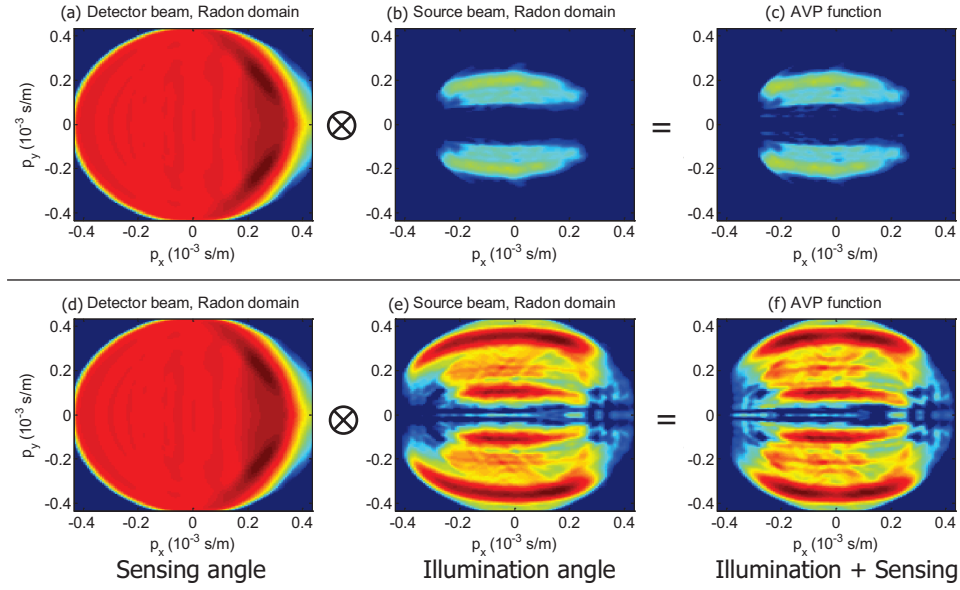


Figure 5.11: The detector beam, the source beam and the AVP function in the Radon domain for the illuminating wavefield from below (upper row) and from the total wavefield (lower row).

which leads to the measured reflectivity $\tilde{\mathbf{A}}\tilde{\mathbf{R}}_k$. The tilde symbol indicates the ray-parameter domain. The focal beam analysis provides a modelled AVP imprint, which represents an estimate $\langle \tilde{\mathbf{A}} \rangle$ of the true acquisition AVP imprint $\tilde{\mathbf{A}}$. Thus, the AVP imprint correction can be applied to the seismic data based on the estimated AVP imprint as follows:

$$\langle \tilde{\mathbf{R}}_k \rangle = \langle \tilde{\mathbf{A}} \rangle^{-1} \tilde{\mathbf{A}}\tilde{\mathbf{R}}_k. \quad (5.1)$$

We computed the true angle-dependent reflectivity for the considered target point in the above example using the known contrast parameters. To estimate this angle-dependent reflectivity curve, the target point should be illuminated from all angles. Figures 5.12a and b show the true reflectivity curve ($\tilde{\mathbf{R}}_k$) with blue lines, the measured reflectivity $\mathbf{A}\mathbf{R}_k$ with dotted black lines and the AVP imprint corrected reflectivity ($\langle \tilde{\mathbf{A}} \rangle^{-1} \tilde{\mathbf{A}}\tilde{\mathbf{R}}_k$) with dotted red lines in the case of using primaries-only wavefield and the full wavefield, respectively. It can be seen that more angle-dependent information can be retrieved with the help of multiples.

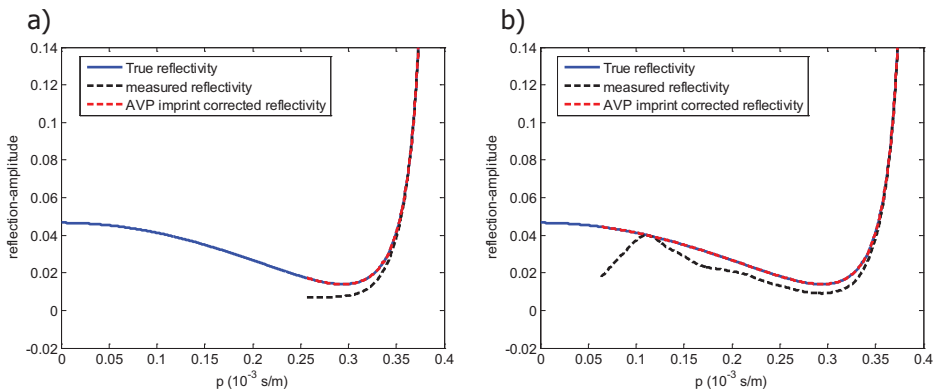


Figure 5.12: a) True reflectivity, measured reflectivity and the AVP imprint-corrected reflectivity for the primaries-only wavefield, and b) same for the full wavefield.

These results have been obtained for the noise free case and considering $\langle \tilde{\mathbf{A}} \rangle = \tilde{\mathbf{A}}$. In the presence of noise, the full-wavefield result is expected to give a more reliable, stable estimate of the reflectivity than the primaries-only wavefield result.

5.3.3 Ziggy model example

The Ziggy model is a Gulf of Mexico salt model developed by SMAART, a former joint venture of BP, BHP Billiton, and Chevron Texaco. The dimensions of the model are 37 km (x) by 40 km (y) by 10 km (z). It is a model with several layers that are more or less flat, and a complex salt structure. A small part of this model with dimensions of 5 km (x) by 5km (y) by 3 km (z) was extracted for an illumination analysis (see Figure 5.13a).

The purpose of this example is to show the influence of an irregularly shaped salt structure on illumination strength (primaries as well as multiples) for subsalt target points by having a perfect source geometry at the surface. The emphasis is on the angle-dependent amplitude information. It is known that this information is highly affected and often irretrievable in subsalt areas. It is, therefore, useful to investigate what information potentially is retrievable with a more or less realistic source geometry and subsequently investigate what extra information can be achievable by using multiples.

A target point located at $(x,y,z) = (2500, 2500, 1660)$ m just below the salt

has been chosen for the illumination analysis. The location of the target point is indicated by the red star in Figures 5.13a and b. The frequency range for which the analysis is carried out is 5 Hz to 30 Hz. The sources are densely sampled with a sampling interval of 25 m in both the inline and the crossline direction. The one-way extrapolation operators, with a length of 29 points, are designed for a maximum propagation angle of 65° using a weighted least square (WLSQ) optimization (Thorbecke et al., 2004). For larger angles, amplitude and phase of the operators go smoothly to zero.

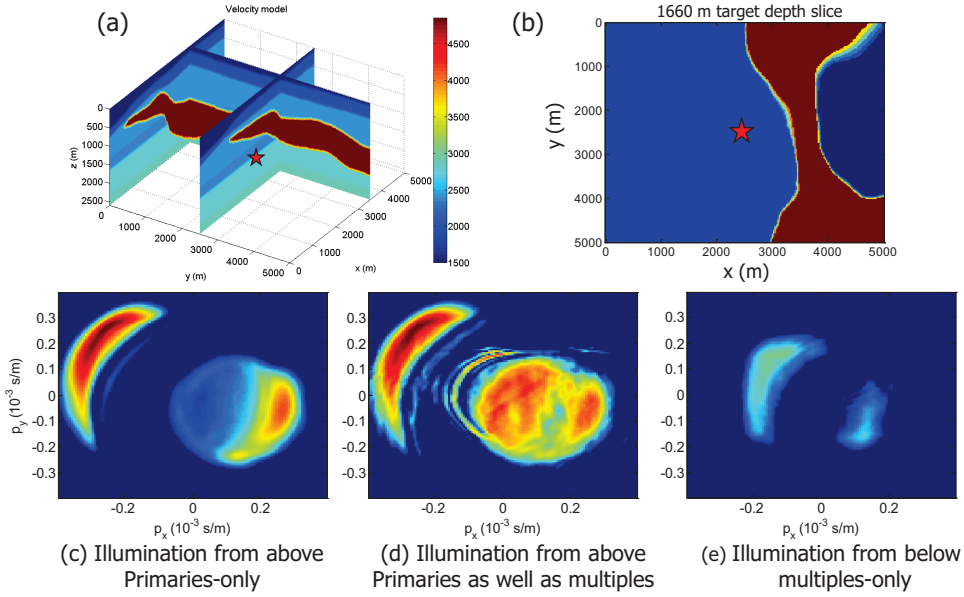


Figure 5.13: a) Part of the Ziggy model (the red star indicates the location of target point), b) the depth slice, where target point is located in the subsurface, c) illumination angles for the primaries-only wavefield, d) illumination angles for the full wavefield incidenting from above, and e) illumination angles for the multiples wavefield incidenting from below.

Equations (4.15) and (4.19) were solved to find the target illumination for the considered target point. Figure 5.13c shows the angles by which the considered target point is illuminated from the perfect source geometry at the surface in the case of using the primaries-only wavefield. Note that this very perfect source distribution provides limited illumination only at the target point in the presence of the salt. It shows a range of angles and azimuths in the bottom right and top left of the figure. The former represents the part of the wavefield that has traveled through the salt. The second high-amplitude

area (top left) represents waves traveling past the edge of salt.

Figure 5.13d shows the extension in illumination angles from above (especially for smaller angles) in the case of using the full wavefield. Similarly, Figure 5.13e provides the angles by which the target point is illuminated from below. The multiples from below are weaker than the multiples from above. Therefore, the amplitude of the illumination angles from below is weaker than the amplitude of the illumination angles from above. In this type of complex scenarios, the multiply scattered wavefield helps considerably to extend the illumination where the singly reflected wavefield fails.

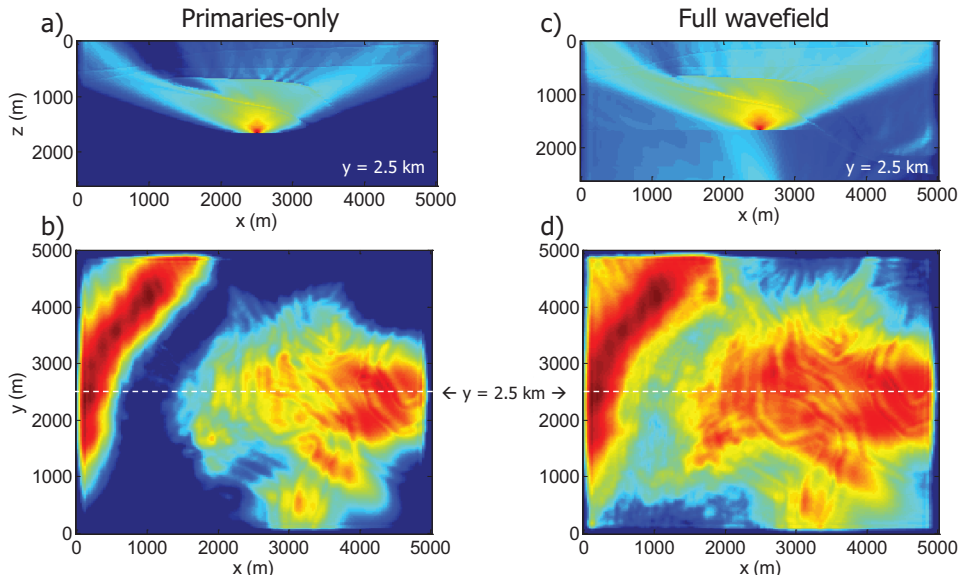


Figure 5.14: 2-D slices of a 3-D energy beam for upward wave propagation from a point diffractor at 1660 m depth, where upper row shows a (x,z) slice at $y = 2.5$ km and the lower row shows the (x,y) slice at the surface. In a) and b) the energy variation caused by the salt body in the case of using the primaries-only wavefield is shown. In c) and d) the same is shown for the full wavefield.

This kind of illumination behavior can be well understood by looking at the energy of the wavefield that propagates upward from a point diffractor at the target point. Figure 5.14 shows how the structure of the salt body causes variations in the energy level at the surface for the primaries-only wavefield as well as for the full wavefield. Figures 5.14a and c show 2-D slices of a 3-D energy beam for upward wave propagation in (x,z) -plane for $y = 2.5$ km. Figures 5.14b and d show a top view energy distribution at the surface along

the (x,y) -plane. A shadow zone can be observed in Figures 5.14a and b from $x = 800$ m to $x = 1800$ m, which corresponds to the loss of illumination angles in Figure 5.13c. The gap in the energy map is partly caused by the angle limitation of the migration operators and it is partly caused by the critical reflection at the base of the salt. However, this gap is partially filled with energy from the multiply scattered wavefield (see Figures 5.14c and d). This explains the extension in illumination angles in Figure 5.13d.

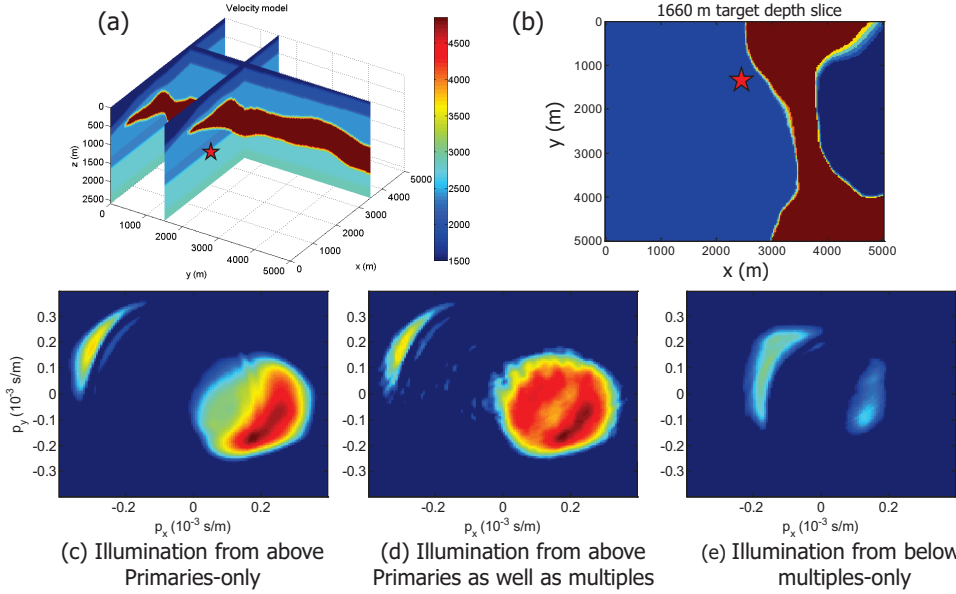


Figure 5.15: a) Part of the Ziggy model (the red star indicates the location of target point), b) the depth slice, where target point is located in the subsurface $(x,y) = (2500,1500)$, c) illumination angles for the primaries-only wavefield, d) illumination angles for the full wavefield incidenting from above, and e) illumination angles for the multiples wavefield incidenting from below.

In the above example, the target point was located in the center of the 1660 m depth slice. Now, we will analyse four more target points at the same depth level but at different lateral locations to see the effect of the subsalt structure on the illumination plot. For all four target points, a 'full 3-D' source geometry is taken (i.e. the sources are densely sampled in both directions). Therefore, the illumination angles are mainly influenced by either the salt structure or the limitation of maximum propagation angle and the aperture. Figures 5.15 to 5.18 show the illumination analysis results for all different target points when using the primaries-only wavefield and the full

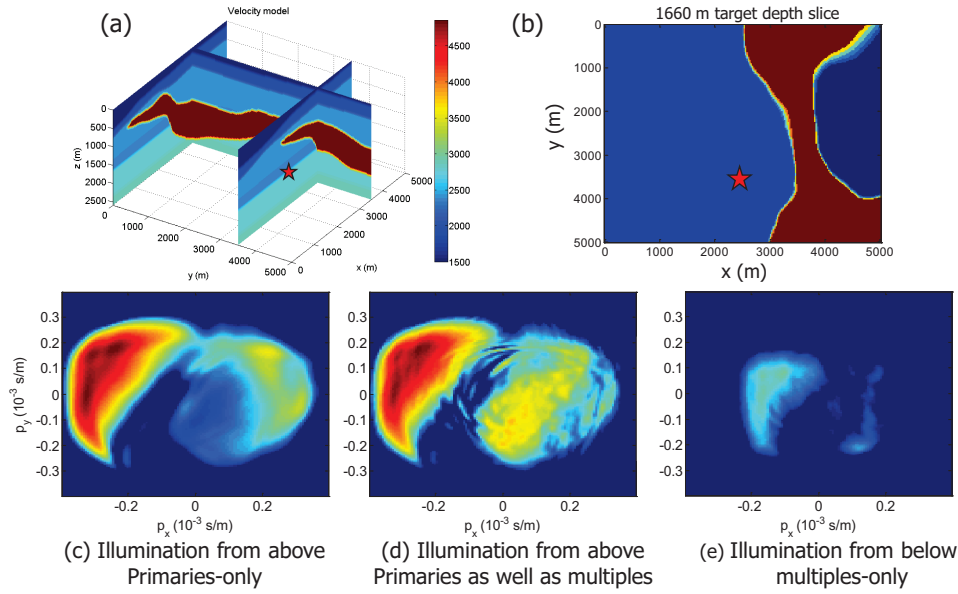


Figure 5.16: a) Part of the Ziggy model (the red star indicates the location of target point), b) the depth slice, where target point is located in the subsurface (x,y) = (2500,3500), c) illumination angles for the primaries-only wavefield, d) illumination angles for the full wavefield incidenting from above, and e) illumination angles for the multiples wavefield incidenting from below.

wavefield, respectively.

Figures 5.15 and 5.16 show the result of the target point which has the same x -coordinate as the centered target point but different y -coordinates (indicated by the red star). Therefore, we see similar effects like two sets of angles and azimuths information, one which has traveled through the salt and the other which has traveled past the edge of salt located in the top left. In both cases, multiples from above as well as from below help to fill the gap in between the two amplitude regions.

Similarly, Figures 5.17 and 5.18 show the result of the target point which has the same y -coordinate as the centered target point but different x -coordinates (indicated by the red star). In Figure 5.17, the target point is located into the salt structure (away from the edge of salt). Therefore, we see illumination angles which have traveled through the salt (see Figure 5.17c). This illumination is enhanced and extended in the case of using the full wavefield (Figures 5.17d and e). On the contrary, the target point is located more towards the

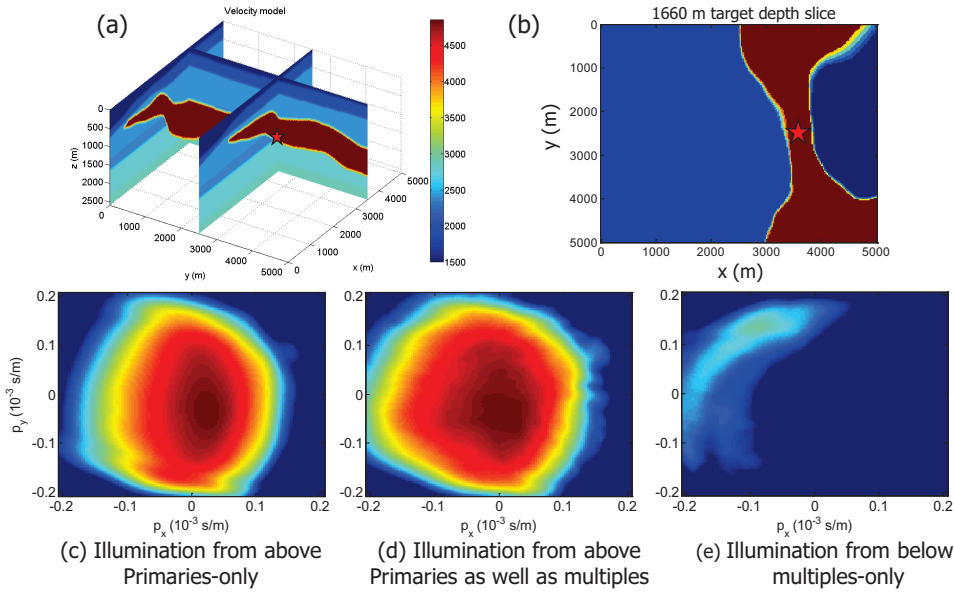


Figure 5.17: a) Part of the Ziggy model (the red star indicates the location of target point), b) the depth slice, where target point is located in the subsurface $(x,y) = (3500,2500)$, c) illumination angles for the primaries-only wavefield, d) illumination angles for the full wavefield incidenting from above, and e) illumination angles for the multiples wavefield incidenting from below.

edge of salt in Figure 5.18, therefore, we see most of the illumination angles which have traveled past the edge of salt only and little through the salt. However, the angles which have traveled through the salt are boosted in the case of using multiples (Figures 5.18d and e).

The above analysis shows that a complex overburden with high velocity contrasts yields limited illumination, even for a perfect source geometry. For the Ziggy model, scattering at the salt boundaries is the main cause. The illumination strongly depend on the location of the target point with respect to the salt body. This is caused by the irregularly shaped salt boundaries. It was shown in the above example that utilizing multiples improves the illumination at the target. Note that in this example 'illumination' can be replaced by 'sensing' if the source distribution at the surface is replaced by a similar detector distribution.

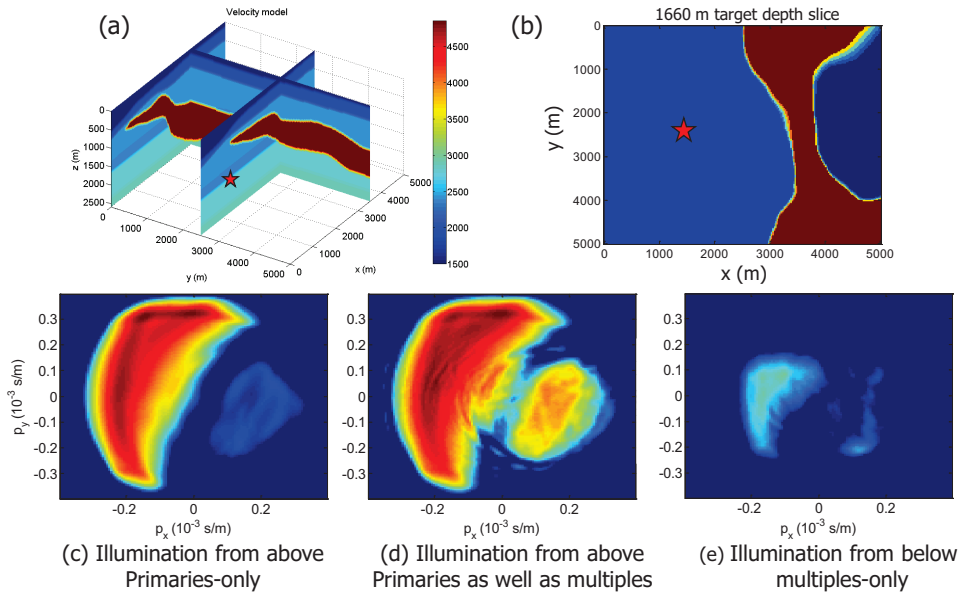


Figure 5.18: a) Part of the Ziggy model (the red star indicates the location of target point), b) the depth slice, where target point is located in the subsurface $(x,y) = (1500,2500)$, c) illumination angles for the primaries-only wavefield, d) illumination angles for the full wavefield incidenting from above, and e) illumination angles for the multiples wavefield incidenting from below.

5.3.4 3-D Model example with a thrust structure

Now we consider another 3-D example with a model having thrust structure. The velocity and the reflectivity model are shown in Figure 5.19. It is a model which has 4 simple layers, where velocity increases with depth and its has a thrust structure in the middle of the model. In this example, we consider an ocean bottom node (OBN) type of geometry in the reciprocal domain: a few sparsely positioned 'sources' at the ocean floor and a dense grid of 'detectors' at the surface. In this case, the measured up-going wavefield at the surface will become the incident wavefield for all surface-related multiples in the data.

The reciprocal OBN geometry shown in Figure 5.20a is taken for the analysis. There are 7 source lines, sparsely sampled with a sampling interval of 600 m in the crossline direction and densely sampled with a sampling interval of 25 m in the inline direction. However, the detectors are densely sampled with a sampling interval of 25 m in both the inline and the crossline direction.

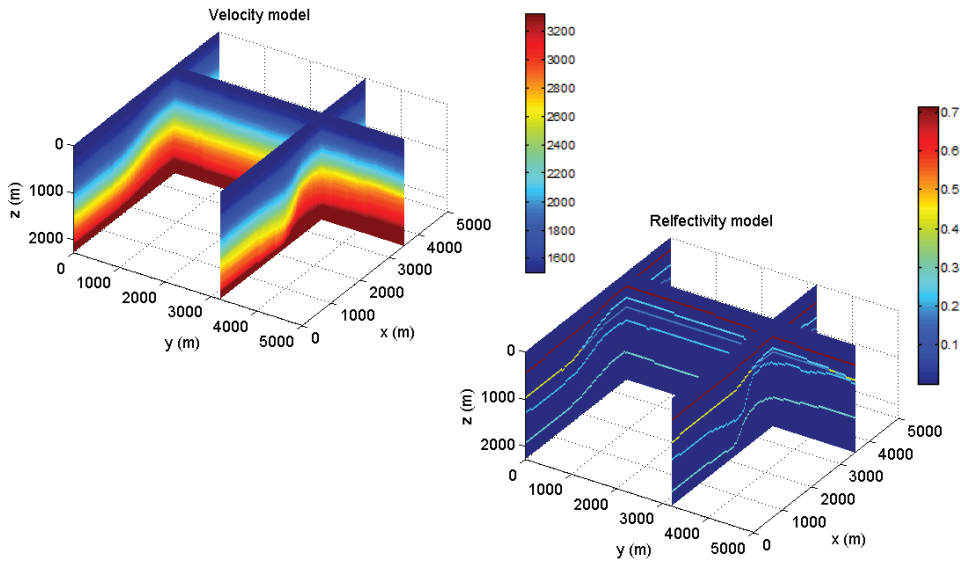


Figure 5.19: The velocity and the reflectivity model taken for the focal beam analysis. The model has a thrust structure in the middle of the subsurface model.

For full-wavefield migration (FWM), it is favorable to have few sources and many densely positioned detectors per source instead of sources and detectors equally distributed (Berkhout and Verschuur, 2014).

The focal beam analysis is performed for two target points: shallow and deep. The location of the target points is shown in Figure 5.20b. The frequency range for which the analysis is carried out is 2 Hz to 30 Hz. Figure 5.21a, b and c show the detector beam, the source beam and their product, the resolution function in the spatial domain for the shallow target point, respectively. As expected from the dense detectors spread, the focusing of detectors is perfect without any aliasing effects (Figure 5.21a). However, the source beam suffers from the sparse sampling interval in the crossline direction, which leads to side lobes as shown in Figure 5.21b. The resolution function is an element by element multiplication of the detector beam and the source beam in the spatial domain. Therefore, the resolution function seems to be perfect even though the source beam suffers from the sparse sampling (Figure 5.21c). Similarly, Figure 5.21d, e and f show the result of the detector beam, the source beam and their element by element product, the AVP function in the Radon domain, respectively. Again, the detector beam shows that all angles are sensed. On the other hand, the source beam shows only

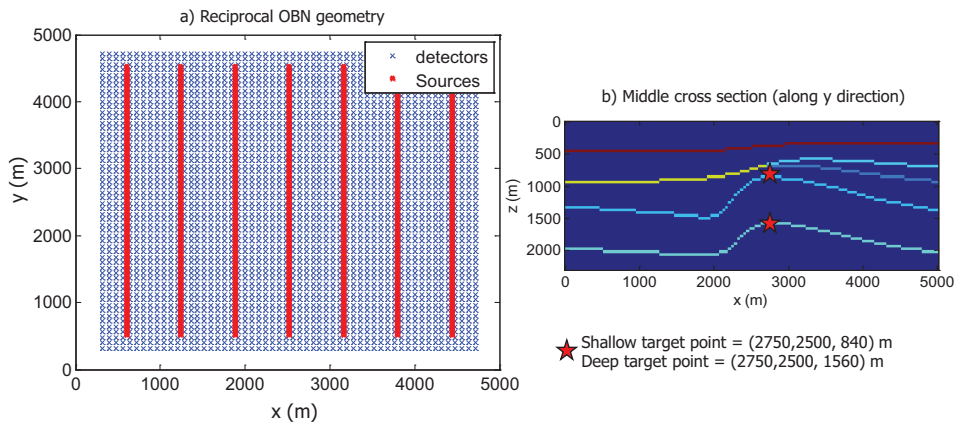


Figure 5.20: a) The OBN geometry in the reciprocal domain, and b) the middle section of the full 3-D reflectivity model in the y -direction. The target points are indicated by a red star with their coordinates.

seven trajectory of illumination angles related to the seven available source lines. Figure 5.21f shows that the AVP function also suffers from the large sampling interval of the source geometry. Therefore, the AVP function is more sensitive to the deficiency of acquisition geometries than the resolution function.

So far, we have seen the results for the primaries-only wavefield. Now, we include multiples to provide the full wavefield results. Figure 5.22 shows the focal beam analysis for the full wavefields. As all the complexity by the multiples is kept at the source side in this case, the detector beam is unchanged. However, multiples provide an additional downgoing source wavefield which reduces the side lobes of the source beam in the spatial domain (Figure 5.22b). In the Radon domain, it becomes clear that multiples provide additional illumination angles, which fill the illumination gap formed by using the primary source wavefields only (Figure 5.22e). There is not much difference in the resolution function, but the gap in the AVP function got filled by the multiples (Figure 5.22f), meaning that angle-dependent reflection properties can be better estimated.

Next, we perform the focal beam analysis for the deeper target point. The maximum opening angle for a target point in the subsurface decreases, when the wavefield travels deeper. Therefore, the deeper target points suffer from the limitation of the angle-aperture. Figure 5.23 shows the result for the deeper target point in case of using the primaries-only wavefield. The detector

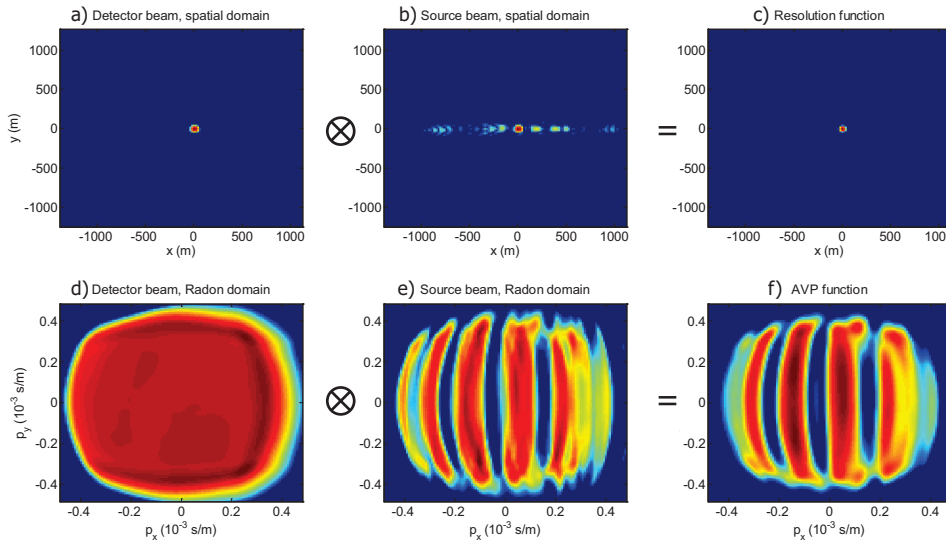


Figure 5.21: a) Focal detector beam in the spatial domain, b) focal source beam in the spatial domain, c) the resolution function for a shallow target point, d) focal detector beam in the Radon domain showing sensing angles, e) focal source beam in the Radon domain showing illumination angles, and f) the AVP function showing illumination-and-sensing angles for the primaries-only wavefield.

beam in the spatial domain (Figure 5.23a) still does not have any side-lobes, but the main lobe is wider than the main lobe of the shallow target detector beam (Figure 5.21a). In the Radon domain, the detector beam shows again that all angles are sensed nicely within the available narrow angle-aperture.

At the source side, the effects of the coarser sampling interval get more severe for the deep target point. E.g., there are now more side-lobes in the spatial domain (Figure 5.23b). In the Radon domain, there are illumination gaps within the available ray-parameter spectrum (Figure 5.23e). The resolution function and the AVP function also suffer from the narrower range of opening angles (Figure 5.23c and f). Now, let us see the result of focal beam analysis for the full wavefield in this deep target point case (Figure 5.24). In this case again, multiples reduce the side lobes in the spatial domain as well as fill the illumination gap in the Radon domain. In both cases, multiples are not only filling the gap but are also boosting the amplitudes of the illumination angles.

So far in all above examples, we have seen that multiples provide extra illu-

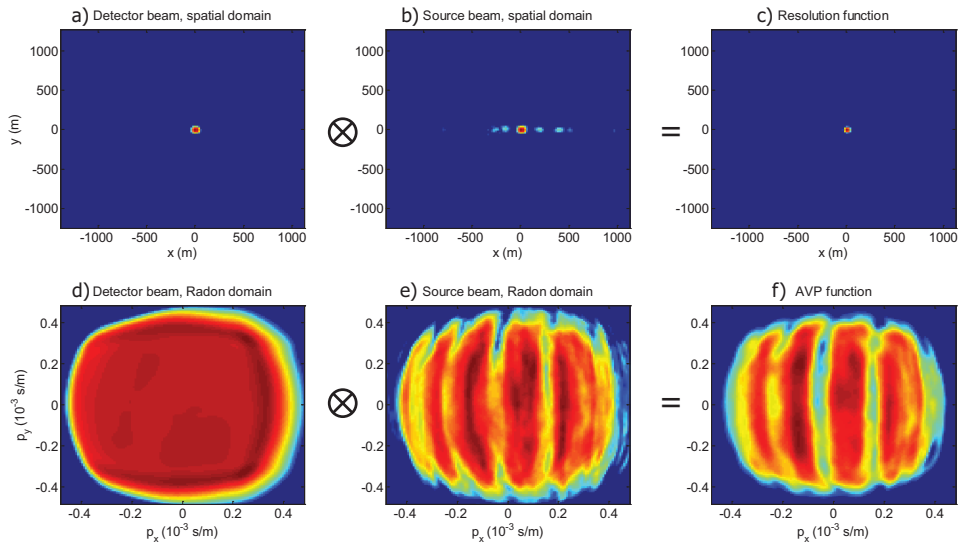


Figure 5.22: Same as figure 5.21, but for the full wavefield.

mination angles for one particular point in the subsurface. However, Figure 5.25 shows that multiple reflections not only provide extra illumination angles at a particular point in the subsurface (Figure 5.25a), but also provide additional image points in the subsurface from one shot record only (Figure 5.25b). It should be noted that the last bounce of each multiple event is considered as the one that is being imaged (indicated by the red circle in the figure).

To illustrate the advantage of utilizing multiples in structural imaging, we provide a 2-D example. A 2-D cross section along the crossline direction of the previous example subsurface model is taken for the illustration of the full-wavefield migration (Figure 5.26a). The detailed theory of the full-wavefield migration can be found in Davydenko et al. (2012); Soni et al. (2012); Davydenko and Verschuur (2013); Berkhout (2014a); Soni et al. (2014); Davydenko and Verschuur (2014).

Along the crossline direction, there are only 7 sources available for the imaging (indicated by the red stars in the Figure 5.26). Therefore, 7 shot-records were modelled using the FWM modelling scheme, where the reflectivity is parametrized as a scalar per grid-point i.e., reflection is angle independent. The modelled data includes all multiple reflections. Next, full wavefield migration is carried out. Figure 5.26b shows the result after first iteration

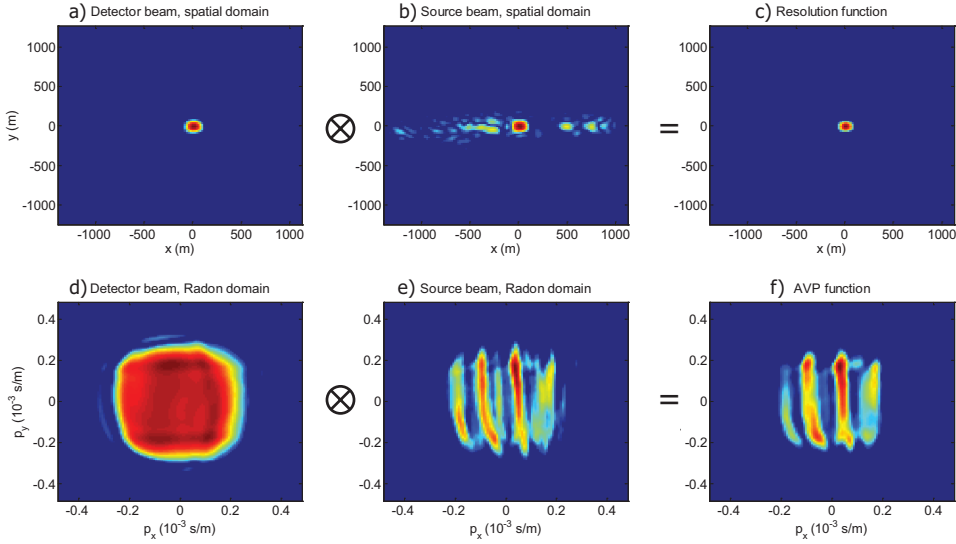


Figure 5.23: a) Focal detector beam in the spatial domain, b) focal source beam in the spatial domain, c) the resolution function for a deep target point, d) focal detector beam in the Radon domain showing sensing angles, e) focal source beam in the Radon domain showing illumination angles, and f) the AVP function showing illumination-and-sensing angles for the primaries-only wavefield.

of FWM (representing conventional migration). In this first iteration, multiples are not correctly explained in the imaging process, which causes strong crosstalk that distorts the estimated reflectivity images.

Now, suppose the multiples have been eliminated from the modelled data using some multiple elimination technique (see e.g. Verschuur et al., 1992; Verschuur, 2006) and then conventional imaging is carried out. The migrated result of the primary reflections only is shown in Figure 5.26c. This estimated reflectivity image looks much better already as multiples have been removed. Therefore, the crosstalk by multiples does not distort the image. However, the sparse sampling of the source geometry produces its imprint on the image and it is impossible to estimate the true reflectivity value of the deep reflectors. This is because the multiples have been *removed* rather than utilized! Next, we *use* the multiples and perform 20 iterations of FWM. The result is shown in Figure 5.26d. A considerable improvement of the estimated reflectivity can be observed compared to the previous two results. There is no source geometry imprint in this case. Note that this means that asymmetric sampling may produce good results, provided information from

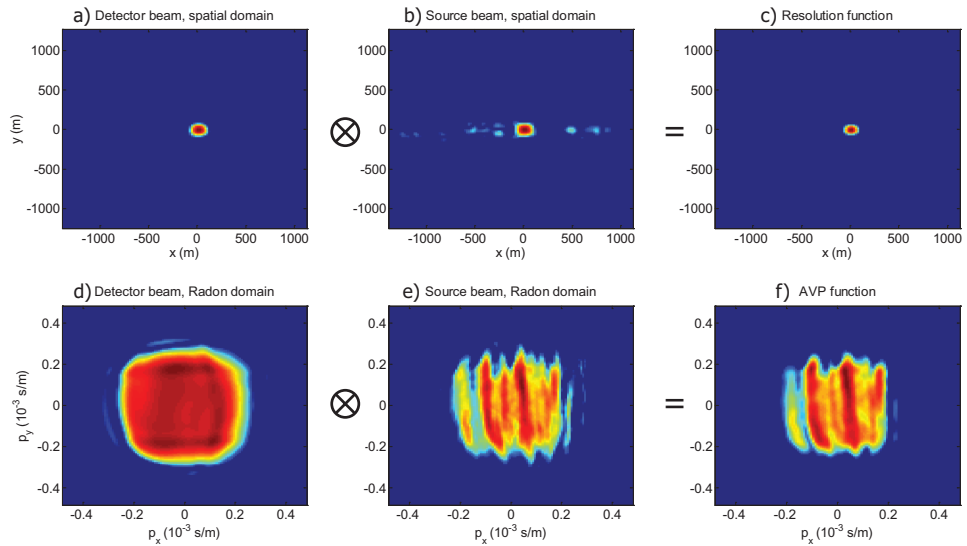


Figure 5.24: Same as figure 5.23, but for the full wavefield.

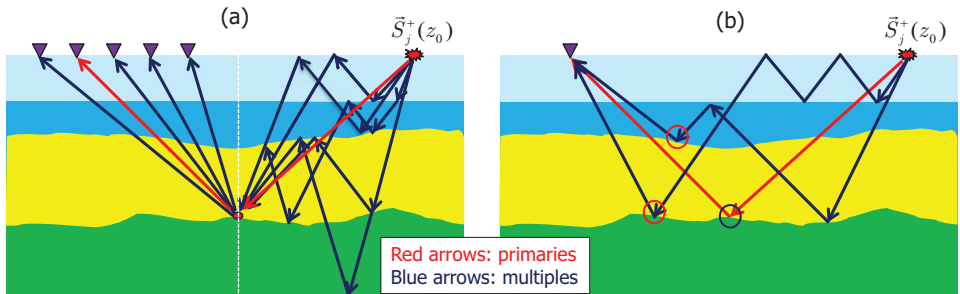


Figure 5.25: a) The schematic representation of extra illumination angles at one target point in the subsurface from one shot record only, and b) shows additional image points from the same shot record. The red circled points are the additional image points.

multiples is utilized.

5.4 Conclusion from this chapter

The main conclusions from this chapter are as follows:

- It was demonstrated that the focal source beam has more energy in the ray-parameter domain (i.e. more illumination angles) when using the full-wavefield for such an analysis than when using the primaries-only wavefield. This supports the theory that multiples imaging uses an areal, down-going source wavefield, which is broadly distributed everywhere in the subsurface model compared to the point sources at the surface used by primaries-only imaging.
- Acquisition geometry design for primaries-only or for the full wavefield leads to different solutions.
- Even if we have a perfect source distribution, primary illumination may be limited due to geology.
- The AVP imprint is always more sensitive to the acquisition geometry than the resolution function.
- The imaging results show that multiples provide an image in primary shadow zones and also help in getting a true-amplitude reflectivity image.
- Finally, the acquisition design and analysis should incorporate both illumination from above and from below.

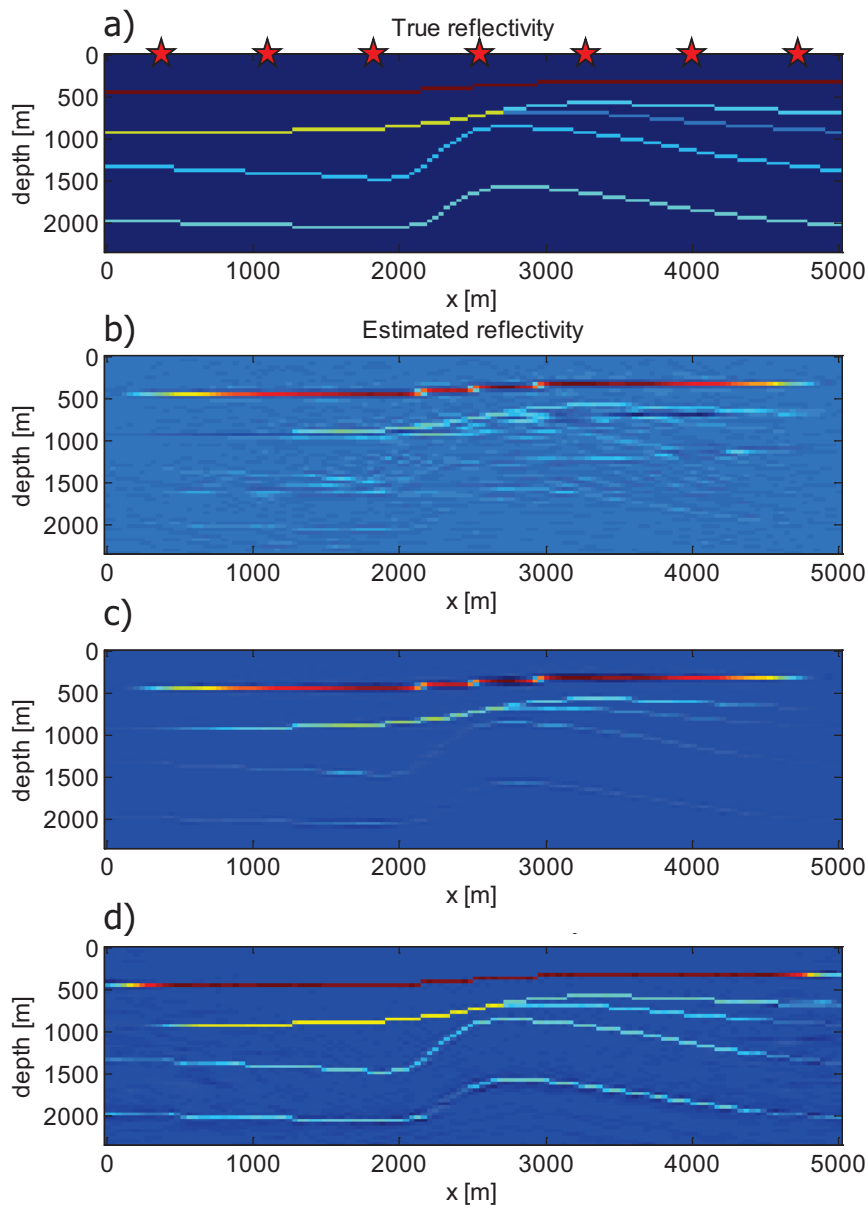


Figure 5.26: a) The true reflectivity image; the 7 sources are indicated by red stars, b) the estimated reflectivity obtained by the primaries-only wavefield migration (the first iteration of FWM), c) the estimated reflectivity obtained by performing the primaries-only wavefield migration on the primaries-only modelled data, and d) the estimated reflectivity obtained after 20 iterations of FWM.

Chapter 6

Marine survey design and analysis ¹

6.1 Introduction

Marine streamer acquisition has improved significantly during the last decade, extending from conventional 3-D marine towed streamer seismic acquisition to the more recent developments such as wide-azimuth, full-azimuth towed streamer, broadband techniques, coil shooting and the emerging technology of simultaneous source acquisition. Despite a tremendous leap in efficiency and wavefield sampling over the last two decades, it is sometimes still difficult to achieve adequate coverage and resolution with marine streamer acquisition. Recent developments have been focusing on improving the sampling of the wavefield especially in the cross-line direction to enhance the resolution and image quality. In streamer seismic, the sampling in the inline direction is much better than in the cross-line direction. Typically, the cross-line CMP spacing is 25 m to 50 m while the inline CMP spacing is 6.25 m to 12.5 m. Also, the maximum offset in the cross-line direction is much smaller than in the inline direction. Both the source and detector sampling intervals are very coarse in the cross line compared to inline. The analysis from Hoffmann et al. (2002) showed that the denser sampling of sources and detectors, in particular in the cross-line direction, can improve the results for towed streamer seismic. Larger cross-line offset improves the focusing of diffractors while denser sampling reduces the acquisition footprint. This is typically achieved by increasing the number of streamers and the number of source tow points in the water. For complex targets, this may involve the costly use of more than

¹This chapter is accepted to *Geophysics* (Kumar et al., 2015). Minor changes were introduced to make the text consistent with the other chapters of this thesis.

one acquisition vessel to achieve wide-azimuth coverage (see e.g., Threadgold et al., 2006; Mandroux et al., 2013; Long, 2010).

An alternative to improve the cross-line sampling is reconstruction using the information of both the pressure wavefield and the cross-line gradients obtained from the cross-line component of a multicomponent streamer (Bunting et al., 2013). On the other hand, multiples can often positively contribute to sampling and illumination if we were able to actively use them in the imaging process. This is possible in a dual-sensor streamer acquisition where the wavefield can be separated into upgoing and downgoing constituents (Whitmore et al., 2010; Lu et al., 2014; Ronholt et al., 2014). We show that multiples can improve the angle range and sampling in the cross-line direction and hence reduce the acquisition footprint.

In this chapter, we extend our existing acquisition analysis technology, the so-called focal beam method further to analyze marine streamer geometries. In this method, a wave-equation-based propagator is used to extrapolate the wavefield from sources and detectors to the subsurface target and a local plane-wave analysis is used at the target level to compute the target illumination and detection. Furthermore, we also include multiples as a valuable signal in our acquisition analysis and show that multiples provide additional information.

We apply the method to the problem of coverage deficiencies that can occur when the survey geometry deviates from the ideal, for example due to feathering. As a result, extra infill lines must be acquired. Day and Rekdal (2006) developed geophysical-based infill specifications to assess the impact of coverage holes on data quality, and thereby set specifications based on permitted levels of data degradation. The current specifications are based on fold of coverage, which is easy to measure during acquisition. However, the effect of coverage holes on data quality after migration is also influenced by geology and survey geometry such that the same fold-based infill specification might lead to very different levels of data degradation for different surveys. In this paper, we implemented a method for infill analysis via the focal beam theory to assess the impact of coverage holes for the primaries as well as the multiples. The infill estimation by Day and Rekdal (2006) was based on time migrated images, but by doing this analysis via focal beams, we extend this work to depth migrated images with or without using multiples.

6.2 Theory

In chapter 2, the focal beam method has been discussed in detail. In this chapter, we extend the focal beam concept further to make it suitable for the analysis of marine streamer geometries. In marine type geometries, the location of the detectors is different for each source (array) position. Such geometries are called non-stationary geometries. In this section, we start with discussing the grid-point responses for non-stationary geometries followed by the concept of the weighted focal beams.

6.2.1 Focal beams for non-stationary geometries

Let us recall the representation of the seismic data in the spatial-frequency domain from equation (2.4) for non-stationary geometries. The seismic response from one template of the total survey can be written as:

$$\mathbf{P}^{[n]}(z_0; z_0) = \mathbf{D}^{[n]}(z_0) \mathbf{W}^-(z_0, z_m) \mathbf{R}^{\cup}(z_m, z_m) \mathbf{W}^+(z_m, z_0) \mathbf{S}^{[n]}(z_0), \quad (6.1)$$

This seismic response for the n^{th} template $\mathbf{P}^{[n]}(z_0; z_0)$ can be further written as superposition of all grid-point responses, as follows:

$$\mathbf{P}^{[n]}(z_0; z_0) = \sum_k \delta_k \mathbf{P}^{[n]}(z_0; z_0), \quad (6.2)$$

where $\delta_k \mathbf{P}^{[n]}(z_0; z_0)$ represents the k^{th} grid-point response and can be expressed as:

$$\delta_k \mathbf{P}^{[n]}(z_0; z_0) = \mathbf{D}^{[n]}(z_0) \mathbf{W}^-(z_0, z_m) \delta_k \mathbf{R}^{\cup}(z_m, z_m) \mathbf{W}^+(z_m, z_0) \mathbf{S}^{[n]}(z_0). \quad (6.3)$$

In order to evaluate the seismic response at the target level, we now need to downward extrapolate the seismic response $\delta_k \mathbf{P}^{[n]}(z_0; z_0)$ for one grid-point at the acquisition level z_0 to the target level z_m . This is achieved by applying additional focusing operators (\mathbf{F}). For the primaries-only case, the image of the grid-point response can then be written as:

$$\delta_k \mathbf{P}^{[n]}(z_m; z_m) = \mathbf{F}(z_m, z_0) \delta_k \mathbf{P}^{[n]}(z_0; z_0) \mathbf{F}(z_0, z_m), \quad (6.4)$$

where matrices \mathbf{F} represent the focusing operators which remove the effect of one way propagation of \mathbf{W}^+ and \mathbf{W}^- . We call this process double focusing

(Berkhout, 1997a). The downward-extrapolated data matrix $\delta_k \mathbf{P}^{[n]}(z_m; z_m)$ is called the grid-point matrix for the n^{th} template. Similar to equation (2.12), the double focusing results can be further written as:

$$\delta_k \mathbf{P}^{[n]}(z_m; z_m) = \left[\mathbf{F}(z_m, z_0) \mathbf{D}^{[n]}(z_0) \vec{W}_k(z_0, z_m) \right] \times \left[\vec{W}_k^\dagger(z_m, z_0) \mathbf{S}^{[n]}(z_0) \mathbf{F}(z_0, z_m) \right], \quad (6.5)$$

$$\delta_k \mathbf{P}^{[n]}(z_m; z_m) = \vec{D}_k^{[n]}(z_m, z_m) \vec{S}_k^{\dagger[n]}(z_m, z_m). \quad (6.6)$$

where $\vec{D}_k^{[n]}(z_m, z_m)$ and $\vec{S}_k^{\dagger[n]}(z_m, z_m)$ represent the focal detector beam (a column vector) and the focal source beam (a row vector) for the k^{th} grid-point by the n^{th} template, respectively. For non-stationary acquisition geometries, focal functions are determined for each stationary part of the survey. Subsequently, the focal functions for the complete survey are obtained by a summation of the focal functions for all stationary parts.

6.2.2 Weighted focal beam concept

According to equation (6.6), the grid-point matrix $\delta_k \mathbf{P}^{[n]}(z_m; z_m)$ can be obtained by the matrix multiplication of the focal detector beam and the focal source beam. In this matrix, the diagonal elements represent the seismic image of the k^{th} grid-point at depth level z_m , the so-called resolution function. These elements are obtained via element by element multiplication of the focal detector beam and the focal source beam. The k^{th} column of this matrix represents the weighted focal detector beam, where the weighting is related to the k^{th} element of the focal source beam $S_{kk}^{[n]}(z_m, z_m)$. Similarly, the k^{th} row of this matrix represents the weighted focal source beam, where the weighting is related to the k^{th} element of the focal detector beam $D_{kk}^{[n]}(z_m, z_m)$. The grid-point matrix is shown in Figure 6.1.

According to the above definition, the weighted focal detector beam (k^{th} column vector of $\delta_k \mathbf{P}^{[n]}(z_m; z_m)$) and the weighted focal source beam (k^{th} row vector of $\delta_k \mathbf{P}^{[n]}(z_m; z_m)$) can be expressed as follows:

$$\delta_k \vec{P}_k^{[n]}(z_m; z_m) = \vec{D}_k^{[n]}(z_m, z_m) S_{kk}^{[n]}(z_m, z_m). \quad (6.7)$$

$$\delta_k \vec{P}_k^{\dagger[n]}(z_m; z_m) = D_{kk}^{[n]}(z_m, z_m) \vec{S}_k^{\dagger[n]}(z_m, z_m). \quad (6.8)$$

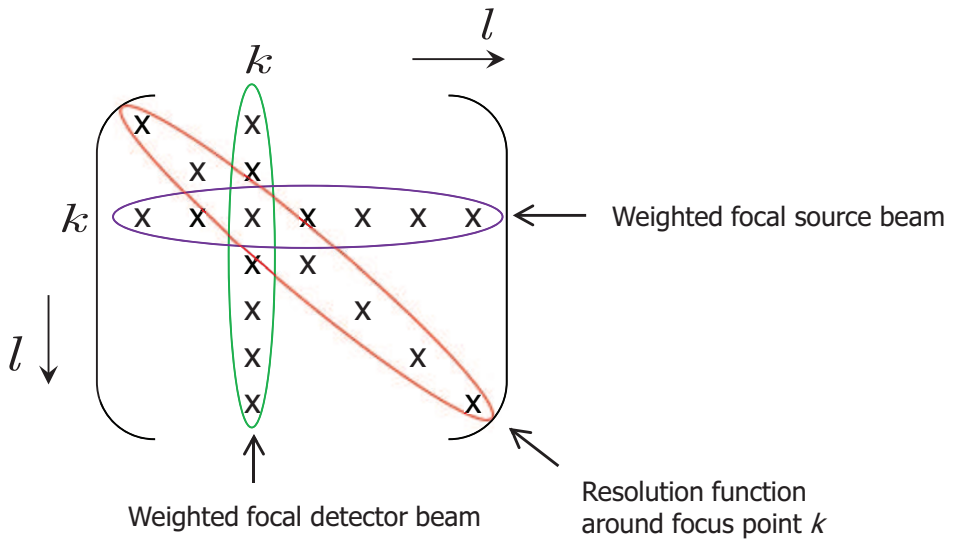


Figure 6.1: The schematic representation of grid-point matrix $\delta_k \mathbf{P}^{[n]}(z_m; z_m)$, showing the position of resolution function as well as the weighted focal detector beam (k^{th} column vector) and the weighted focal source beam (k^{th} row vector). The letter l indicate the lateral location $(x, y)_l$ varying at the target depth level z_m .

The weighted focal detector beam represents the focusing capability of the detector geometry, which strength is weighted by their corresponding sources focused at that target point and vice-versa. This results from the inherent properties of a point diffractor acting as a secondary source and emitting energy in all directions. However, its strength is controlled by the primary sources at the surface by which it is illuminated. Transforming these weighted focal beams to the Radon domain provides illumination-weighted sensing angles (detector side) and sensing-weighted illumination angles (source side), respectively.

Note that all the formulations discussed so far are for the n^{th} template of the total survey. To get a quantitative impression of the total 'illumination capability', the weighted focal source beams for each stationary part should be summed:

$$\delta_k \vec{P}_k^\dagger(z_m; z_m) = \sum_n \delta_k \vec{P}_k^{\dagger[n]}(z_m; z_m). \quad (6.9)$$

Similarly, to see how well the target diffractor can be sensed potentially by all detectors included in the survey, the weighted focal detector beams for each stationary part should be summed:

$$\delta_k \vec{P}_k(z_m; z_m) = \sum_n \delta_k \vec{P}_k^{[n]}(z_m; z_m). \quad (6.10)$$

6.2.3 Extension to multiples

So far, we discussed the focal beams for the primary reflections only. If we include multiples at the source side, the one-way downward propagator $\mathbf{W}^+(z_m, z_0)$ in equation (6.3) should be replaced by the full-wavefield propagator $\mathbf{G}^+(z_m, z_0)$, which includes the effects of all multiples (i.e., propagation as well as reflection and transmission effects). Similarly, if we include multiples at the detector side, one-way upward propagator $\mathbf{W}^-(z_0, z_m)$ in equation (6.3) should be replaced by the full-wavefield propagator $\mathbf{G}^-(z_0, z_m)$. Therefore, in the case of including multiples at the source side, the focal source beam can be expressed as follows, replacing $\vec{W}_k^\dagger(z_m, z_0)$ by $\vec{G}_k^\dagger(z_m, z_0)$ in equation (2.18):

$$\vec{S}_k^{[n]}(z_m) = \vec{G}_k^\dagger(z_m, z_0) \mathbf{S}^{[n]}(z_0) \mathbf{F}(z_0, z_m). \quad (6.11)$$

Similarly, in the case of including multiples at the detector side, the focal detector beam can be expressed as follows, replacing $\vec{W}_k(z_0, z_m)$ by $\vec{G}_k(z_0, z_m)$ in equation (2.17):

$$\vec{D}_k^{[n]}(z_m) = \mathbf{F}(z_m, z_0) \mathbf{D}^{[n]}(z_0) \vec{G}_k(z_0, z_m). \quad (6.12)$$

In these cases, the focusing operator matrices \mathbf{F} should be computed such that they remove the effects of two way propagation of \mathbf{G}^+ and \mathbf{G}^- , respectively. Therefore, the focal beams are computed by a minimization scheme, which is discussed in detail in chapter 4. In this minimization process, the focal beams are computed iteratively and updated using a conjugate gradient scheme.

6.3 Examples

To illustrate the concept of weighted focal beams, we perform focal beam analysis to marine streamer geometries for primaries as well as multiples. The locations of the detectors move with the source position in the case of marine streamer geometries. Hence, the focal beams are computed for each shot position. The source beam for one shot does not have much physical meaning since there is no focusing and the focusing per template is fully determined by the detector geometry. Therefore, the sum of the weighted focal beams over all templates represents the result of the total survey. This sum is shown in the following.

6.3.1 Single source shooting

Weighted focal beams have been computed for an acquisition geometry with the following features (also shown in Figure 6.2):

- shot point interval 50 m;
- 12 streamers per shot, with a length of 1200 m;
- streamer separation 100 m;
- receiver group spacing 25 m;
- 4 sail lines;
- sail-line spacing 600 m;
- near offset gap in the inline direction 50 m.

This geometry is referred as a 1-12 geometry indicating a single source with 12 streamers. The subsurface is a simple 3-D plane-layer model where the velocity increases with depth. The middle cross section ($y = 0$) of the model is shown in Figure 6.3. The analysis is carried out for frequencies ranging from 2 Hz to 30 Hz. A target point laterally located at the center of the total survey area has been chosen for the analysis (indicated by the red star in the Figure 6.2). The target depth is 700 m. In this analysis, the four nearest sail lines were considered, as additional sail lines would not contribute much to the image of the considered target point.

The sum of the weighted focal beams in the spatial domain for the total survey is shown in Figures 6.4a and b. All the results are displayed in a

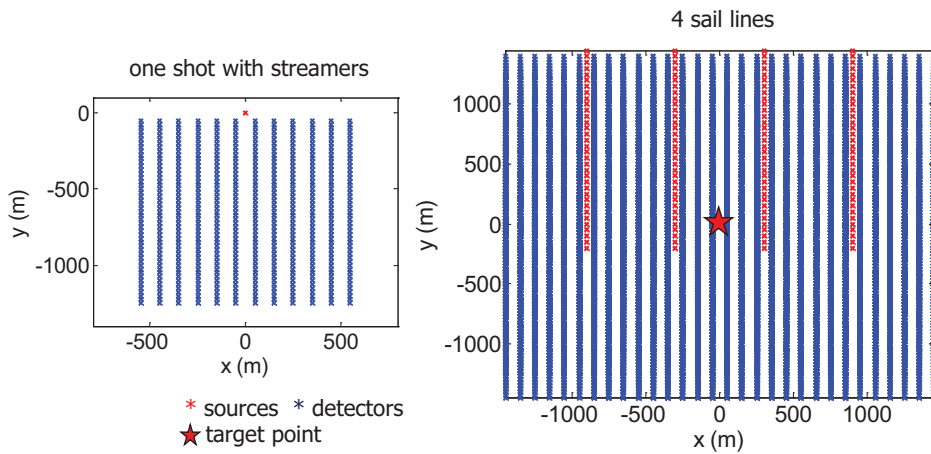


Figure 6.2: 3-D parallel acquisition geometry. On the left, one shot with the corresponding detector lines is shown. On the right, all sail lines and detector lines are shown. The lateral position of the target point is indicated by the red star. Its depth is 700 m.

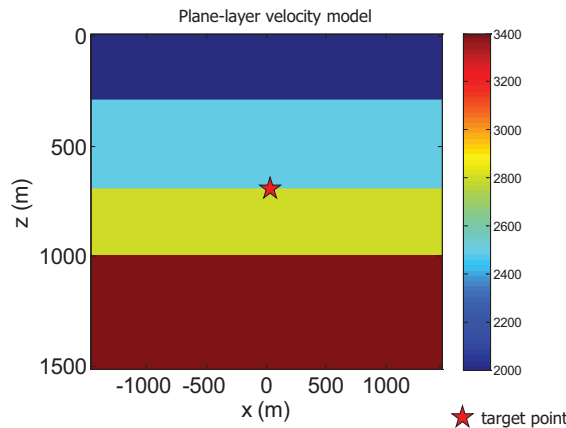


Figure 6.3: A middle cross section of the 3-D plane-layer subsurface model.

linear amplitude scale and the amplitudes are normalized relative to their maximum value, unless mentioned otherwise. The large spacing between the source lines and the detector lines results in spatial aliasing effects. Spatial aliasing causes the side lobes in the cross-line directions that are visible in Figures 6.4a and b. The side-lobe level of the detector beam is much lower than that of the source beam. This can be explained by the dense cross-line

sampling of the detectors compared to the sources. Comparison of the side-lobe positions shows that in case of a smaller line spacing, the side lobes are farther away from the main lobe. They are also weaker in amplitude.

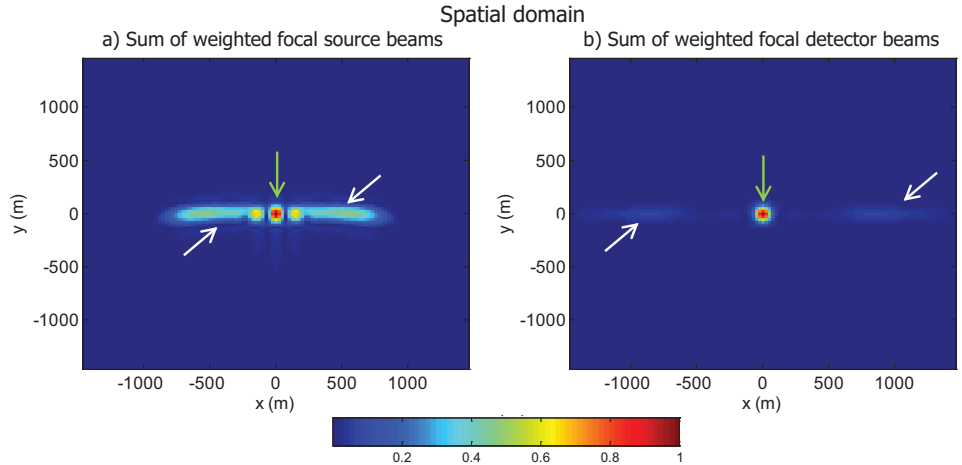


Figure 6.4: a) The sum of weighted focal source beams for the total survey in the spatial domain, showing the focusing capability of the source geometry. b) The sum of weighted focal detector beams in the spatial domain, showing the focusing capability of the detector geometry. The white arrows indicate the side lobes while the green arrows point towards the main lobe.

The angle-dependent information contained in these beams can be obtained by the Radon transformation. Figure 6.5a shows illumination angles weighted by the strength of the focused detectors. Similarly, Figure 6.5b provides sensing angles weighted by the strength of the focused sources. Again, due to the large source-line spacing, we see spatial aliasing effects in this domain as a strong amplitude in the middle of Figure 6.5a. Although the detectors are more densely sampled than the sources along the cross-line direction, we still see vertical stripes related to the detector geometry imprint in Figure 6.5b.

So far, we have seen the results of the focal beam analysis for the primaries-only wavefield. We now present the results for the case that multiples are included. For the model considered above, we now include multiples at the detector side. Therefore, the focal detector beam is recomputed using equation (6.12). Figure 6.6 shows the comparison of the sum of the weighted focal detector beams for the primaries-only wavefield versus the same for the full wavefield. Here, the color scale has been normalized to the maximum value

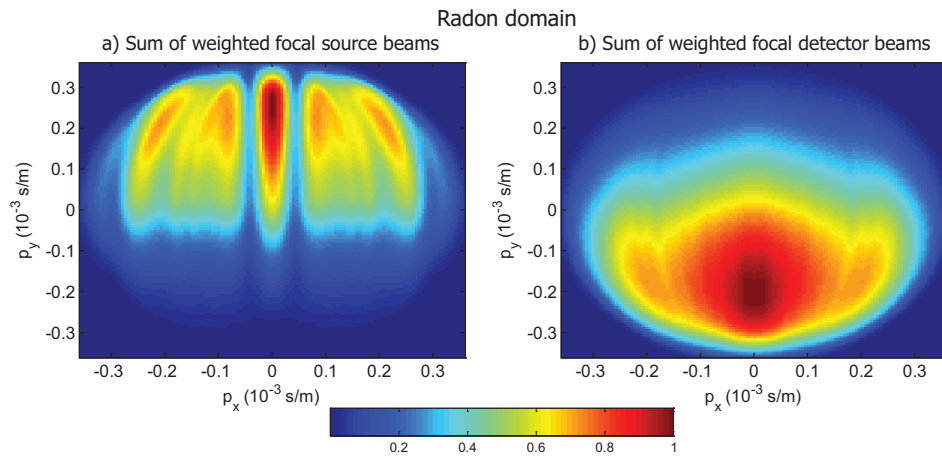


Figure 6.5: a) The sum of weighted focal source beams for the total survey area in the Radon domain, showing illumination angles weighted by their corresponding detectors. b) The sum of weighted focal detector beams in the Radon domain, showing sensing angles weighted by their corresponding sources.

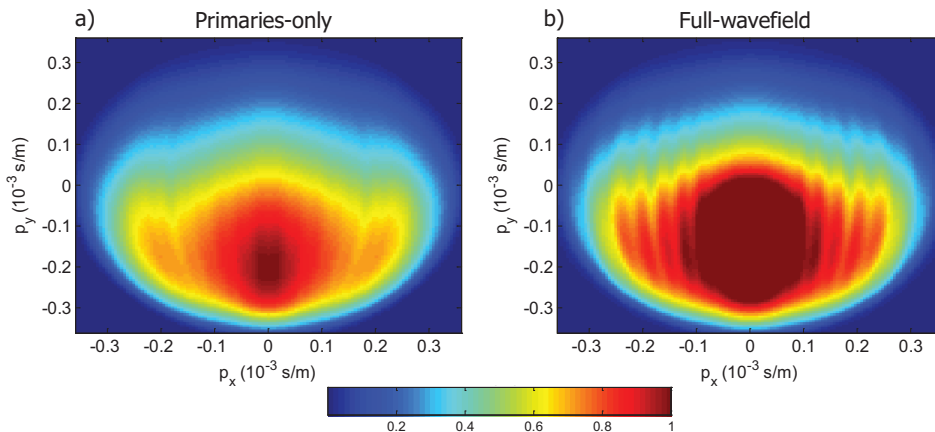


Figure 6.6: Comparison of a) the sum of the weighted focal detector beams for the primaries-only wavefield versus b) for the full wavefield.

of the primaries-only plot. In this simple layered model multiples clearly provide additional signal at the target location, mainly in the smaller angle range.

6.3.2 Flip-flop shooting

We now provide an example of flip-flop shooting for the same subsurface model. The geometry comprises of a dual source separated by 50 m along the cross-line direction, the number of streamers is the same as for single source shooting. This geometry is shown in Figure 6.7.

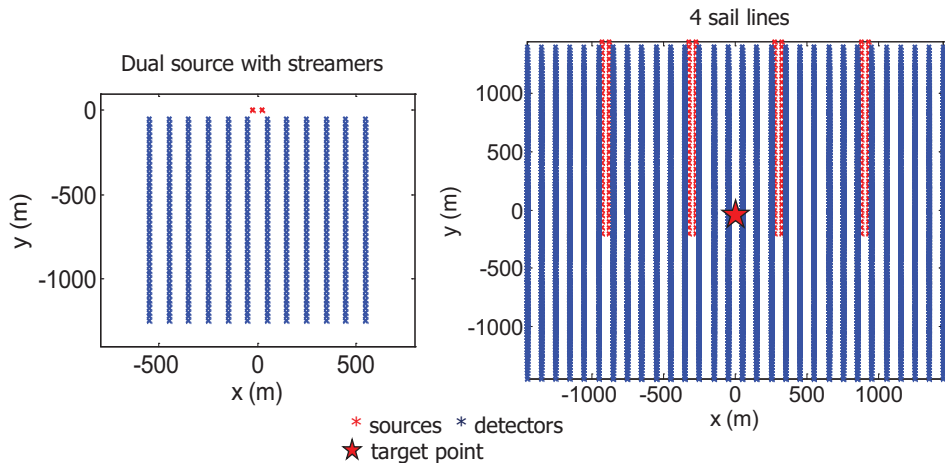


Figure 6.7: 3-D parallel acquisition geometry with dual source configuration. On the left, dual sources with their corresponding detector lines are shown. On the right, all sail lines and detector lines are shown. The lateral location of the target point is in the middle of the total survey, indicated by the red star, and its depth is 700 m.

This geometry is referred as 2-12 geometry indicating a geometry having dual sources and 12 streamers. The results of the focal beam analysis for the primaries-only wavefield are shown in Figure 6.8. Note that the position of the side lobes is the same as in the previous example for the weighted focal source beam (compare Figure 6.8a and 6.4a). It is determined by the distance between the sail lines, which is the same for these two geometries. However, the 1-12 geometry has stronger side lobes than the 2-12 geometry, which means that flip-flop shooting reduces the side-lobe level. Also, there is less spread of energy that can be observed in the Radon domain of the weighted focal source beam (see Figure 6.8b compared to Figure 6.5a). At the detector side, there is little difference in the weighted focal detector beam results between the two geometries. This is because the number of streamers and the streamer separation are the same for both.

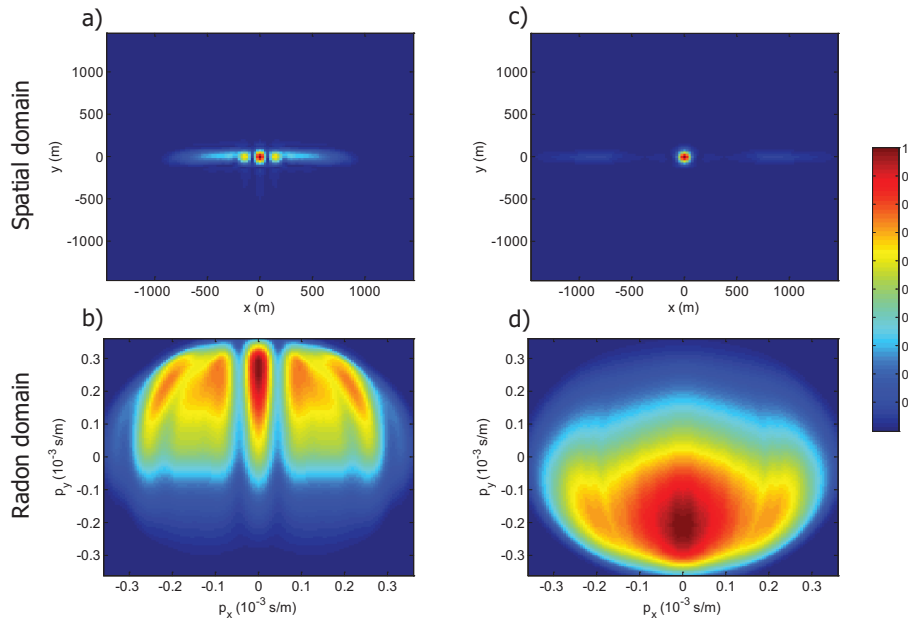


Figure 6.8: Analysis of the 2-12 flip-flop shooting geometry. a) The sum of weighted focal source beams for the total survey in the spatial domain, b) same in the Radon domain, c) the sum of weighted focal detector beams for the total survey in the spatial domain and d) same in the Radon domain.

Now, we show the diagonal elements of the grid-point matrix (Figure 6.1) obtained by the 1-12 geometry and 2-12 geometry respectively. The diagonal elements represent the seismic image of the point diffractor at the target depth level, the so-called resolution function. The resolution functions are shown in Figure 6.9 in a logarithmic (dB) scale. The main lobes show little differences between these two geometries, as these are determined by the maximum aperture which is the same for both geometries. However, the side lobes for the 2-12 geometry (Figure 6.9b) are reduced significantly compared to the 1-12 geometry (Figure 6.9a). This is attributable to the decrease of the crossline CMP spacing for the 2-12 geometry. The use of flip-flop shooting improves the weighted source beam as well as the resolution function.

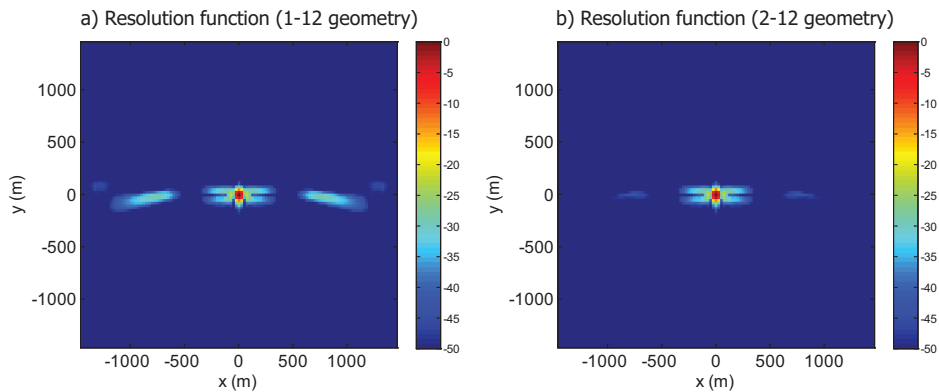


Figure 6.9: Resolution function for two geometries: a) single source shooting (1-12), and b) flip-flop shooting (2-12).

6.4 Application to infill analysis

During marine streamer acquisition, coverage deficiencies may occur when the sail-line geometry deviates from the ideal, for example due to feathering or due to obstacles such as production platforms. As a result, extra 'infill' lines must be acquired (Vermeer, 2012). Brink et al. (2004) describe a method for assessing the effect of coverage holes at specified target horizons using simulated reflection amplitudes based on a 3D subsurface model. Day and Rekdal (2006) developed geophysical-based infill specifications to assess the impact of coverage holes on data quality, and thereby set suitable specifications based on permitted levels of data degradation. This degradation is measured in terms of maximum amplitude loss and time shift in the presence of deficient coverage relative to a reference model with full coverage. Infill specifications can be determined by defining the maximum permissible data degradation as measured by these attributes.

Coverage holes in common mid-point (CMP) position may be simulated either at the center of the sail lines (to mimic center streamer split due to jet-flow effects) or at the sail-line boundaries (to mimic coverage holes due to changes in feather between adjacent sail lines). In a simple plane-layer model, removing more and more streamers from two adjacent sail lines creates bigger and bigger holes in the CMP positions as explained in Figure 6.10. These are termed as CMP holes or coverage holes. Such holes are responsible for amplitude losses as well as time shifts in the final migrated image. The latter

quantities are the basis of infill analysis according to Day and Rekdal (2006). Figure 6.10 also shows how the angle range decreases with the increase in hole size for a centrally located target point.

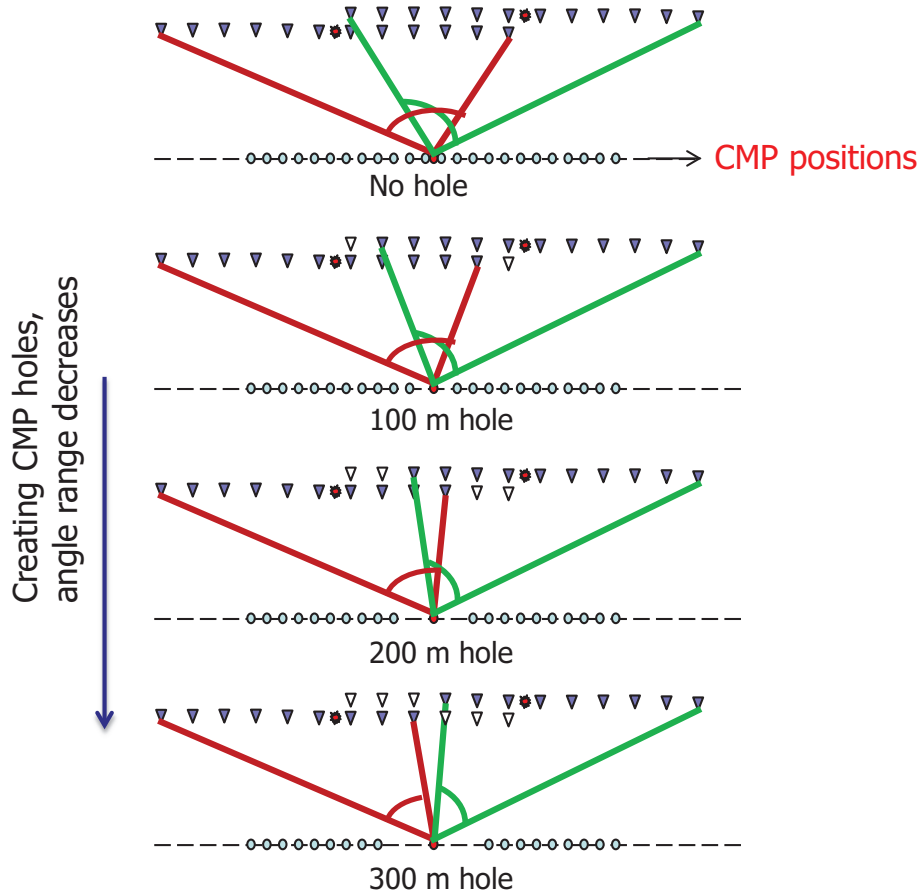


Figure 6.10: Schematic representation of creating coverage holes in the crossline direction by repeatedly removing streamers from adjacent sail-lines. Green triangles denote the position of streamers that are kept in the spread, and white triangles denote the streamers that are omitted in the analysis to simulate a hole due to feathering. It also shows a decrease in the angle range for a target point located centrally.

Because the focal beams are computed for a particular target point in the depth domain, we can perform infill analysis in the ray-parameter domain using focal beams for the same target point. For each coverage hole size, the focal beams can be computed and analyzed. Let us now analyze the effects of coverage holes on the sum of the weighted focal detector beams for the

same model discussed in the example section. Figure 6.11 shows the analysis result for the primaries as well as for the full wavefield. In the left column of Figure 6.11, it is clear that with increasing hole size, increasing gaps occur in the middle for low values of $|p_x|$, resulting in decreased illumination for these angles. However, the effect is somewhat mitigated if multiples are considered in the imaging process (right column of Figure 6.11).

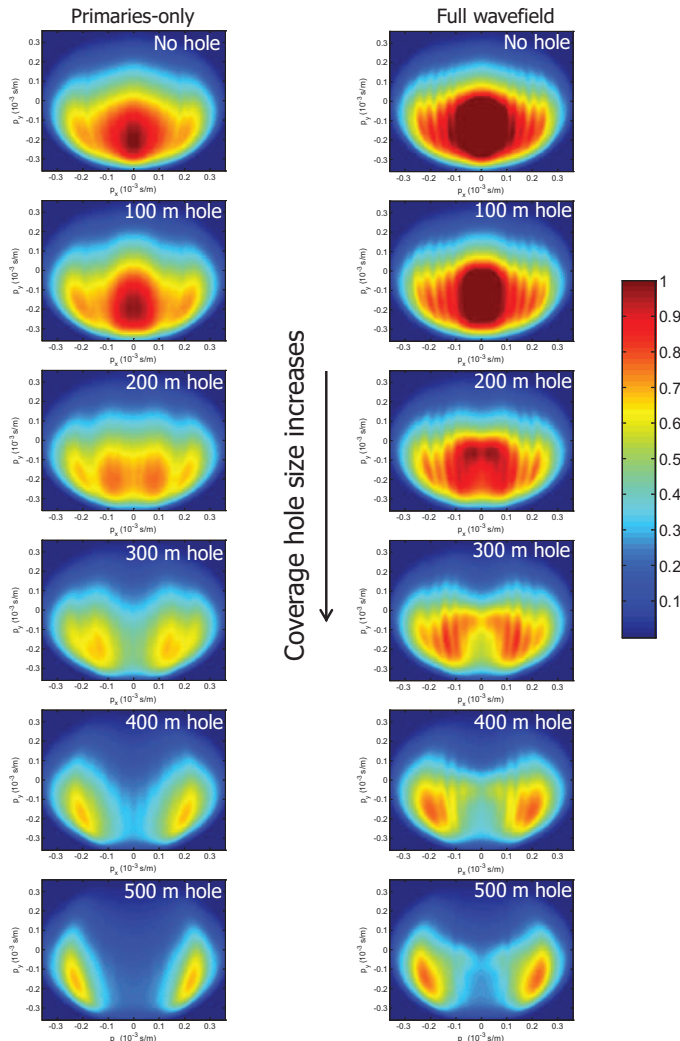


Figure 6.11: Comparison of a) the sum of the weighted focal detector beams for primaries-only wavefield versus b) same for the full wavefield.

If we sum the amplitudes along the p_y direction, the amplitude drop along the p_x direction for holes of different sizes can be obtained. Figure 6.12 shows the relative amplitude drop with respect to the reference level (no hole case with using full wavefield) for the primaries as well as for the full wavefield. In both figures a negative amplitude change indicates that the amplitude along the p_x direction with a coverage hole has a lower level than the the reference level. It is to be noted that the reference level is the same for both the primaries as well as the full wavefield. It can be seen clearly that the primaries-only amplitude decays more for the same hole size compared to the full wavefield case.

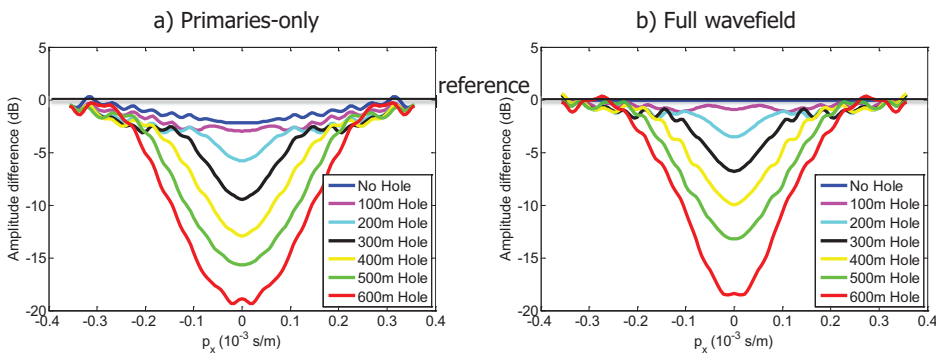


Figure 6.12: Amplitude drop in dB as a function of inline ray parameter for several hole sizes. a) for primaries-only wavefield, and b) for the full wavefield case. The reference line is shown in black.

Summation of the weighted focal beams over all ray-parameter components yields an angle-averaged diffraction amplitude. This is the amplitude as is produced by 3D prestack depth migration of a point-diffractor response. The relative drop in the angle-averaged diffraction amplitude with respect to the coverage hole size is shown in Figure 6.13. In this figure, the reference level of the full wavefield has been taken for both cases. Therefore, the gain of 1.7 dB in the amplitude for the full wavefield over the primaries-only wavefield can be seen clearly. The relative drop in the amplitude is the same for the primaries-only and the full-wavefield cases.

The results shown in Figures 6.11 to 6.13 were modelled assuming zero coverage case, when holes were completely empty. But in practice, there can be some coverage in the hole. Therefore, partial coverage can be simulated by appropriate weighting of the contributions from the coverage hole. The

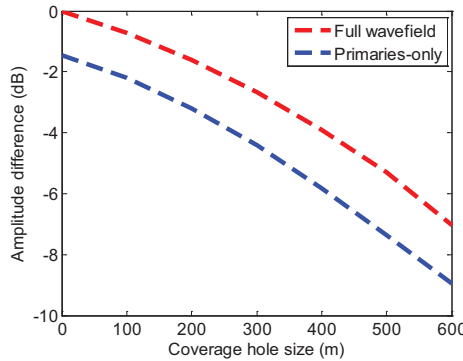


Figure 6.13: The relative drop in the angle-averaged diffraction amplitude with respect to the coverage hole size after summing all ray-parameter components.

amplitude loss is calculated for several partial coverage levels. Figure 6.14 summarizes the amplitude loss as a function of hole size and the coverage percentage within the hole for a single target point when using the primaries-only wavefield. Relationships of this form are used to define infill specifications.

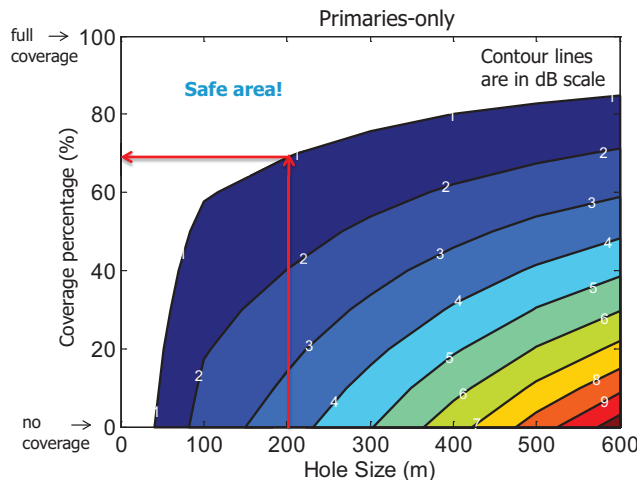


Figure 6.14: Amplitude loss (in dB) as a function of hole size and percentage coverage within the hole for a single target point when using the primaries-only wavefield.

Infill specifications can be defined based on the amplitude loss as shown in Figure 6.14. In order to satisfy the data quality requirements, the amplitude loss due to coverage holes should be chosen such that it does not exceed

a certain value, e.g., 1 dB. In that case, the area above the 1 dB contour in Figure 6.14 could be considered as safe area, i.e., the data degradation remains acceptable. For example, 200 m hole size can be allowed if there is a coverage of 70 percent in the hole as indicated by the red lines.

Next, we show the similar contour plot for the full wavefield case (Figure 6.15). It is to be noted that the safe area has been increased now when using multiples. For example, 200 m hole size can be allowed now with only 45 percent coverage in the hole compared to 70 percent in the case of the primaries-only wavefield. Therefore, the infill criteria can be relaxed by including multiples. With this analysis, we have defined a way to derive a criterion for the acceptable gap size in seismic data using the focal beams.

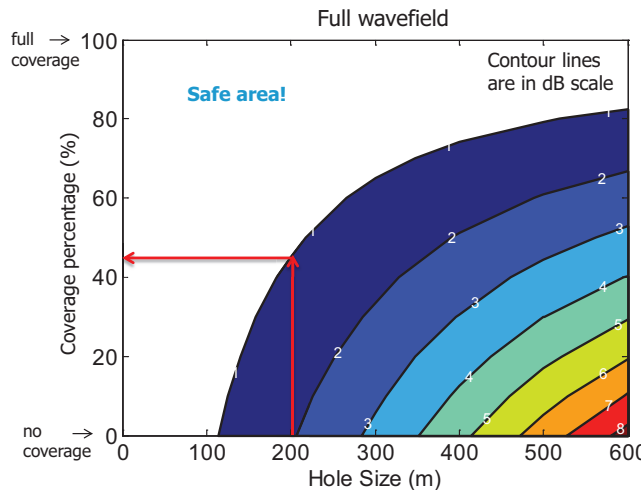


Figure 6.15: Amplitude loss (in dB) as a function of hole size and percentage coverage within the hole for a single target point when using the full wavefield.

6.5 Discussion

We propose the (weighted) focal beam concept to analyze marine streamer geometries, where all multiples can be used effectively to enhance the resolution and the illumination. The main purpose of this chapter is to demonstrate the huge potential of the focal beam method to analyze any type of geometry with and without using all multiples. Also, we demonstrated that this method can be used to assess the impact of coverage holes on angle-

dependent properties contained in the acquired seismic data.

The analysis results shown in this chapter were for a plane layer subsurface model. However, for more complex models, they are still qualitatively valid and useful. Also, these analyses were carried out for a single shallow target point. However, the analysis can be carried out for any target point located in the subsurface, depending upon the requirement.

We do realize that our analysis can be improved further. The reflectivity model used for the modeling of multiples in the recursive full wavefield modeling method was angle-independent. The method can be extended to include angle-dependent reflectivity to improve the amplitude aspects of the multiples, in particular the amplitude-versus-offset information. So far, illumination and sensing angles correspond to P-waves only. However, the method can be extended to include multi-component seismic data, meaning incorporating converted waves as well (see chapter 6, Soni, 2014). There are many benefits of using converted waves, e.g., shear waves are not affected by gas clouds, while gas causes strong transmission losses for pressure waves. Granli et al. (1999) show that a better image quality is obtained when using converted waves in situations where gas clouds form a problem. This would require an extension of the full-wavefield modeling engine to the elastic case.

6.6 Conclusion from this chapter

The focal beam concept can be used to assess the illumination capabilities of a marine acquisition geometry in the depth domain. In addition to calculating the resolution function, the concept of weighted focal source and detector beams allows to conveniently assess the angular aperture available for a specific acquisition configuration at the considered depth point. Potential illumination problems under complex overburden, or possible acquisition footprint patterns can be quickly identified in this domain. By extending the problem to two-way propagation, multiples are included in the analysis, considering the response for the increasing popular case that multiples are not suppressed but rather actively used in the imaging process.

We addressed one particular application, namely the identification of coverage holes arising from deviations to the nominal survey geometry, for example due to feathering. The advantage of the proposed method is that coverage holes can be assessed in the depth domain so that infill criteria can be adapted to the local geology. This leads to more accurate infill decisions compared

to CMP-based criteria. In addition, the effect of multiples in coverage holes can be assessed. Considering multiples in the imaging process may lead to more relaxed thresholds for infill shooting.

Chapter 7

Conclusions and recommendations

Utilization of multiples is considered to be the next big step forward in seismic imaging and reservoir characterization. Multiples in the measured data are generally considered to be noise in the seismic industry. However, the multiples provide an extra source of illumination in the area where the primary wavefield may have failed to illuminate. In this PhD research, I have looked upon the seismic acquisition geometry design and analysis via the focal beam method, when multiples are used as a signal in the seismic imaging. The traditional focal beam method has been extended to take into account the illumination properties of all multiples as well. In this chapter, I will discuss the conclusions and recommendations based on this research and future research plans.

7.1 Conclusions

This section summarizes the main conclusions based on the research presented in this thesis. In chapter two, the traditional focal beam concept has been reviewed thoroughly and applied to the Schoonebeek oil field geometry. The underlying principles of the focal beam concept are as follows:

- The prestack migration results are directly determined by the properties of the two focal beams (source and detector). The beam properties are directly determined by the source and detector geometry.
- Element by element multiplication of the source and detector beam in the space-frequency domain yields the resolution function, which is

the image of a unit point diffractor. It is used to measure the spatial resolution at the target and to quantify the effects of spatial aliasing.

- Similarly, an element by element multiplication of the source and detector beam in the Radon-frequency domain yields the AVP function, which is the angle-dependent image of one reflection point on an angle-independent reflector. It is used to show how the angle-dependent reflectivity is sampled at the target by a particular acquisition geometry.
- A major advantage of the focal beam analysis is the separation in source and detector geometry, allowing imaging deficiencies to be traced towards their origin, i.e., source and/or detector distributions.
- The Radon transformation of a focal source beam shows the angle-dependent illumination of a subsurface point. Similarly, the Radon transformation of a focal detector beam shows the angle-dependent sensing of a subsurface point.
- The resolution function is relatively less sensitive to acquisition geometries than the AVP function. This means that in terms of resolution, source and detector geometry complement each other. Hence, decisions about acquisition geometries should not be based on resolution functions only.
- In the case of the AVP function, the source and detector geometry do not complement each other. An accurate AVP functions would require the Radon transform of both the source and detector beam to have a constant amplitude spectrum. That implies high acquisition effort: the complete sampling of both sources and detectors.

In chapters 3, 4 and 5, the existing so-called focal beam method for primary reflections was expanded to include all multiples as well. The grid-point response is formulated such that all the complex wave propagation paths by the multiples are kept on the source side, leading to a complex full illuminating wavefield. As a result of the complex illuminating wavefields involved, the focal beam needs to be computed by a minimization scheme. A distinction is made between illumination from above and illumination from below: both directions of illumination contain information about the local reflectivity. Illumination from above as well as from below by multiply reflected wavefields reveals information at angles that may not be present in illumination by primary reflections. This feature can be exploited in the acquisition design. It may either lead to a much improved image of the subsurface for the same acquisition geometry, or to a more cost-effective acquisition geometry for the

same image quality. This extended analysis via focal beams can be used for effective survey design, assuming that multiples will be used in imaging and reservoir characterization on a routine basis. The main benefits of using multiples in the focal beam are the following:

- The focal source beam has more energy in the ray-parameter domain (i.e. more illumination angles) when using the full-wavefield than when using the primaries-only wavefield. This supports the theory that multiples imaging uses an areal, down-going source wavefield, which is broadly distributed everywhere in the subsurface compared to the point sources at the surface used by primaries-only imaging.
- Acquisition geometry design for primaries-only or for the full wavefield leads to different solutions.
- Even if we have a perfect source distribution, primary illumination may be limited due to geology.
- The imaging results show that multiples provide an image in primary shadow zones and also help in getting a true-amplitude reflectivity image.
- Finally, the acquisition design and analysis should incorporate both illumination from above and from below.

In chapter 6, we introduced the concept of the weighted focal beam for non-stationary geometries, e.g., marine geometries. In addition to calculating the resolution function, the concept of weighted focal source and detector beams allows to conveniently assess the angular aperture available for a specific acquisition configuration at the considered depth point. We addressed one particular application, namely the identification of coverage holes arising from deviations to the nominal survey geometry, for example due to feathering. The advantage of the proposed method is that coverage holes can be assessed in the depth domain so that infill criteria can be adapted to the local geology. This leads to more accurate infill decisions compared to CMP-based criteria. In addition, the effect of multiples in coverage holes can be assessed. Considering multiples in the imaging process may lead to more relaxed thresholds for infill shooting.

7.2 Recommendations

- The theory presented in this thesis is a forward analysis of any proposed acquisition geometry in terms of resolution and angle-dependent properties at any subsurface point. For example, our analysis can provide the extra information to be obtained from all multiples, when they are *used* rather than *removed* for a particular acquisition geometry on a given subsurface model. The next step could be a backward analysis to find an optimum acquisition geometry which provides the required illumination from above as well as from below, utilizing all multiples. Also, the method has the ability to assess separately detector and source contributions. Therefore, this feature could be exploited in a design algorithm to arrive at an optimized acquisition configuration.
- We do realize that our forward focal beam analysis can be improved further. The reflectivity model used in this thesis for the modeling of multiples in the recursive full wavefield modeling method was angle-independent. The method can be extended to include angle-dependent reflectivity to improve the amplitude aspects of the multiples, in particular the amplitude-versus-offset information.
- So far, illumination and sensing angles correspond to P-waves only. However, the method can be extended to include multi-component seismic data, meaning incorporating converted waves as well (see chapter 6, Soni, 2014). There are many benefits of using converted waves, e.g., shear waves are less affected by gas clouds, while gas causes strong transmission losses for pressure waves. Granli et al. (1999) show that a better image quality is obtained when using converted waves in situations where gas clouds form a problem. This would require an extension of the full-wavefield modeling engine to the elastic case.

Appendix A

The phase shift operator (\mathbf{W})

The starting point for deriving acoustic forward wavefield extrapolation operators is the one-way version of the acoustic Rayleigh II integral (Wapenaar and Berkhout, 1989):

$$P^+(x, y, z_1; \omega) = 2 \iint \left[\frac{\partial G^+(x, y, z_1; x', y', z' = z_0; \omega)}{\partial z'} \frac{1}{\rho(x', y', z_0)} P^+(x', y', z_0; \omega) \right] dx' dy', \quad (\text{A.1})$$

where P^+ represents the downgoing part of the total acoustic pressure wavefield, G^+ is the downgoing part of the Green's wavefield at (x, y, z_1) due to a monopole source at $(x', y', z' = z_0)$, ω is the radial frequency, and ρ is the mass density. The above equation states that a pressure wavefield at depth level z_1 can be synthesized by a dipole distribution at depth level z_0 weighted with the downgoing part of the pressure wavefield at depth level z_0 (see Figure A.1). The formulation of upgoing wavefields is similar.

For the special situation that the medium between z_0 and z_1 is laterally invariant, the Green's wavefields are a function of the distances $x - x'$ and $y - y'$ only, hence for this situation equation (A.1) can be written as a spatial convolution integral (Berkhout, 1982):

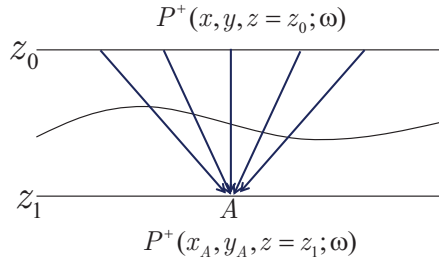


Figure A.1: Acoustic forward wavefield extrapolation: Downward extrapolation of down-going waves (one way Rayleigh II integral).

$$\begin{aligned}
 & P^+(x, y, z_1; \omega) \\
 &= \frac{2}{\rho(z_0)} \iint \left[\frac{\partial G^+(x - x', y - y', z_1; 0, 0, z' = z_0; \omega)}{\partial z'} P^+(x', y', z_0; \omega) \right] dx' dy', \tag{A.2}
 \end{aligned}$$

or

$$P^+(x, y, z_1; \omega) = W^+(x, y; z_1, z_0; \omega) * P^+(x, y, z_0; \omega), \tag{A.3}$$

with

$$W^+(x, y; z_1, z_0; \omega) = \frac{2}{\rho(z_0)} \frac{\partial G^+(x, y, z_1; 0, 0, z = z_0; \omega)}{\partial z}. \tag{A.4}$$

The convolution in the space-frequency domain of equation (A.3) corresponds to multiplication in the wavenumber-frequency domain as follows:

$$\tilde{P}^+(k_x, k_y, z_1; \omega) = \tilde{W}^+(k_x, k_y; z_1, z_0; \omega) \tilde{P}^+(k_x, k_y, z_0; \omega), \tag{A.5}$$

where

$$\tilde{W}^+(k_x, k_y; z_1, z_0; \omega) = \frac{2}{\rho(z_0)} \frac{\partial \tilde{G}^+(k_x, k_y, z_1; 0, 0, z = z_0; \omega)}{\partial z}. \tag{A.6}$$

Here, k_x and k_y are the lateral wavenumbers. The tilde symbol (\sim) indicates the wavenumber-frequency domain.

Now, considering vertically invariant media between depth levels z_0 and z_1 , the free space Green's wavefield between the source point \vec{r}_0 and the observation point \vec{r}_1 in the space-time domain, is given by:

$$g(\vec{r}_1, \vec{r}_0, t) = \frac{\rho}{4\pi} \frac{\delta(t - \frac{\Delta r}{c})}{\Delta r}, \quad (\text{A.7})$$

where c is the propagation velocity and Δr is the distance $|\vec{r}_1 - \vec{r}_0|$. Applying Fourier transformation, the Green's wavefield in the space-frequency domain can be expressed as follows:

$$G(\vec{r}_1, \vec{r}_0, \omega) = \frac{\rho}{4\pi} \frac{e^{-jk\Delta r}}{\Delta r}, \quad (\text{A.8})$$

with

$$k = \frac{\omega}{c}. \quad (\text{A.9})$$

In the wavenumber-frequency domain, the Green's wavefield is written as:

$$\tilde{G}(k_x, k_y, z_1; x_0, y_0, z_0, \omega) = \rho e^{j(k_x x_0 + k_y y_0)} \frac{e^{-jk_z \Delta z}}{2jk_z}, \quad (\text{A.10})$$

with

$$k_z^2 = k^2 - k_x^2 - k_y^2. \quad (\text{A.11})$$

where Δz is the vertical depth step $|z_1 - z_0|$. By taking $x_0 = 0$ and $y_0 = 0$, we may substitute this free space solution into equation (A.6), yielding:

$$\begin{aligned} \tilde{W}^+(k_x, k_y; z_1, z_0; \omega) &= 2 \frac{\partial}{\partial z_0} \left[\frac{e^{-jk_z \Delta z}}{2jk_z} \right] \\ &= e^{-jk_z \Delta z}. \end{aligned} \quad (\text{A.12})$$

This is the well known phase-shift operator (Gazdag, 1978). For a homogenous layer, wavefield extrapolation from one depth level to another can be achieved simply by multiplication with a phase shift term in the wavenumber-frequency domain. However, to allow lateral medium variations, we have to go back to the space-frequency domain and carry out this operation as space-variant convolution. A benefit of the computation of $W^+(x, y; z_1, z_0; \omega)$ via the $k_x k_y$ -domain (A.12) rather than directly (A.4) is that operator aliasing can be easily avoided.

Appendix B

Expression for \mathbf{G} in terms of \mathbf{W} , \mathbf{R} and \mathbf{T}

In chapters 4 and 5, we discussed that the one-way propagation operator (\mathbf{W}) is replaced by the full wavefield propagation operator (\mathbf{G}) in the case of including all multiples in the grid-point responses. The one-way propagation operator \mathbf{W} is the discretized version (in matrix notation) of the W discussed in the previous appendix (A). In this appendix, we will derive the full expression of \mathbf{G} for a simple two layer reflector model (see Figure B.1). We will show that the operator \mathbf{G} is a complex non-linear combination of one-way operator \mathbf{W} , reflection operator \mathbf{R} and transmission operator \mathbf{T} .

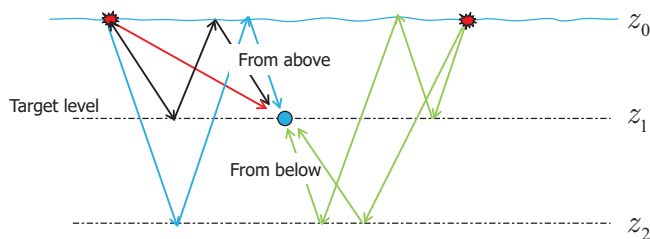


Figure B.1: A cartoon showing the illuminating wavefield from above as well as from below at depth level z_1 by the sources located at the surface z_0 .

For the model shown in Figure B.1, we are going to derive the expression for the illuminating wavefield at depth level z_1 by sources located at the

surface z_0 for the primaries-only wavefield as well as for the full wavefield, respectively. The primaries-only illuminating wavefield at depth level z_1 can be expressed as follows (indicated by the red arrow in Figure B.1):

$$\mathbf{P}_0^+(z_1; z_0) = \mathbf{W}^+(z_1, z_0) \mathbf{S}^+(z_0). \quad (\text{B.1})$$

Next, we use the primary reflections from depth level z_1 after reflecting at surface z_0 as an illuminating wavefield from above to depth level z_1 . It is indicated by the black arrows in Figure B.1. This wavefield can be expressed as:

$$\mathbf{P}_1^+(z_1; z_0) = \mathbf{W}^+(z_1, z_0) \mathbf{R}^\cap(z_0, z_0) \mathbf{W}^-(z_0, z_1) \mathbf{R}^\cup(z_1, z_1) \mathbf{W}^+(z_1, z_0) \mathbf{S}^+(z_0). \quad (\text{B.2})$$

Similarly, the primary reflections from depth level z_2 after reflecting at the surface can also be used as an illuminating wavefield from above (indicated by the blue arrows in Figure B.1):

$$\mathbf{P}_2^+(z_1; z_0) = \mathbf{W}^+(z_1, z_0) \mathbf{R}^\cap(z_0, z_0) \underline{\mathbf{W}}^-(z_0, z_2) \mathbf{R}^\cup(z_2, z_2) \underline{\mathbf{W}}^+(z_2, z_0) \mathbf{S}^+(z_0). \quad (\text{B.3})$$

where $\underline{\mathbf{W}}$ represents generalized one-way propagation operators which include transmission effects as well, given by:

$$\begin{aligned} \underline{\mathbf{W}}^-(z_0, z_2) &= \mathbf{W}^-(z_0, z_1) \mathbf{T}^-(z_1, z_1) \mathbf{W}^-(z_1, z_2), \\ \underline{\mathbf{W}}^+(z_2, z_0) &= \mathbf{W}^+(z_2, z_1) \mathbf{T}^+(z_1, z_1) \mathbf{W}^+(z_1, z_0). \end{aligned} \quad (\text{B.4})$$

Similarly, there are many orders of internal multiple-reflection terms which illuminate target level z_1 from above. The full illuminating wavefield from above can be written as superposition of all these terms:

$$\mathbf{P}_{full}^+(z_1; z_0) = [\mathbf{P}_0^+(z_1; z_0) + \mathbf{P}_1^+(z_1; z_0) + \mathbf{P}_2^+(z_1; z_0) + \dots], \quad (\text{B.5})$$

or

$$\begin{aligned} \mathbf{P}_{full}^+(z_1; z_0) &= \mathbf{W}^+(z_1, z_0) \left[\mathbf{I} + \mathbf{R}^\cap(z_0, z_0) \mathbf{W}^-(z_0, z_1) \mathbf{R}^\cup(z_1, z_1) \mathbf{W}^+(z_1, z_0) \right. \\ &\quad \left. + \mathbf{R}^\cap(z_0, z_0) \underline{\mathbf{W}}^-(z_0, z_2) \mathbf{R}^\cup(z_2, z_2) \underline{\mathbf{W}}^+(z_2, z_0) + \dots \right] \mathbf{S}^+(z_0). \end{aligned} \quad (\text{B.6})$$

In short, the above expression (B.6) can be expressed as:

$$\mathbf{P}_{full}^+(z_1; z_0) = \mathbf{G}^+(z_1, z_0) \mathbf{S}^+(z_0), \quad (B.7)$$

where

$$\begin{aligned} & \mathbf{G}^+(z_1, z_0) \\ &= \mathbf{W}^+(z_1, z_0) \left[\begin{array}{l} \mathbf{I} + \mathbf{R}^\cap(z_0, z_0) \mathbf{W}^-(z_0, z_1) \mathbf{R}^\cup(z_1, z_1) \mathbf{W}^+(z_1, z_0) \\ + \mathbf{R}^\cap(z_0, z_0) \mathbf{W}^-(z_0, z_2) \mathbf{R}^\cup(z_2, z_2) \mathbf{W}^+(z_2, z_0) + \dots \end{array} \right]. \end{aligned} \quad (B.8)$$

This is the expression of the full wavefield propagator for this simple layered model only. Similarly, the expression for the full illuminating wavefield from below can be derived. It can be seen from the expression (B.8) that the full wavefield propagator (\mathbf{G}) becomes a complex non-linear propagator including the effects of \mathbf{W} , \mathbf{R} and \mathbf{T} . Therefore, the inverse of \mathbf{G} can not be expressed as its complex conjugate: $\mathbf{G}^{-1} \neq \mathbf{G}^H$. As a consequence, the focal beams are computed by a minimization scheme, which is discussed in detail in chapter 4.

Appendix C

The Radon transformation

The focal beams are computed in the spatial domain and then a plane wave decomposition of the focal beams by means of a Radon transformation shows the angles from which the target point is illuminated (source beam) or detected (detector beam). In this appendix, we discuss the Radon transformation operator by which a beam in the spatial domain is transformed into the Radon domain. In the spatial domain the focal beams for a target point $(x, y)_j$ at depth level z_m are a function of x, y and ω . In the Radon domain the focal beams can be represented as a function of the lateral ray parameter components p_x, p_y and intercept time τ . The linear Radon transformation of the focal beam, with respect to target point $(x, y)_j$ can be written as follows:

$$\hat{B}_j(\vec{p}, z_m, \tau) = \Delta x \Delta y \sum_{y_n} \sum_{x_n} B_j(\vec{x}_j - \vec{x}_n, z_m, \omega) e^{j\omega[\tau + \vec{p} \cdot (\vec{x}_j - \vec{x}_n)]}, \quad (C.1)$$

where τ is the intercept time, ω is the radial frequency, the vector \vec{x} represents the spatial coordinates (x, y) , and the vector \vec{p} represents the lateral ray parameter components (p_x, p_y) . The hat symbol $\hat{\cdot}$ indicates the Radon domain. Δx and Δy are the discrete sampling intervals of x and y . Equation (C.1) transforms the spatial beam $B_j(\vec{x}_j - \vec{x}_n, z_m, \omega)$ to the Radon-transformed focal beam $\hat{B}_j(\vec{p}, z_m, \tau)$ for lateral location \vec{x}_j , indicated by the subscript j . Note that the Radon transform is shifted such that location \vec{x}_j is the lateral origin of the coordinate system. Since we are only interested in zero intercept time, the Radon transform simplifies to:

$$\hat{B}_j(\vec{p}, z_m, \tau = 0) = \Delta x \Delta y \sum_{y_n} \sum_{x_n} B_j(\vec{x}_j - \vec{x}_n, z_m, \omega) e^{j\omega[\vec{p} \cdot (\vec{x}_j - \vec{x}_n)]}. \quad (C.2)$$

In the matrix operator notation, expression (C.2) can be written as:

$$\hat{B}_j(z_m) = \Gamma \vec{B}_j(z_m, \omega), \quad (C.3)$$

where each element of the Radon transformation operator Γ has the form:

$$\Gamma_{kn} = \Delta x \Delta y e^{j\omega \mathbf{p}_k \cdot (\vec{\mathbf{x}}_j - \vec{\mathbf{x}}_n)}. \quad (C.4)$$

The length of the column vector $\vec{B}_j(z_m, \omega)$ is $N_x N_y$, where N_x is the number of x -samples and N_y is the number of y -samples. The length of the column vector $\hat{B}_j(z_m)$ is $P_x P_y$, where P_x is the number of p_x -samples and P_y is the number of p_y -samples. It means the size of the Radon operator Γ is $P_x P_y$ by $N_x N_y$. Bear in mind that the two lateral coordinates x and y are arranged along one matrix dimension and two ray parameter components p_x and p_y are arranged along the other matrix dimensions as shown in Figure C.1.

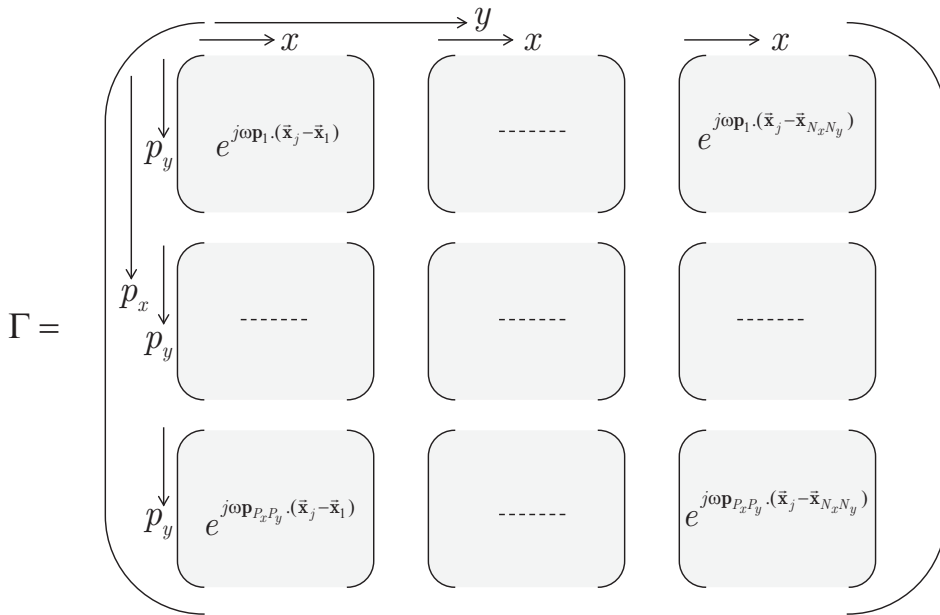


Figure C.1: 2 dimensional Radon operator arranged in matrix form. The size of operator is $P_x P_y$ by $N_x N_y$.

Bibliography

Berkhout, A. J., and Verschuur, D. J., 1994, Multiples technology, Part II: Migration of multiple reflections: 64th Annual International Meeting, Soc. Expl. Geophys., Expanded abstracts, 1497–1500.

Berkhout, A. J., and Verschuur, D. J., 2004, Imaging multiple reflections, the concept: 74th Annual International Meeting, Soc. of Expl. Geophys., Expanded abstracts, 1273–1276.

Berkhout, A. J., and Verschuur, D. J., 2011, Full wavefield migration, utilizing surface and internal multiple scattering: 81st Annual International Meeting, Soc. of Expl. Geophys., Expanded abstracts, 3212–3216.

Berkhout, A. J., and Verschuur, D. J., 2014, Sensitivity of data acquisition in full wavefield migration: 84th Annual International Meeting, Soc. of Expl. Geophys., Expanded abstracts, 3920–3924.

Berkhout, A. J., Ongkiehong, L., Volker, A. W. F., and Blacqui  re, G., 2001, Comprehensive assessment of seismic acquisition geometries by focal beams - Part I: Theoretical considerations: *GEOPHYSICS*, **66**, 911–917.

Berkhout, A. J., Blacqui  re, G., and Verschuur, D. J., 2012a, Multiscattering illumination in blended acquisition: *GEOPHYSICS*, **77**, no. 2, P23–P31.

——— 2012b, Illumination properties and imaging promises of blended, multiple-scattering seismic data: a tutorial: *Geophysical Prospecting*, **60**, 713–732.

Berkhout, A. J., 1982, Seismic migration, imaging of acoustic energy by wave field extrapolation, A. theoretical aspects: Elsevier.

Berkhout, A. J., 1984, Seismic resolution: a quantitative analysis of resolving power of acoustical echo techniques: Geophysical Press, London – Amsterdam.

Berkhout, A. J., 1997a, Pushing the limits of seismic imaging, part I: prestack migration in terms of double dynamic focusing: *GEOPHYSICS*, **62**, no. 3, 937–953.

——— 1997b, Pushing the limits of seismic imaging, part II: integration of prestack migration, velocity estimation and AVO analysis: *GEOPHYSICS*, **62**, no. 3, 954–969.

Berkhout, A. J., 2012, Combining full wavefield migration and full waveform inversion, a glance into the future of seismic imaging: *GEOPHYSICS*, **77**, no. 2, S43–S50.

Berkhout, A. J., 2014a, An outlook on the future of seismic imaging, Part II: Full-wavefield migration: *Geophysical Prospecting*, **62**, 931–949.

——— 2014b, Review paper: An outlook on the future of seismic imaging, Part I: forward and reverse modelling: *Geophysical Prospecting*, **62**, 911–930.

Beylkin, G., 1985, Imaging of discontinuities in the inverse scattering problem by inversion of a causal generalized Radon transform: *J. Math. Phys.*, **26**, no. 1, 99–108.

Blacquière, G., Debeye, H. W. J., Wapenaar, C. P. A., and Berkhout, A. J., 1989, 3-D table-driven migration: *Geophys. Prosp.*, **37**, 925–958.

Bostock, M. G., Rondenay, S., and Shragge, J., 2001, Multiparameter two-dimensional inversion of scattered teleseismic body waves: *Journal of Geophysical Research*, **106**, 30771–30782.

Brink, M., Jones, N., Doherty, J., Vinje, V., and Laurain, R., 2004, Infill decisions based on estimated reflection amplitudes: 74th Ann. Internat. Mtg., Soc. Expl. Geophys., ACQ 2.7.

Brown, M. P., and Guitton, A., 2005, Least-squares joint imaging of multiples and primaries: *GEOPHYSICS*, **70**, no. 5, S79–S89.

Bunting, T., Watterson, P., and Vassallo, M., 2013, Isometrically sampled towed-streamer marine seismic data: 13th International Congress of the Brazilian Geophysical Society and EXPOGEF, Rio de Janeiro, Brazil, SEG, 1177–1180.

Campbell, S., Pramik, W. B., and Cafarelli, B., 2002, Comparative ray-based illumination analysis: 72nd Annual International Meeting, SEG, Expanded Abstracts.

Chang, T., Kue, C., Canales, L., and Shih, C., 2002, Forward modeling attribute analysis for AVO and prestack depth migration: 72nd Annual International Meeting, SEG, Expanded Abstracts.

Cordseen, A., Galbraith, M., and Peirce, J., 2000, Planning land 3-D seismic surveys: Soc. Expl. Geophys.

Corones, J., 1975, Bremmer series that correct parabolic approximations: Journal of mathematical analysis and applications, **50**, 361–372.

Dash, R., Spence, G., Hyndman, R., Grion, S., Wang, Y., and Ronen, S., 2009, Wide-area imaging from obs multiples: GEOPHYSICS, **74**, no. 6, Q41–Q47.

Davydenko, M., and Verschuur, D. J., 2013, Full wavefield migration, using internal multiples for undershooting: 83rd Annual International Meeting, Soc. of Expl. Geophys., Expanded abstracts, 3741–3745.

Davydenko, M., and Verschuur, D. J., 2014, Full wavefield migration in three dimensions: 84th Annual International Meeting, Soc. of Expl. Geophys., Expanded abstracts, 3935–3940.

Davydenko, M., Staal, X., and Verschuur, D. J., 2012, Full wavefield migration in multi-dimensional media, examples: 82nd Annual International Meeting, Soc. of Expl. Geophys., Expanded abstracts, 1–5.

Day, A., and Rekdal, T., 2006, Determining infill specifications based on geophysical criteria: 76th Annual International Meeting, Soc. of Expl. Geophys., Expanded abstracts, 30–35.

De Bruin, C. G. M., Wapenaar, C. P. A., and Berkhout, A. J., 1990, Angle-dependent reflectivity by means of prestack migration: GEOPHYSICS, **55**, no. 09, 1223–1234.

Dragoset, B., Verschuur, E., Moore, I., and Bisley, R., 2010, A perspective on 3d surface-related multiple elimination: GEOPHYSICS, **75**, 75245–75261.

Fleury, C., 2013, Increasing illumination and sensitivity of reverse-time migration with internal multiples: Geophysical Prospecting, **61**, 891–906.

Foster, D., and Mosher, C., 1992, Suppression of multiple reflections using the radon transform: GEOPHYSICS, **57**, 386–395.

Galbraith, M., 2004, A new methodology for 3D survey design: The Leading Edge, **23**, no. 10, 1017–1023.

Gazdag, J., and Sguazzero, P., 1984, Migration of seismic data by phase-shift plus interpolation: *GEOPHYSICS*, **49**, no. 02, 124–131.

Gazdag, J., 1978, Wave equation migration with the phase-shift method: *GEOPHYSICS*, **43**, no. 7, 1342–1351.

Gibson, R. L., and Tzimeas, C., 2002, Quantitative measures of image resolution for seismic survey design: *GEOPHYSICS*, **67**, no. 6, 1844–1852.

Granli, J. R., Arntsen, B., Sollid, A., and Hilde, E., 1999, Imaging through gas-filled sediments using shear-wave data: *GEOPHYSICS*, **64**, no. 3, 668–677.

Gustafsson, M., 2000, The Bremmer series for a multi-dimensional acoustic scattering problem: *J. Phys. A: Math. Gen.*, **33**, 19211932.

Hestenes, M. R., and Stiefel, E., 1952, Methods of conjugate gradient for solving linear systems: *Journal of Research of the National Bureau of Standards*, **49**, 409–436.

Hoffmann, J., Rekdal, T., and Hegna, S., 2002, Improving the data quality in marine streamer seismic by increased crossline sampling: 72nd Annual International Meeting, Soc. of Expl. Geophys., Expanded abstracts, 85–88.

Hoffmann, J., 2001, Illumination, resolution, and image quality of PP- and PS-waves for survey planning: *The Leading Edge*, **20**, no. 9, 1008–1014.

Holberg, O., 1988, Towards optimum one-way wave propagation: *Geophys. Prosp.*, **36**, 99–114.

Jiang, Z., Yu, J., Schuster, G. T., and Hornby, B. E., 2005, Migration of multiples: *The Leading Edge*, **24**, no. 3, 315–318.

Jurick, D., Codd, J., Hoxha, F., Naumenko, J., and Kessler, D., 2003, Gulf of Suez acquisition design using 2D and 3D full wave equation simulation: 73rd Annual International Meeting, Soc. Expl. Geophys., Expanded abstracts, 2136–2139.

Kinneging, N. K., Budejicky, V., Wapenaar, C. P. A., and Berkhout, A. J., 1989, Efficient 2D and 3D shot record redatuming: *Geophys. Prosp.*, **37**, no. 5, 493–530.

Kumar, A., and Blacquière, G., 2013, Including secondary illumination in seismic acquisition design: 83rd Annual International Meeting, Soc. of Expl. Geophys., Expanded abstracts, 181–185.

Kumar, A., Blacquière, G., and Verschuur, D. J., 2014a, 3D acquisition geometry analysis: incorporating information from multiples: 84th Annual International Meeting, Soc. of Expl. Geophys., Expanded abstracts, 30–35.

——— 2014b, Extending illumination using all multiples: Application to seismic acquisition analysis: *Geoph. Prosp.*, Accepted in press.

Kumar, A., Blacquière, G., Pedersen, M. W., and Goertz, A., 2015, Full-wavefield marine survey design using all multiples: *GEOPHYSICS*, in press.

Laurain, R., Gelius, L. J., Vinje, V., and Lecomte, I., 2004, A review of 3D illumination studies: *Journal of Seismic Exploration*, **13**, 17–37.

Liu, Y., Chang, X., Jin, D., He, R., Sun, H., and Zheng, Y., 2011, Reverse time migration of multiples for subsalt imaging: *GEOPHYSICS*, **76**, no. 5, WB209–WB216.

Long, A., 2010, An overview of seismic azimuth for towed streamers: *The Leading Edge*, **29**, no. 5, 512–523.

Lopez, G. A., and Verschuur, D. J., 2013, 3D primary estimation by sparse inversion using the focal domain parameterization: 83rd Annual International Meeting, Soc. of Expl. Geophys., Expanded abstracts, 4172–4177.

Lu, S., Whitmore, N., Valenciano, A., and Chemingui, N., 2011, Imaging of primaries and multiples with 3d seam synthetic: 81st Annual International Meeting, Soc. of Expl. Geophys., Expanded abstracts, 3217–3221.

Lu, S., Whitmore, D., Valenciano, A., and Chemingui, N., 2014, Enhanced subsurface illumination from separated wavefield imaging: *First Break*, **32**, 87–92.

Malcolm, A. E., Ursin, B., and de Hoop, M., 2008, Seismic imaging and illumination with internal multiples: *Geophys. J. Int.*, **176**, no. 3, 847–864.

Mandroux, F., Ong, B., Ting, C.-O., Mothi, S., Huang, T., and Li, Y., 2013, Broadband, long-offset, full-azimuth, staggered marine acquisition in the gulf of mexico: *First Break*, **31**.

Muerdter, D., and Ratcliff, D., 2001, Understanding subsalt illumination through ray-trace modeling, Part 1: Simple 2-D salt models: *The Leading Edge*, **20**, no. 6, 578–595.

Regone, C. J., 2006, A modeling approach to wide-azimuth design for subsalt imaging: *The Leading Edge*, **25**, no. 12, 1467–1475.

Rondenay, S., Bostock, M. G., and Fischer, K., 2005, Multichannel inversion of scattered teleseismic body waves: Practical considerations and applicability: *Geophysical Monograph Series*, **157**.

Ronholt, G., Korsmo, O., Danielsen, B., Brown, S., Brandsberg-Dahl, S., Valenciano, A., Chemingui, N., Whitmore, D., and Lie, J. E., 2014, High fidelity imaging using reflections, refractions and multiples: North sea example, johan sverdrup field: 84th Annual International Meeting, Soc. of Expl. Geophys., Expanded abstracts, 4738–4742.

Sheriff, R. E., 2002, *Encyclopedic dictionary of applied GEOPHYSICS*, fourth edition: Soc. of Expl. Geophys.

Slawson, S. E., Grove, K. D., and Fischer, G. W., 1994, Model-based 3-D seismic acquisition design: 64th Annual International Meeting, Soc. Expl. Geophys., Expanded abstracts, 919–920.

Slob, E., Wapenaar, K., Broggini, F., and Snieder, R., 2014, Seismic reflector imaging using internal multiples with Marchenko-type equation: *GEOPHYSICS*, **79**, no. 2, S63–S76.

Soni, A. K., and Verschuur, D. J., 2014, Full wavefield migration of vertical seismic profiling data: using all multiples to extend the illumination area: *Geophysical Prospecting*, **62**, 740–759.

Soni, A., Staal, X., and Verschuur, D. J., 2012, VSP imaging using all multiples: Full wavefield migration approach: 82nd Annual International Meeting, Soc. of Expl. Geophys., Expanded abstracts, 1–6.

Soni, A., Verschuur, D. J., and Davydenko, M., 2014, Full wavefield migration to image salt-flanks using an unblended and blended VSP data: 84th Annual International Meeting, Soc. of Expl. Geophys., Expanded abstracts, 5085–5091.

Soni, A. K., 2014, Full wavefield migration of vertical seismic profiling data: Ph.D. thesis, Delft University of Technology.

ten Kroode, 2002, Prediction of internal multiples: *WAVE MOTION*, **35**, no. 4, 315–338.

Thorbecke, J., and Wapenaar, K., 2003, Improved extrapolation operator design with the WLSQ method: 73rd Ann. Internat. Mtg., Soc. of Expl. Geophys., 1146–1149.

Thorbecke, J. W., Wapenaar, C. P. A., and Swinnen, G., 2004, Design of one-way wavefield extrapolation operators, using smooth functions in WLSQ optimization: *GEOPHYSICS*, **69**, no. 4, 1037–1045.

Threadgold, I. M., ZembeckEngland, K., Aas, P. G., Fontana, P. M., Hite, D., and Boone, W. E., 2006, Implementing a wide azimuth towed streamer field trial: the what, why and mostly how of wats in Southern Green Canyon: 76th Annual International Meeting, Soc. of Expl. Geophys., Expanded abstracts, 2901–2904.

Toxopeus, G., Petersen, S., and Wapenaar, K., 2003, Improved geologic modeling and interpretation by simulated migrated seismics: 73rd Annual International Meeting, Soc. of Expl. Geophys., Expanded abstracts, 1829–1832.

van der Neut, J., Thorbecke, J., Mehta, K., Slob, E., and Wapenaar, K., 2011, Controlled-source interferometric redatuming by crosscorrelation and multidimensional deconvolution in elastic media: *GEOPHYSICS*, **76**, no. 4, SA63–SA76.

van Groenestijn, G. J. A., and Verschuur, D. J., 2009, Estimating primaries by sparse inversion and application to near-offset data reconstruction: *GEOPHYSICS*, **74**, no. 3, A23–A28.

van Veldhuizen, E. J., Blacquière, G., and Berkhouit, A. J., 2008, Acquisition geometry analysis in complex 3D media: *GEOPHYSICS*, **73**, no. 5, Q43–Q58.

van Veldhuizen, E. J., 2006, Integrated approach to 3-D seismic acquisition geometry analysis: Ph.D. thesis, Delft University of Technology.

Vasconcelos, I., Snieder, R., and Hornby, B., 2008, Imaging internal multiples from subsalt VSP data - examples of target-oriented interferometry: *GEOPHYSICS*, **73**, no. 4, S157S168.

Vermeer, G. J. O., 1999, Factors affecting spatial resolution: *GEOPHYSICS*, **64**, 942–953.

Vermeer, G. J. O., 2012, 3-D seismic survey design, second edition: Society of Exploration Geophysicists.

Verschuur, D. J., and Berkhout, A. J., 2011, Seismic migration of blended shot records with surface-related multiple scattering: *Geophysics*, **76**, no. 01, A7–A13.

Verschuur, D. J., Berkhout, A. J., and Wapenaar, C., 1992, Adaptive surface-related multiple elimination: *Geophysics*, **57**, no. 9, 1166–1177.

Verschuur, D. J., 2006, Seismic multiple removal techniques - past, present and future: EAGE Publications BV.

Vidale, J. E., 1988, Finite-difference calculation of travel times: *Bulletin of the Seismological Society of America*, **78**, no. 78, 2062–2076.

Virieux, J., 1986, *P-SV* wave propagation in heterogeneous media: velocity-stress finite-difference method: *GEOPHYSICS*, **51**, 889–901.

Volker, A. W. F., Blacquière, G., Berkhout, A. J., and Ongkiehong, L., 2001, Comprehensive assessment of seismic acquisition geometries by focal beams - Part II: Practical aspects and examples: *GEOPHYSICS*, **66**, 918–931.

Volker, A. W. F., 2002, Assessment of 3-D seismic acquisition geometries by focal beam analysis: Ph.D. thesis, Delft University of Technology.

von Seggern, D., 1994, Depth imaging resolution of 3-D seismic recording patterns: *GEOPHYSICS*, **59**, 564–576.

Walters, S. L., Miller, R. D., and Raef, A. E., 2006, Repeatability observations from a timelapse seismic survey: 76th Annual International Meeting, SEG, 3185–3189.

Wapenaar, C. P. A., and Berkhout, A. J., 1989, Elastic wave field extrapolation: Redatuming of single- and multi-component seismic data: Elsevier Science Publ. Co., Inc.

Wapenaar, K., van der Neut, J., Ruigrok, E., Draganov, D., J., H., Slob, E., and Snieder, R., 2011, Seismic interferometry by crosscorrelation and by multidimensional deconvolution: A systematic comparison: *Geophysical Journal International*, **185**, no. 3, 1335–1364.

Wapenaar, K., Thorbecke, J., van der Neut, J., Broggini, F., Slob, E., and Snieder, R., 2014a, Marchenko imaging: *GEOPHYSICS*, **79**, no. 3, WA39–WA57.

——— 2014b, On the focusing conditions in time-reversed acoustics, seismic interferometry, and Marchenko imaging: 84th Annual International Meeting, Soc. of Expl. Geophys., Expanded abstracts, 4613–4619.

Wapenaar, C. P. A., 1996, One-way representations of seismic data: *Geoph. J. Int.*, **127**, 178–188.

Wapenaar, C. P. A., 1997, 3-D migration of cross-spread data: Resolution and amplitude aspects: *GEOPHYSICS*, **62**, no. 04, 1220–1225.

Wapenaar, C. P. A., 1998, Short note – Reciprocity properties of one-way propagators: *GEOPHYSICS*, **63**, no. 05, 1795–1798.

Wei, W., Fu, L. Y., and Blacquière, G., 2012, Fast multifrequency focal beam analysis for 3D seismic acquisition geometry: *GEOPHYSICS*, **77**, P11–P21.

Whitmore, N., Valenciano, A., and Sollner, W., 2010, Imaging of primaries and multiples using a dualsensor towed streamer: 80th Annual International Meeting, Soc. of Expl. Geophys., Expanded abstracts, 3187–3192.

Xie, X., Jin, S., and Wu, R., 2006, Wave-equation-based seismic illumination analysis: *GEOPHYSICS*, **71**, no. 5, S169–S177.

Youn, O. K., and Zhou, H. W., 2001, Depth imaging with multiples: *GEOPHYSICS*, **66**, no. 1, 246–255.

Zheng, D., and Schuster, G. T., 2014, Least-squares reverse time migration of multiples: *GEOPHYSICS*, **79**, no. 1, S11–S21.

Acknowledgments

Reaching a milestone is remarkable; but the journey to the milestone is always memorable and a treasure for life. Throughout this journey of mine at innumerable instances I had to hunt for new direction and that is where, all the below named persons have contributed immensely and played a pivotal role. Contribution from all of them has helped me synthesize ideas, works and my efforts in to this thesis.

Dr. Gerrit Blacquiere, my mentor for this research work; has been instrumental for my learning in Geophysics and has always been a source of inspiration and encouragement. His continued guidance and support helped me figure out what exactly I wanted to do. I express my deep gratitude to you Gerrit for the support you have extended to me during my research. I would also like to thank you for critically reviewing my conference abstracts, journal papers, and my thesis. Dr. Eric Verschuur, the person with spool of ideas; taught me that problems in research do provide a window to its own solution and has always been accessible whenever I needed a breakthrough. Professor Guus Berkhout, the leader of the DELPHI group, an encyclopaedia in himself, always taught me that presentation of ideas and results matters the most (whatever you have done, you should be able to communicate it properly). My completion of this work could not have been accomplished without the support of my promotor Professor Kees Wapenaar. He ensured right momentum and support for this work. I would like to thank him for the inspiring courses and for his remarks on this thesis to improve the contents.

Sponsoring for any project is like blood in our body and this is where DELPHI consortium sponsors have always been phenomenal in providing impetus for growth to innumerable researchers like me. I offer my sincere appreciation for the learning opportunities, international exposure (during each Delphi sponsor meeting) and required financial support provided by DELPHI consortium sponsors.

I would like to thank Roald van Borselen to invite me at the Leiden office of PGS to present my research work, which results in getting an opportunity to work as an intern at the PGS office in Oslo, Norway. I would like to acknowledge PGS Oslo for giving me the opportunity to carry out part of my PhD work during my internship in Oslo, Norway. I would like to thank team leader Alexander Goertz, and my mentors Morten Pedersen and Stefen Jetschny. Additional thanks to Morten for day to day scientific discussion on the project work during my internship and meticulously reading and reviewing my journal papers.

For proper nourishment of a baby, its important to have a lively environment having the righteous combination of factors for growth and TU Delft is an ideal and phenomenal place for research not only because of the facilities, but mainly because of the people. For this reason, I would like to express my thanks to all PhD students with whom I had many learning and fun moments. I would like to mention most of the names here. Thanks Alok, Araz and Panos for helping me in my early days of my PhD to get started with Delphi notations; thanks Tomo for day to day discussion from the beginning to the end of our PhD research life; thanks Pawan for many fruitful discussions, ideas and sharing fun moments during conferences; thanks Mikhail for helping me to understand full wavefield modelling scheme; thanks Iris for translating my PhD summary in Dutch; thanks Joost, Siddharth, Niels, Matteo, Sixue, Boris, Carlos and Gabriel for all the pleasant outings during conferences and for great dining I shared with you all. Many thanks are also due to current and past members of our research group: Alex, Xander Staal, Juerg, Elmer, Alimzhan, Bouchaib, Jan-Willem, Runhai, Asiya, Abdulrahman, Hussain, Hannes, Yimin, Rik, Andreas, Jan, Ranjani, Shogo, Yohei, Apostolos, Max, Peter, Ralf. Thank you all. Please forgive me if I unintentionally miss someone's name.

The move to the Netherlands for pursuing my PhD would have never been much fun without my friends. Now, I would like to thank some of my close friends living in Delft. Thanks Sana for being my first wonderful Pakistani friend and never let me miss India in terms of food. Philippe, Kishor, Mohit, Ankit, Shirish, Ajay, Gargi, Sampi, Naresh: Thank you all for all the fun times and get-togethers.

Finally, to my caring, loving, and supportive Parents: my deepest gratitude. Your encouragement when the times got rough are much appreciated and duly noted. The countless times, I severed; your love and blessing engulfed and shielded me from all problems in life. My brother, Sumiran: you have

been my greatest source of strength. I love you with all my heart. My sister, sister-in-law and brother-in-law, Sonam, Dharini and Rakesh: Thank you for being always available whenever I needed someone in tough times. I owe everything to you.

Oh, GOD! I would never have been what I am today without your blessings and enlightenment. Please accept my heartfelt gratitude for bestowing me with enough wisdom and strength to complete this research work.

New Beginnings create new endings. With blessings, love and support of all of you, I look forward to new adventures in my life. Wish me Luck!

My heartfelt thanks to all.

Delft, August 2015

Amarjeet

Curriculum Vitae

Personal information

Name Amarjeet Kumar
Nationality Indian
Date of birth 22nd November, 1987
Place of birth Bairababad, Bihar, India

Education and work

Since August 2015	Researcher, Delphi Consortium, Delft University of Technology, The Netherlands
2011–2015	PhD in Applied Geophysics, Delft University of Technology, the Netherlands
2014 (August–October)	Research intern, Petroleum Geo-Services., Oslo, Norway
2006–2011	5 year Integrated Master course, Exploration Geophysics Indian Institute of Technology, Kharagpur, India
2009 (May–July)	Summer intern, Australian National University, Canberra, Australia

Journal papers

- **Kumar, A.**, G. Blacquiere and D.J. Verschuur, 2015, Extending illumination using all multiples: application to 3D acquisition geometry analysis, *Geophysical prospecting*.
<http://dx.doi.org/10.1111/1365-2478.12326>.
- **Kumar, A.**, G. Blacquiere, M. W. Pedersen and A. Goertz, 2015, Full-wavefield marine survey design using all multiples, Accepted by *Geophysics* (In press).
- Tkalcic, H., N. Rawlinson, P. Arroucau, **A.Kumar** and B.L.N. Kennett, Multi-Step modeling of receiver-based seismic and ambient noise data from WOMBAT array: Crustal structure beneath southeast Australia, *Geophys. J. Int.*, 189, 1681-1700, 2012.

Conference abstracts

- **Kumar, A.** and G. Blacquiere, Full wavefield acquisition analysis: the benefits of using multiples, *SEG Technical Program Expanded Abstracts 2015*: 260-265.
- **Kumar, A.**, G. Blacquiere., M. W. Pedersen and A. Goertz, Marine survey design and analysis using all multiples: *77th EAGE Conference and Exhibition 2015*, DOI: 10.3997/2214-4609.201412596.
- **Kumar, A.**, G. Blacquiere and D.J. Verschuur, 3-D acquisition geometry analysis: incorporating information from all multiples: *SEG Technical Program Expanded Abstracts 2014*: 30-35.
- **Kumar, A.**, G. Blacquiere and D.J. Verschuur, Optimizing illumination using multiples: application to seismic acquisition analysis: *76th EAGE Conference and Exhibition 2014*, DOI: 10.3997/2214-4609.20141465.
- **Kumar, A.**, and G. Blacquiere, Including secondary illumination in seismic acquisition design: *SEG Technical Program Expanded Abstracts 2013*: 181-185.
- **Kumar, A.**, and G. Blacquiere, Taking advantage of surface-related multiples in seismic acquisition design: *75th EAGE Conference and Exhibition incorporating SPE EUROPEC 2013*, DOI: 10.3997/2214-4609.20130739.

- **Kumar, A.**, H. Tkalcic, P. Arroucau, N. Rawlinson, M. Sambridge and B. L. Kennett, Constraints on Southeast Australian Lithosphere From Multi- Step Modeling of Teleseismic and Noise Data Recorded by the SEAL3, Experiment: Eos Trans. AGU, 90(52), Fall Meet. Suppl., Abstract S13B-1755.

Delphi Chapters

- **Kumar, A.**, Blacquiere, G, Pedersen, M.W and Goertz, A. (2015). Chapter 5: Marine survey design and analysis using all multiples, Delphi: The A&P Project (2015) (From Seismic Measurements to Rock and Pore Parameters, XIX) (pp. 53-73).
- **Kumar, A.**, Blacquiere, G and Verschuur, D.J (2015). Chapter 4: Extending illumination using multiples: Application to Seismic Acquisition Design, Delphi: The A&P Project (2015) (From Seismic Measurements to Rock and Pore Parameters, XIX) (pp. 23-48).
- **Kumar, A.**, Blacquiere, G and Verschuur, D.J (2014). Chapter 6: Optimizing illumination using multiples, Delphi: The A&P Project (2014) (From Seismic Measurements to Rock and Pore Parameters, XVI) (pp. 28-50).
- **Kumar, A.** and Blacquiere, G (2013). Chapter 6: Taking advantage of multiples in acquisition design, Delphi: The A&P Project (2013) (From Seismic Measurements to Rock and Pore Parameters, XVII) (pp. 105-121).
- **Kumar, A.** and Blacquiere, G (2012). Chapter 8: Acquisition design for fluid front monitoring: the Schoonebeek field, Delphi: The A&P Project (2012) (From Seismic Measurements to Rock and Pore Parameters, XVI) (pp. 131-147).